2009

Tertiary Creep Damage Modeling Of A Transversely Isotropic Ni-based Superalloy

Calvin Stewart
University of Central Florida

TERTIARY CREEP DAMAGE MODELING OF A TRANSVERSELY ISOTROPIC NI-BASED SUPERALLOY

by

CALVIN M STEWART
B.S. University of Central Florida, 2008

A thesis submitted in partial fulfillment of the requirements
for the degree of Master of Science
in the Department of Mechanical, Materials and Aerospace Engineering
in the College of Engineering and Computer Science
at the University of Central Florida
Orlando, Florida

Fall Term
2009

ABSTRACT

Anisotropic tertiary creep damage formulations have become an increasingly important prediction technique for high temperature components due to drives in the gas turbine industry for increased combustion chamber exit pressures, temperature, and the use of anisotropic materials such as metal matrix composites and directionally-solidified (DS) Ni-base superalloys. Typically, isotropic creep damage formulations are implemented for simple cases involving a uniaxial state of stress; however, these formulations can be further developed for multiaxial states of stress where materials are found to exhibit induced anisotropy. In addition, anisotropic materials necessitate a fully-developed creep strain tensor. This thesis describes the development of a new anisotropic tertiary creep damage formulation implemented in a general-purpose finite element analysis (FEA) software. Creep deformation and rupture tests are conducted on L, T, and 45°-oriented specimen of subject alloy DS GTD-111. Using the Kachanov-Rabotnov isotropic creep damage formulation and the optimization software uSHARP, the damage constants associated with the creep tests are determined. The damage constants, secondary creep, and derived Hill Constants are applied directly into the improved formulation. Comparison between the isotropic and improved anisotropic creep damage formulations demonstrates modeling accuracy. An examination of the off-axis creep strain terms using the improved formulation is conducted. Integration of the isotropic creep damage formulation provides time to failure predictions which are compared with rupture tests. Integration of the improved anisotropic creep damage produces time to failure predictions at intermediate orientations and any state of stress. A parametric study examining various states of stress, and materials

orientations is performed to verify the flexibility of the improved formulation. A parametric exercise of the time to failure predictions for various levels of uniaxial stress is conducted.

Dedicated to the Stewart family.

“God keep us strong”

ACKNOWLEDGMENT

I would like to thank my advisor and thesis committee chairman Dr. Ali P. Gordon for his guidance, thoughtful suggestions, and support throughout this thesis process. I'm continually learning from him the importance of striving for excellence in everything you do. My thanks go to the member of my thesis committee, who are: Dr. David W. Nicholson, and Dr. Faissal A. Moslehy.

I am indebted to Erik A. Hogan for developing and providing substantial technical support for the uSHARP optimization program. Without that software, this thesis would not have been possible. I would like to thank Dr. Rick Neu and Dr. Ashok Saxena for provided the material properties and creep deformation and rupture experiments for the thesis.

I would like to thank all the people who have provided technical, emotional, or spiritual support during my thesis including: my fellow graduate students, the members of Knights of Mcknight, my family, and God.

Most importantly, I would like to thank the Mcknight Doctoral Fellowship for provide financial support through the Florida Education Fund.

TABLE OF CONTENTS

LIST OF FIGURES

LIST OF TABLES

CHAPTER ONE: INTRODUCTION

1.1 Motivation

As global power demands increase and the issue of meeting peak power requirements skyrockets, there is considerable interest in improving the efficiency of Industrial Gas Turbines (IGT). Industrial Gas Turbines produce power via high temperature and highly pressurized combustion gases that are driven through a series of turbine blades stages causing rotor rotation, spinning electric generators. Increasing firing temperature by 55°C has been shown to increase power generation by 10-13% and overall cycle efficiency by 4% [1]. Compressor pressure ratios greater than 23 coupled with combustion chamber exit temperatures of above 1425°C create a situation where material design and selection play a major role in the long term reliability of gas turbine components [2].

Nickel-base superalloys are excellent candidate materials for turbine blades, transition pieces, vanes, turbine discs, combustors, and boilers due to high temperature strength, corrosion resistance, and oxidation resistance. Historically, the firing temperature of turbine blade materials has increased on average 6°C per year due to improved metallurgical design, the introduction of advanced air cooling methods, and the evolution of thermal barrier coatings (TBC) [2].

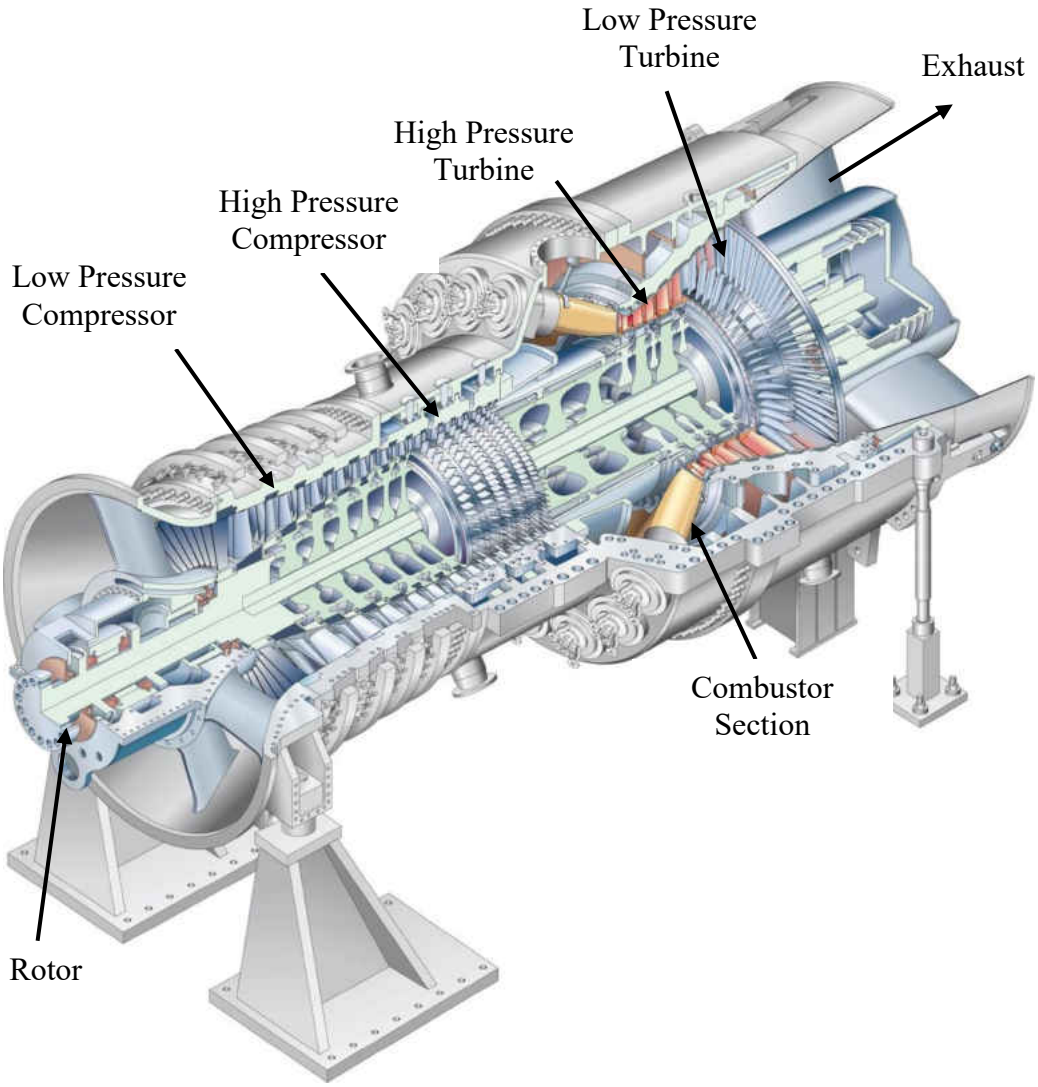

Figure 1.1 – Computer Aided Drawing (CAD) of the 340+ MW Siemens SGT5-8000H gas turbine. Developed using advanced materials and cooling methods, this turbine when used in a SCC5-8000H combined cycle power plant produces efficiency exceeding 60%. [3]

Creep is the inelastic deformation of a material at high temperature. Typically, this form of strain of Ni-base superalloys is predicted via either steady state (e.g. secondary) creep deformation modeling with or without consideration of the tertiary creep regime. As temperature increases, the creep strain rate increases accordingly. Further development, geared towards including the non-linear strain experienced in the tertiary creep regime, leads to the inclusion of

the concept of damage. It resulted in creep damage models where a damage evolution equation is coupled with the creep strain rate equation.

Figure 1.2 – Out of service Siemens transition piece (a) inlet connection (b) external shot of the transition path leading to outlet

Gas turbine transition pieces are components which conduct hot combustion gases into the first ring of stationary blades. They are design to deliver a uniformly distributed mass flow maintaining efficiency. Industry standard materials for this component include, Hastelloy X, Nimonic 263, HS-188, GTD-222, Haynes 230, and IN617 [2]. At the inlet, the connection is a donut section as seen in Figure 1.2a. Along the geometry a smooth transition occurs transforming the cross section to a circular hole at the outlet connection as shown in Figure 1.2b. There is a significant temperature gradient about the inlet connection but beyond it the temperature found along the body and at the outlet is mostly constant. Transition pieces commonly experience temperatures between 40% to 60% of material melting temperature, T_m, and top panel stress at most 20% of the yield strength, σ_y. As such, this thermal activity accelerates the rate at which secondary and tertiary creep deformation modes become dominant. Although previous studies

suggest that for stress level between 20% to 40% of yield strength, σ_y, accurate prediction of the creep rupture life up to 10^6 hours is of importance, when considering that transition pieces undergo not only creep but high cyclic fatigue, accurately modeling the creep rupture life at lower stress levels is critical [4-6].

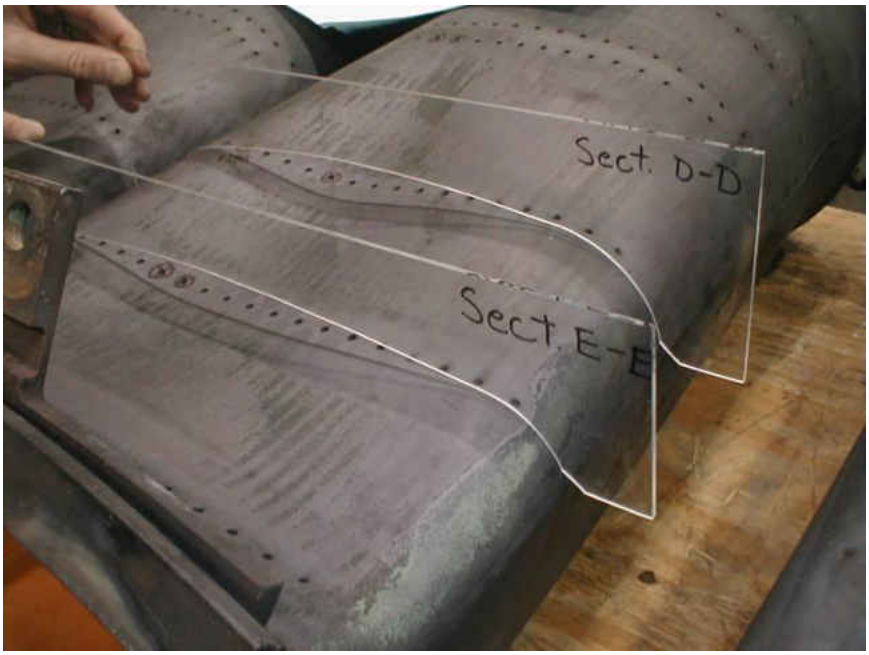

Figure 1.3. - Creep deformation of a IN617 transition piece.

Transition pieces pulled from operation show a fatigue and creep induced buckling of the upper panel near the inlet including a deformation of the transition piece cross-section at the inlet as shown in Figure 1.3. It has been found that the principle causes of gas turbine transition piece failure are creep, high cycle fatigue, and environmental effects [7]. Thermal expansion of the transition piece leads to a loss of clearance between seals at the inlet producing mechanical stress on the top panel. Asymmetric thermal loading coupled with mechanical constraint on the top panel leads to a multiaxial state of stress.

Isotropic creep damage models work best when the mechanical load experienced by a component is similar to what is applied during uniaxial creep tests. Such models are inappropriate for modeling components which undergo complex states of stress. In most cases, the off-axis components of a stress tensor in the vicinity of stress raisers, cracks, and notches have non-zero values and the stress state is more complex than that which can be achieved in conventional creep testing. Moreover, the dependence of creep rate is strongly non-linear with stress; therefore, creep damage may also depend on the 'direction' of the stress vector as well as on the absolute value of its components. Thus in the case of damage, complex states of stress induce an anisotropic material behavior.

Isotropic constitutive modeling efforts for multiaxial/complex states of stress have focused on replacement of von Mises (equivalent tensile) effective with triaxial stress that relates, the first principal, hydrostatic, and von Mises stresses. However, these formulations do not account for induced anisotropic damage.

Drives by the aerospace and power generation industries to increase turbine efficiency have produced a massive influx in the development of anisotropic alloys since the 1980's [8]. Through the process of directional solidification (DS), material manufacturers can directly control the alignment of grain boundaries. The established manufacturing process is the Bridgeman vacuum casting process, where a directional heat flow is generated via remove of the shell mould from a hot zone to a cooling zone at some prescribed rate. In the power generation industry alternative methods such as the liquid metal cooling (LMC) casting process are used due to casting issues inherit to larger components [9,11].

Figure 1.4 - Turbine layers one to three of a 292+ MW Siemens SGT5-4000F Gas turbine. Thermal barrier coatings (TBC) and careful material design and selection allows operation at combustion exit temperatures of 1400°C for this turbine. [10]

The result of directional solidification (DS) is a component which exhibits enhanced strength, stiffness, and/or creep resistance in a set orientation. Typically DS gas turbine blade materials are transversely-isotropic, where there is a plane of "transverse grain (T)" isotropy and an enhanced "long grain (L)" orientation.

Turbine blades experience high temperatures, fuel and air contamination (in marine turbine chlorine due to salt water), and foreign object damage (FOD) an environment very

conducive to corrosion and oxidation. High stress due to centrifugal forces near the speed of sound, dynamic flutter and vibrations, flexural stresses due to combustion gases interfacing with blade surface area, and thermal gradient induced thermal stresses impart a complex state of stress on gas turbine blades [12]. Stress concentrations near the blade root are the frequent location of crack initiation. Fatigue, creep damage and the interactions of both are the principle cause of microstructural damage leading to eventual failure [13]. In the case of IGT turbine blades where the cycle duration and maintenance intervals can in the thousands of hours, DS materials have been implemented to minimize intergranular (brittle) creep cracking by alignment of long grains (L) with the first principal stress direction [14]. However, the regulation of thrust to produce lower or higher power output and the regular fluctuations in combustion exit exhaust velocity coupled with the existence of inherit vibration issues can result in a first principal stress direction not aligned with the enhanced (L) material orientation.

Isotropic creep models are unable to model the orientation-dependence of anisotropic materials. An isotropic-scalar compliance term cannot replicate an anisotropic compliance tensor in symmetry classes such as triclinic, orthotropic, transversely-isotropic materials, and so on.

Constitutive modeling efforts for creep deformation of anisotropic materials have been limited. Few models have been developed, optimized, and actually compared with creep test data. In the case of transversely-isotropic turbine blade materials with induced anisotropic damage, no models currently exist.

A number of creep rupture prediction models are implemented in industry; however, no models have been developed that are capable of predicting the creep rupture time under complex states of stress on a transversely-isotropic material.

1.2 Approach

In approaching this problem, a number of steps are taken. First, the commonly implemented Kachanov-Rabotnov isotropic tertiary creep damage model is written in FORTRAN and implemented in the finite element analysis (FEA) software, ANSYS as a user-programmable feature (UPF). Second, taking available creep test data in longitudinal and transverse orientations of subject material DS GTD-111, the automated optimization software, uSHARP, is used to determine the necessary damage constants at various states of uniaxial stress and temperature. Next, a novel anisotropic tertiary creep damage model using a unique second-order symmetric damage evolution tensor and a creep strain rate tensor with the Hill compliance tensor is developed and implemented in ANSYS. Comparison of the isotropic and novel anisotropic model to uniaxial creep test data shows the novel anisotropic model performs well in L and T orientation but not at intermediate rotations. An improved anisotropic creep damage formulation is produced based principally on application of the multiple hill compliance tensors in the damage evolution equation. The improved formulation is shown to outperform the novel anisotropic in modeling both damage evolution and creep deformation. Integration provides rupture time prediction equation for all three formulations. The isotropic model is found to

predict rupture time well for uniaxial specimen. The novel anisotropic formulation is found to produce good predictions at L and T orientation but not at intermediate material orientations. The improved anisotropic model succeeds in modeling any material orientation. Parametric creep deformation and damage evolution exercise of the improved anisotropic formulation shows it can account for any states of stress and/or material orientations.

1.3 Organization

This work is organized similar to the aforementioned approach. Chapter 2 introduces the fundamentals of creep deformation and reviews the existing isotropic and anisotropic creep deformation and rupture prediction models. Chapter 3 reviews directionally solidified Ni-base superalloys and goes into detail on the subject material, DS GTD-111. Chapter 4 describes the Kachanov-Rabotnov isotropic tertiary creep damage model, the derived rupture time prediction model, and the implementation of the model in FEA. Chapter 5 describes the novel anisotropic tertiary creep damage model, the derived rupture time prediction model, and the implementation of the model in FEA. Chapter 6 describes the improved anisotropic tertiary creep damage model, the derived rupture time prediction model, and the implementation of the model in FEA. Afterwards, in Chapter 7, the results of optimization and a comparison of the creep deformation and rupture prediction models to creep tests data is presented. In Chapter 8, a parametric exercise of the improved anisotropic model under various states of stress and material orientation is presented. Chapter 9 contains concluding remarks and recommendations for future work.

Appendix A contains screenshots of the optimization routine uSHARP. Appendix B covers the derivations necessary to determine Hill's constants. Appendix C contains an analytic stress and material orientation study of the novel anisotropic damage evolution tensor found in the novel anisotropic tertiary creep damage model.

CHAPTER TWO: BACKGROUND

2.1 Fundamentals of Creep Deformation

Creep is defined as time-dependent deformation that occurs below the yield strength of a material. The rate of creep deformation is dependent on material behavior (i.e., creep constants), temperature, time, and stress. Typically creep is discussed in terms of materials under high temperature as the creep rate increases sustainably as temperature increases.

Classically, creep deformation is separated into three distinct stages, primary, secondary, and tertiary creep as depicted in Figure 2.1. Descriptively, this stages are associated with transient, steady-state, and accelerating creep, respectively [15].

In the case of Ni-based superalloys, primary creep, is due to strain-hardening where pre-existing dislocations encounter obstacles (solid solution atoms, dispersoids, precipitates, grain boundaries, etc.) and becoming immobilized [16,17]. It initially occurs at a high rate, but the eventual saturation of dislocation density inhibits further primary creep deformation. For Ni-base superalloys, primary creep is typically small when compared to the rupture strain (about 0.3%). After this stage, secondary creep is observed and is characterized by an almost constant strain rate (typically called the minimal strain rate) due to a balance between strain-hardening and recovery mechanics. Increased mobility enhanced by thermal activity (temperature induced diffusion) can cause cross slip where dislocations can diffuse away from obstacles [18]. In this region, the nucleation of grain boundaries and grain boundary sliding occur. Finally, tertiary

creep becomes dominant and is characterized by a rapid non-linear increase of strain rate until creep rupture. This stage is driven by the net area reduction due to elongation (substantial in ductile material) and the evolution of the phenomena called “damage” which has the effect of reducing material creep strength.

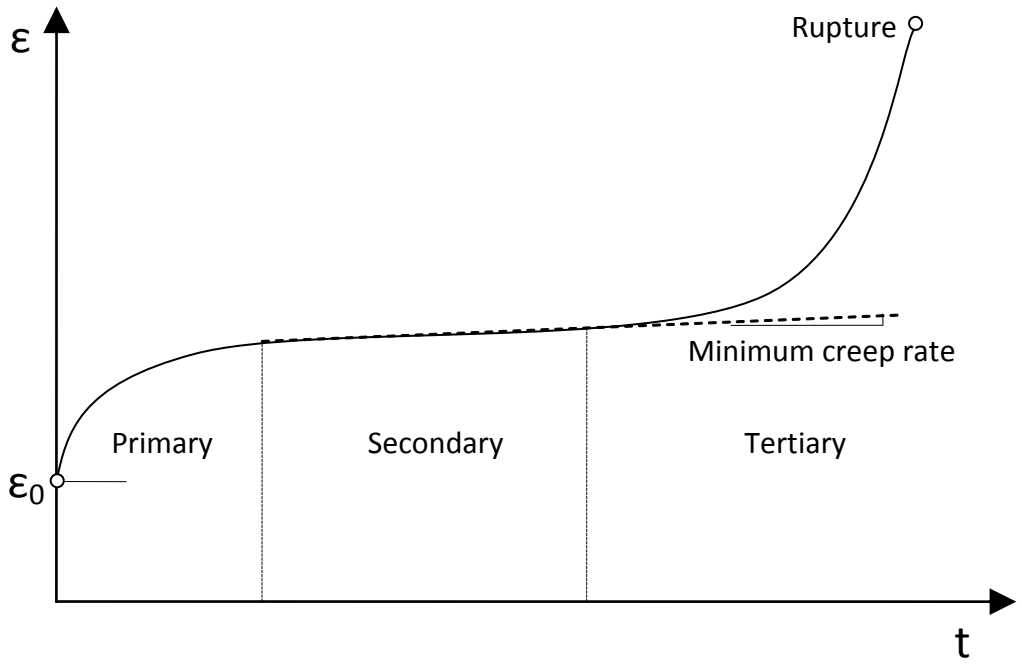

Figure 2.1 - Depiction of creep deformation stages

Creep deformation is accounted for in total strain as a decoupled plastic strain term. Unloading at a suitable rate will result in purely elastic behavior. Total strain takes the following form

$$\varepsilon = \varepsilon_e + \varepsilon_p \tag{2.1}$$

where ε_e is the elastic strain and ε_p is the plastic strain. Typically instantaneous plastic strain and anelastic strain (due to delayed elasticity during unloading) are neglected.

2.2 Primary Creep Modeling

Traditionally, the transient creep observed in the primary creep stage is accounted for using Andrade's law for primary creep of the form.

$$\varepsilon_{cr} = \varepsilon_0 + At^{1/q} \tag{2.2}$$

where ε_0 is instantaneous creep, A ($t^{-1/q}$) is a coefficient, and q is a unitless exponent. The constant q has been experimentally observed to be 3 for most materials [19,20]. A number of authors have attempted to disprove the uniformity of this constant with limited success [21]. A more advantageous formulation for primary creep is based around a power law of the simple form

$$\varepsilon_{cr} = A\sigma^n t^m \tag{2.3}$$

where $\sigma\,(MPa)$ is the applied load and A ($MPa^{-n}hr^{-m}$), n, and m are temperature-dependent primary creep constants [22]. When stress is assumed to be constant, a primary creep time-hardening strain rate equation can be developed of the form

$$\dot{\varepsilon}_{cr} = \frac{d\varepsilon_{cr}}{dt} = Am\sigma^{n}t^{m-1} \tag{2.4}$$

where the units of A change to $MPa^{-n}hr^{-(m-1)}$. This relation is for uniaxial loading. To account for multiaxial states of stress a tensorial formulation is desired [23].

In the case of Ni-based alloys, the primary creep stage is short compared to rupture strain. A study was performed on the creep deformation in the polycrystalline wrought Ni-base alloy IN617 [24]. The melting temperature of IN617 is approximately 1300°C. At environmental temperatures below $0.4T_m$, where T_m is the melting temperature, in most metals creep is largely a slip process observed as primary creep altered by thermal activity. As environmental temperatures reaches between $0.4T_m$ to $0.5T_m$, cross slip and recovery mechanism are arises leading to a reduction in strain hardening. For IN617 at the temperature 649°C (approximately $0.5T_m$) primary creep is observable as strain hardening before the onset secondary creep. It is equivalent to about 25-30% of the rupture strain. At higher temperatures of $0.6T_m$, cross slip and recovery become balanced leading to secondary and tertiary creep behavior [18]. For IN617, as temperature increases, the contribution of primary creep to the final rupture strain becomes negligible. This same behavior is observed in most Ni-based alloys.

2.3 Secondary Creep Modeling

The classical approach to modeling the secondary creep behavior for materials is the Norton power law for secondary creep [25]

$$\dot{\varepsilon}_{cr} = \frac{d\varepsilon_{cr}}{dt} = A\bar{\sigma}^n \tag{2.5}$$

where A and n are the secondary creep constants, and $\bar{\sigma}$ is an equivalent stress. Typical the von Mises equivalent stress which is both isotropic and pressure insensitive is used of the form

$$\begin{aligned} \sigma_H &= \sigma_{kk}/3 \\ \mathbf{S}_{ij} &= \boldsymbol{\sigma}_{ij} - \sigma_H \\ \sigma_{vm} &= \sqrt{\frac{3}{2}\mathbf{S}_{ij}\mathbf{S}_{ij}} \end{aligned} \tag{2.6}$$

where σ_H is the hydrostatic (mean) stress and $\mathbf{S}$ is the deviatoric stress tensor. For anisotropic materials, the well known Hill's anisotropic equivalent stress is implemented of the form

$$\begin{aligned} \sigma_{Hill} &= \sqrt{\mathbf{s}^T\mathbf{M}\mathbf{s}} \\ \mathbf{s} &= VEC(\boldsymbol{\sigma}) \end{aligned} \tag{2.7}$$

$$\mathbf{M} = \begin{bmatrix} G+H & -H & -G & 0 & 0 & 0 \\ -H & F+H & -F & 0 & 0 & 0 \\ -G & -F & F+G & 0 & 0 & 0 \\ 0 & 0 & 0 & 2N & 0 & 0 \\ 0 & 0 & 0 & 0 & 2L & 0 \\ 0 & 0 & 0 & 0 & 0 & 2M \end{bmatrix}$$

where **s** is the vector form of the Cauchy stress tensor, $\boldsymbol{\sigma}$, and **M** is the Hill compliance tensor [26] consisting of the *F*, *G*, *H*, *L*, *M*, and *N* unitless material constants that can be obtained from creep tests [27]. Hill's equivalent stress reverts to von Mises when

$$F = G = H = \frac{1}{2}$$
$$L = M = N = \frac{3}{2} \tag{2.8}$$

The Norton power law is sometimes referred to as the Norton-Bailey law. The secondary creep constants *A* and *n* exhibit temperature-dependence. Stress provides a substantial contribution to the creep strain rate as the *n* secondary creep constant is an exponent of stress. The deformation mechanism map for Pure Ni is provided in Figure 2.2. It demonstrates the influence that stress and temperature have on the onset of various deformation mechanisms and the rates at which deformation will occur.

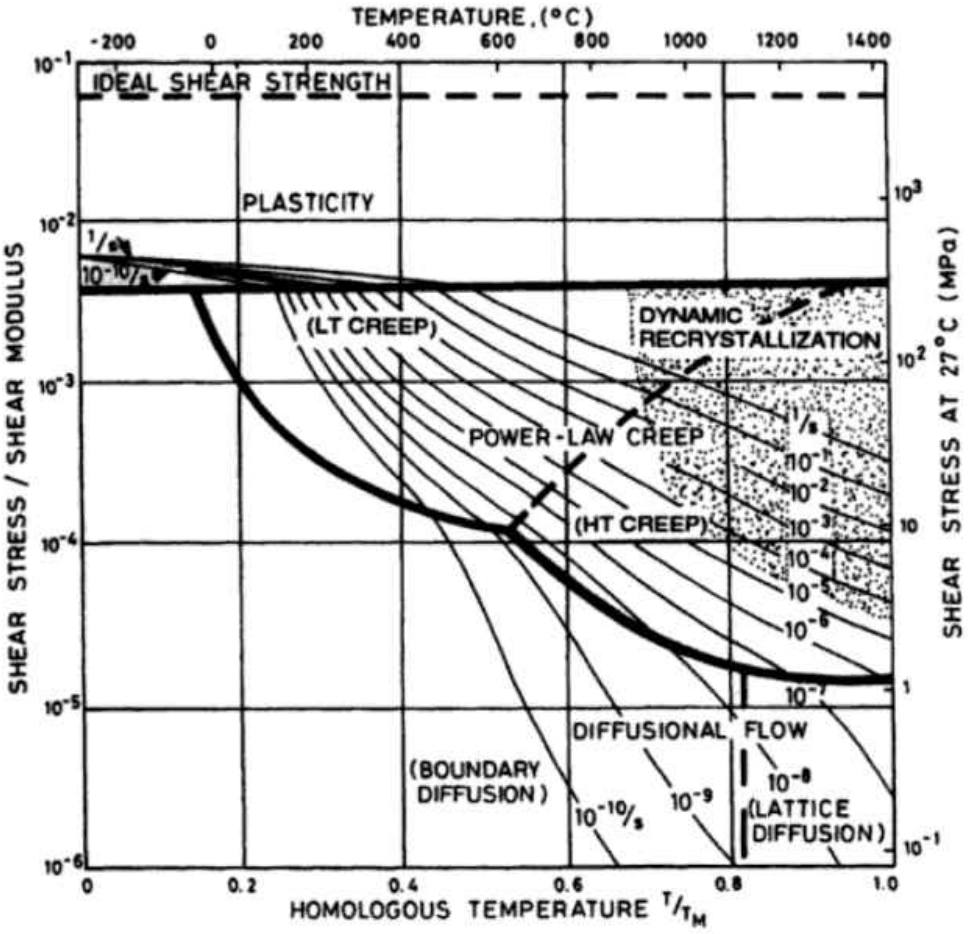

Figure 2.2 - Deformation mechanism map for pure nickel with a grain size of 0.1mm [28]

Dorn [32] suggested that temperature contributions can be accounted for by replacing the *A* constant with an Arrhenius equation

$$A(T) = B\,exp\left(\frac{-Q_{cr}}{RT}\right) \tag{2.9}$$

where B is the pre-exponential factor in units $MPa^{-1}\ hr^{-1}$, Q_{cr} is the apparent activation energy for creep deformation in units $J\ mol^{-1}$, R is the universal gas constant 8.314 $J\ mol^{-1}\ K$, and T is temperature in units Kelvin. Introducing Eq. (2.5) into Eq. (2.9) leads to

$$\dot{\varepsilon}_{cr} = \frac{d\varepsilon_{cr}}{dt} = B\bar{\sigma}^{n}\, exp\left(\frac{-Q_{cr}}{RT}\right) \tag{2.10}$$

Using this equation, stress and temperature contributions to the strain rate are obtained. The secondary creep constants can be determined from uniaxial creep tests by rearranged Eq. (2.10) into the following form

$$ln\,\dot{\varepsilon}_{min} = ln\,B + n\,ln\,\bar{\sigma} - \frac{-Q_{cr}}{RT} \tag{2.11}$$

where the creep strain rate $\dot{\varepsilon}_{cr}$ is replaced with the minimum creep strain rate $\dot{\varepsilon}_{min}$. Plotting the log of the minimum creep strain versus $1/T$, the apparent activation energy of creep, Q_{cr}, can be determined as the slope. Plotting the log of the minimum creep strain versus von Mises equivalent stress, the secondary creep constant, n, can be determined as the slope. This method is graphically represented in Figure 2.3.

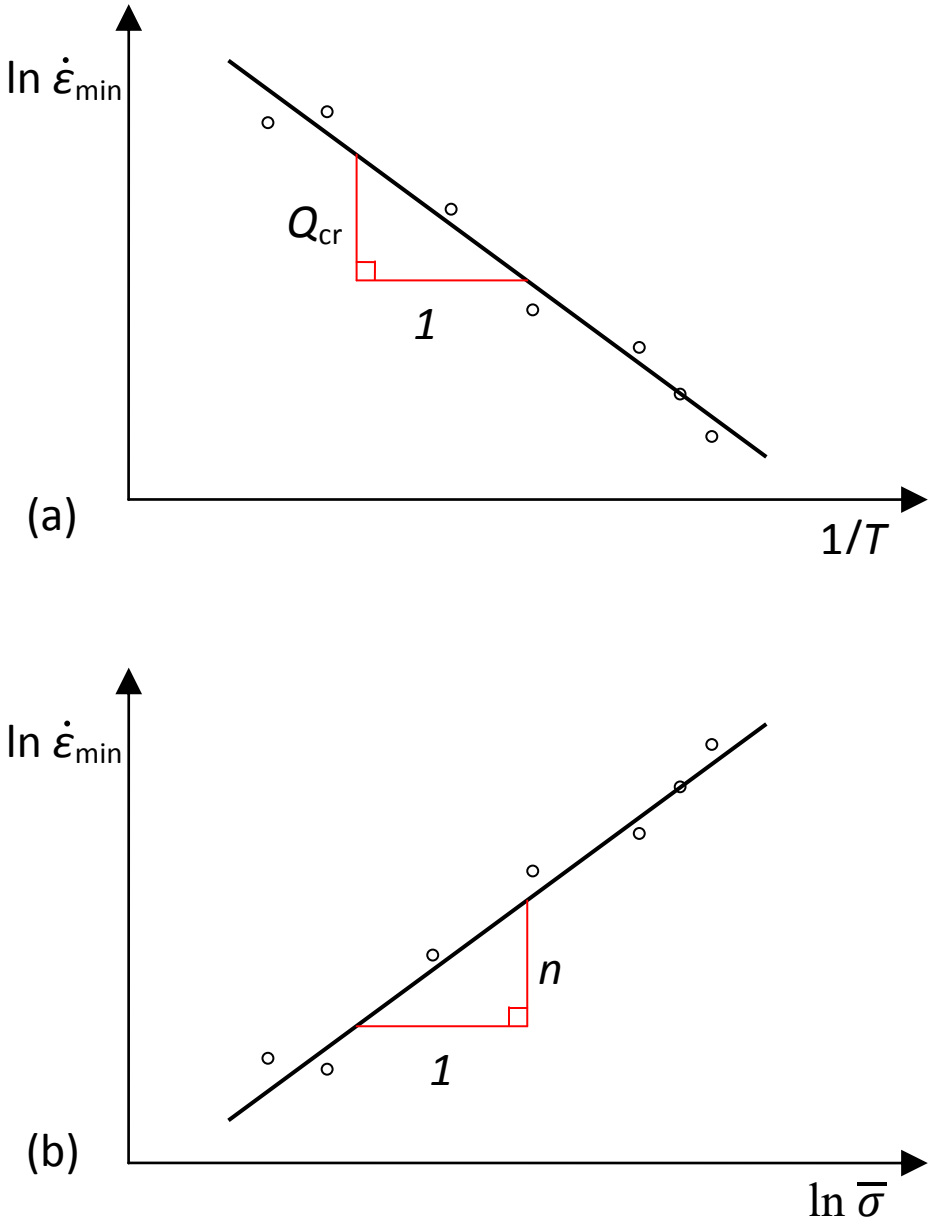

Figure 2.3 - Example of analytical method to determine (a) Q_{cr} and (b) n secondary creep constants from experimental creep tests

Historic application of this model has shown that the B, Q_{cr}, and n secondary creep constants exhibit stress dependence when comparing constants obtain from high stress (high creep strain rate) experiments with those at lower stress (low strain rate). A high stress modification was proposed as

$$\dot{\varepsilon}_{cr} = \frac{d\varepsilon_{cr}}{dt} = B\,exp\left(\beta\sigma\right)exp\left(\frac{-Q_{cr}}{RT}\right) \tag{2.12}$$

where β is an additional secondary creep constant. An interface of Eq. (2.10) and Eq. (2.12) was proposed by Garofalo [33] as follows

$$\dot{\varepsilon}_{cr} = \frac{d\varepsilon_{cr}}{dt} = B\left(sinh\,\alpha\sigma\right)^{n} exp\left(\frac{-Q_{cr}}{RT}\right)$$
$$\beta = \alpha\sigma \tag{2.13}$$

where the model reverts to Eq. (2.10) when $\alpha\sigma < 0.8$ and reverts to Eq. (2.12) when $\alpha\sigma > 1.2$ [28]. Typically extensive creep tests at both high and low stress levels are not available; therefore, the commonly implemented method is the simple Norton power law with the Arrhenius relation, Eq. (2.11). This selection is repeated in this thesis.

Monkman and Grant [29] observed that creep rupture can be predicted for many alloy systems using the following expression

$$\log\left(t_r\right) + m\log\left(\dot{\varepsilon}_{min}\right) = k_{MG} \tag{2.14}$$

where $\dot{\varepsilon}_{min}$ is the minimum creep strain rate, t_r is the creep rupture time, m is a constant typically about 1.0, and k_{MG} is the referred to as the Monkman-Grant constant. Assuming m is equal to unity furnishes a simplified form of Eq. (2.14) expressed as

$$\dot{\varepsilon}_{min} t_r = k_{MG} \tag{2.15}$$

Previous studies show that the Monkman-Grant relationship produces accurate rupture time predictions for various DS Ni-based superalloys [30,31].

2.4 Tertiary Creep Modeling (Isotropic Creep Damage)

Microstructural damage mechanism occurring during creep can be manifested in a number of ways, such as microcracks, cavities, voids, etc. in increased scale. Typically, creep damage is classed into two forms: transgranular (ductile) damage and intergranular (brittle) damage. Transgranular (ductile) damage arises were slip bands of plasticity forming under high stress and low temperature. Intergranular (brittle) damage is a microcracking process at grain boundaries under high temperature and low stress [34]. Damage is an all inclusive non-recoverable accumulation that exhibits the same dependences as creep deformation: material behavior (i.e., creep constants), temperature, time, and stress. Generally, damage is considered to be in continuum, (i.e., homogenous thought a body) thereby the expression *continuum damage mechanics* (CDM) is used. The damage phenomenon is closely aligned with the creep cracking and has been used to in local and nonlocal CDM approaches to predict creep crack growth. Many

comprehensive lists of creep damage CDM-based formulations are available in literature [15,34,35].

Early work in the characterization of creep damage by Kachanov [5] and Rabotnov [6], introduced the concept of scalar-valued damage evolution expressed as $\dot{\omega} = f(\sigma, \omega)$ where σ is uniaxial stress, ω is the current state damage. Damage is coupled within the creep strain rate via current damage and is expressed as $\dot{\varepsilon}_{cr} = f(\sigma, \omega)$. Within the creep strain equation, arises a net/effective stress which relates the physical space of damage where the presence of microcracks and voids reduces creep strength, to an effective space, where microstructural creep damage is replaced with an effective increase in the applied stress, as conceptualized in Figure 2.4.

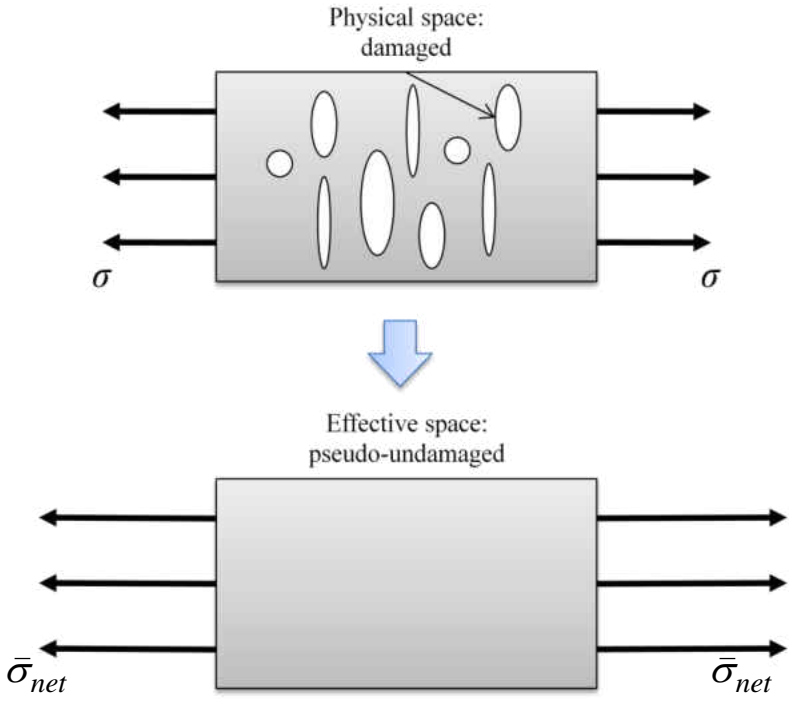

Figure 2.4 - Schematic demonstrating the concept of a physical and effective space

Creep damage can be considered equal to the reduction-in-area from microcrack, cavities, voids, and etc. as a structure undergoes creep deformation. This reduction-in area has been implemented into the net/effective stress of the form

$$\tilde{\sigma} = \bar{\sigma}\frac{A_0}{A_{net}} = \frac{\bar{\sigma}}{\left(1-\frac{A_0 - A_{net}}{A_0}\right)} = \frac{\bar{\sigma}}{(1-\omega)} \tag{2.16}$$

where A_{net} is the current area, A_0 is the initial area, $\bar{\sigma}$ is the von Mises equivalent stress, and $\tilde{\sigma}$ is the net/effective stress. Extensive studies have focused on experimental methods to determine the current state of creep damage within test specimen [36-38].

Phenomenological formulations have been developed to account for damage evolution. Kachanov [5] and Rabotnov [6] followed later by various other authors proposed the following creep rate and damage evolution formulations

$$\dot{\varepsilon}_{cr} = \frac{d\varepsilon_{cr}}{dt} = A\left(\frac{\bar{\sigma}}{1-\omega}\right)^n \tag{2.17}$$

$$\dot{\omega} = \frac{d\omega}{dt} = \frac{M\bar{\sigma}^{\chi}}{(1-\omega)^{\phi}} \tag{2.18}$$

where the creep strain rate is equal to Norton's power law for secondary, Eq. (2.5), with the same associated A and n constants, $\bar{\sigma}$ is von Mises stress, and M, χ, and ϕ are tertiary creep damage constants. Numerous authors have developed specialized formulations based on this fundamental formulation [39-44]. These formulations based around von Mises equivalent stress, have also be generalized for multiaxial states of stress in isotropic materials using elastic compliance tensors and the stress deviator [23]. An isochoric creep behavior (incompressibility) is assumed.

2.5 Void Induced Anisotropy Modeling

In the tertiary creep stage, damage causes the formulation of microcrack, cavities, voids, etc. within the material. It is important to note that void formulation and growth (arise from cavity growth at grain boundaries) is strongly driven by the state of applied stress. Under certain multiaxial conditions, this produces an anisotropic distribution of creep damage within the material; inducing anisotropy.

Literature shows that intergranular damage must be represented by multiple principle damage variables due to induced anisotropy [45,46] in the form of $\boldsymbol{\omega}$ a damage tensor

$$\omega = \begin{bmatrix} \omega_1 & 0 & 0 \\ 0 & \omega_2 & 0 \\ 0 & 0 & \omega_3 \end{bmatrix} \tag{2.19}$$

where each term of damage corresponds to the orthogonal planes of a material. Murakami and Ohno [47] proposed the concept of net-area-reduction into three-dimensions as a second order damage tensor restricted to three planes of symmetry defined

$$\boldsymbol{\omega} = \sum_{i=1}^{3} \omega_i \mathbf{n}_i \otimes \mathbf{n}_i \tag{2.20}$$

where $\mathbf{n}_1$, $\mathbf{n}_2$, and $\mathbf{n}_3$ unit normal vectors and ω_1, ω_2, and ω_3 are the associated principal damage variables as defined in Eq. (2.19).

Damage anisotropy can be indentified in two material classes, aluminum-like and copper-like [34,48]. For aluminum-like materials, damage is mostly distributed isotropically (Figure 2.5a). Aluminum-like materials with a simple stress state (i.e., uniaxial creep tests) can be modeled with isotropic creep damage models [46,49,50]. For copper-like materials, damage evolves independent on each orthogonal plane. The highest rate of damage is observed on the plane perpendicular to the first principal stress direction (Figure 2.5b). Copper-like materials and components undergoing a complex state of stress exhibit an induced anisotropic creep response which must be accounted for with more robust modeling techniques [4]. Models have been developed that can account for both aluminum-like and copper-like materials [45,51]. A number of non-local irreversible thermodynamically-based anisotropic creep damage formulations have been developed; however, numerical complexity has limited application of such techniques [52,53].

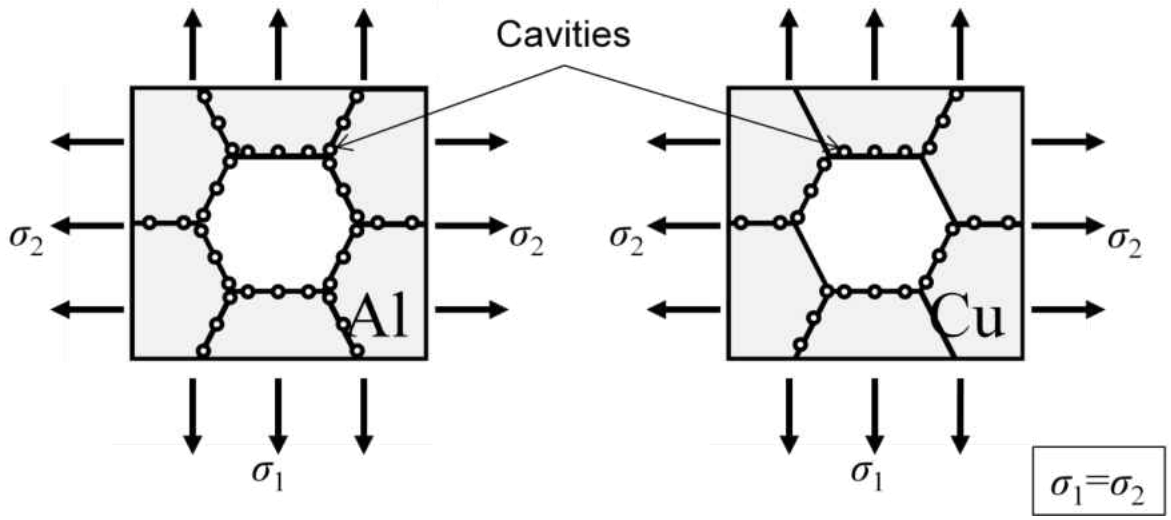

Figure 2.5 - Schematic of cavity growth on grain boundaries for (a) Aluminum and (b) Copper

From the damage tensor a new concept of the net/effective stress tensor arises. Various authors have proposed methods to introduce the damage tensor into a net/effective stress tensor, $\tilde{\boldsymbol{\sigma}}$. [55]. The first method was proposed by Rabotnov [54] as follows

$$\tilde{\boldsymbol{\sigma}} = \boldsymbol{\Omega}\boldsymbol{\sigma} \tag{2.21}$$

where $\boldsymbol{\sigma}$ is Cauchy stress and $\boldsymbol{\Omega}$ is a fourth order damage applied tensor assumed to be symmetric. Numerous alternative methods have been proposed in literature. Murakami and Ohno [47] proposed the following

$$\tilde{\boldsymbol{\sigma}} = \boldsymbol{\sigma} \cdot \left(\mathbf{I} - \boldsymbol{\omega}\right)^{-1} \tag{2.22}$$

where $\boldsymbol{\omega}$ represents a second order damage tensor and $\mathbf{I}$ is a indentify tensor. This expression produces an asymmetric effective stress which violates the concept of symmetric stress and causes an asymmetric inelastic compliance tensors to form. To mitigate this issue Murakami and Ohno [56] proposed a form that includes only the symmetric part expressed as

$$\tilde{\boldsymbol{\sigma}} = \frac{1}{2}\left[\boldsymbol{\sigma} \cdot \left(\mathbf{I} - \boldsymbol{\omega}\right)^{-1} + \left(\mathbf{I} - \boldsymbol{\omega}\right)^{-1} \cdot \boldsymbol{\sigma}\right] \tag{2.23}$$

This effective stress tensor has been used successfully in a number of creep-damage formulations [45,51,57].

Cordebois and Sidoroff [58,59] proposed a symmetric effective stress tensor compatible with thermodynamical requirements of strain energy as follows

$$\tilde{\boldsymbol{\sigma}} = \left(\mathbf{I} - \boldsymbol{\omega}\right)^{-1/2} \cdot \boldsymbol{\sigma} \cdot \left(\mathbf{I} - \boldsymbol{\omega}\right)^{-1/2} \tag{2.24}$$

This formulation has also been used in later study [65]. The deformation of a component depends not only on void induced net-area reduction but also void arrangement. To that end, Murakami and Imaizumi [60] proposed that the deformation characteristics of a material should be fourth order leading to the following effective stress tensor

$$\tilde{\boldsymbol{\sigma}} = \frac{1}{2}\left[\boldsymbol{\Gamma} : \boldsymbol{\sigma} + \left(\boldsymbol{\Gamma} : \boldsymbol{\sigma}\right)^{\mathrm{T}}\right] \tag{2.25}$$

where $\boldsymbol{\Gamma}$ is a fourth order tensor corresponding to damage. Despite the additional numerical complexity require with 4^{th} order tensors, this effective stress tensor has been used in a number of studies [60-62].

Lemaitre and Chaboche [63] postulated that material damage is related to the change in elastic constants. When damage reaches unity elastic strain will not occur as the structural has reach rupture. This provides a method by which both elastic and plastic strains can be controlled and related to the material damage. Extending this concept to multiaxial stress results in an eighth order damage tensor. To reduce numerical complexity, Chaboche [64] proposed a condensed fourth order damage tensor, **D** is related to the elasticity tensor, **E**, in the following form

$$\begin{aligned} \tilde{\mathbf{E}}\left(\mathbf{D}\right) &= \left(\mathbf{I} - \mathbf{D}\right) : \mathbf{E} \\ \mathbf{D} &= \mathbf{I} - \tilde{\mathbf{E}} : \mathbf{E}^{-1} \end{aligned} \tag{2.26}$$

$$\tilde{\boldsymbol{\sigma}} = \left(\mathbf{I} - \mathbf{D}\right)^{-1} : \boldsymbol{\sigma}$$

where is the $\tilde{\mathbf{E}}$ is the effective elasticity tensor and (:) stands for a contraction of rank two.

In general, most induced anisotropic formulations implicitly account for the multiaxial states of stress as induced anisotropy is driven by the multiaxial state of stress. In the case of thin-walled pipes used in power plants, considerable work has been focused around isotropic creep damage modeling [45]. Induced anisotropy has been observed in the creep rupture of pipes under biaxial loading [66]. A schematic of such a pipe is found in Figure 2.6. Literature has demonstrated that anisotropic strength in thin-walled tubular elements is common [67].

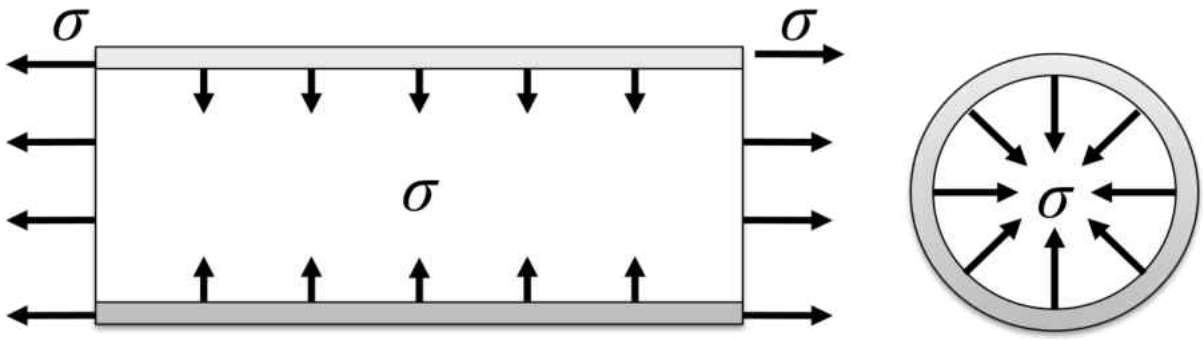

Figure 2.6 - Schematic of pipe under biaxial loading

2.6 Creep Damage Models of Anisotropic Materials

Creep damage exhibits a strong dependence on the orientation of grain structure relative to the state of stress. A schematic of a transversely-isotropic material under multiaxial stress is provided in Figure 2.7. For directionally-solidified materials, where the grain structure is aligned to produce desire material properties, the effect of material orientation must be included in the coupled creep-damage formulation. Induced anisotropy and material anisotropy exacerbates the anisotropic creep damage behavior of anisotropic materials. To account for these issues recently a few authors have produced formulations.

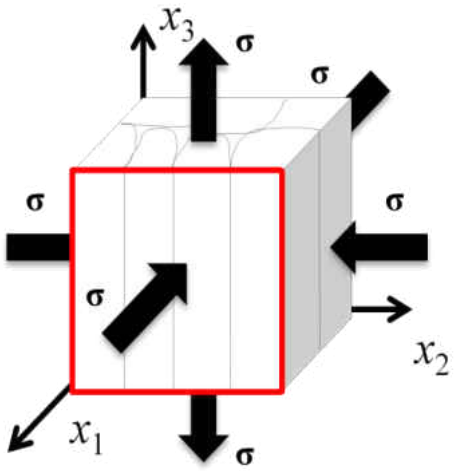

Figure 2.7 - Schematics of transversely-isotropical material under multiaxial loading

Kawai proposed a thermodynamically-based inelasticity model for metal matrix composites [68]. The composite anisotropy is described using a forth order transversely-isotropic tensor **A** of the following form

$$\begin{aligned} A_{abcd} &= \mu\left(\delta_{ac}\delta_{bd}+\delta_{ad}\delta_{cb}\right)+\alpha\left(\delta_{ab}h_c h_d\right) \\ &+\beta\left(\delta_{ac}h_b h_d+\delta_{bc}h_a h_d+\delta_{ad}h_b h_c+\delta_{bd}h_a h_c\right) \\ &-\left(3\alpha+4\beta\right)h_a h_b h_c h_d \end{aligned} \tag{2.27}$$

$$\delta = \delta_{ab}\mathbf{e}_a \otimes \mathbf{e}_b$$

where δ_{ab} is the kronecker delta, h_a are components of the unit vector **h** (=$h_a\mathbf{e}_a$) in the direction of the reinforcing fibers, and α, β, and μ are material constants. The concept of inelastic free energy is introduced. A damage-coupled kinematic hardening formulation is developed. The following kinematic hardening variables are assumed

$$\xi = \sqrt{\frac{3}{2}}\rho\mathbf{n} \quad \mathbf{n} = \sqrt{\frac{3}{2}}\frac{\boldsymbol{\sigma}}{\sigma_{vm}} \tag{2.28}$$

where ρ is a scalar variable. Internal stress **p** is defined as

$$\mathbf{p} = \frac{2}{3}H\xi = \sqrt{\frac{3}{2}}r\mathbf{n} \quad r = H\rho \tag{2.29}$$

where ξ is not independent, ρ is an independent variable, and r is the associated thermodynamic force. Using the damage-coupled kinematic hardening model an isotropic hardening formulation is produced. To model the creep damage behavior the following assumptions are made

$$r = \varphi\sigma_{vm} \qquad \varphi = \frac{K^{1/m}}{K^{1/m}+M^{1/m}} \tag{2.30}$$

where K, M, and m are material constants. Taking the isotropic hardening formulation and introducing these assumptions the desired creep-damage formulation is produced

$$\dot{\varepsilon}^{p} = \frac{3}{2}\left(\frac{1}{1-\omega}\right)^{m+1} \dot{P}_s \frac{\mathbf{An}}{\sqrt{\frac{3}{2}\mathbf{n}\cdot\mathbf{An}}}$$

$$\dot{P}_s = K\sqrt{\mathbf{n}\cdot\mathbf{An}}^{m}\left(1-\varphi\right)^{m}\left\{\sigma_{vm}\right\}^{m} \tag{2.31}$$

$$\dot{\omega} = N\left[|p|\sqrt{\mathbf{n}\cdot\mathbf{Dn}}\right]^{n}\left(\frac{1}{1-\omega}\right)^{k}$$

where $\dot{\varepsilon}^{p}$ is the creep strain rate, $\dot{P}_s$ is a convenient rate related to isotropic hardening, and $\dot{\omega}$ is damage evolution. The Kawai formulation demonstrates a good correlation to the steady-state creep behavior of specimen from 0° to 90°-orientations; however, the tertiary creep-damage behavior at intermediate orientations has not been studied. The formulation is designed for composites materials with arbitrarily oriented reinforcing fibers. The damage mechanisms found in composite materials are not the same as those found in Ni-based superalloys. Within the formulation, damage is a scalar-valued term where anisotropy is applied post-evolution in the hardening rate. The necessary damage tensor does not arise. A better formulation is thus desired.

Early work by Hyde developed a secondary creep model for anisotropic materials [69]. The formulation is based around a multiaxial form of the Norton creep law [25] where the von Mises equivalent stress is replaced with the Hill's anisotropic equivalent stress [26]. The creep strain rate tensor arises using the derivative of Hill's compliance tensor with respect to Cauchy stress. This formulation is a simple and yet powerful formulation for secondary creep of anisotropic materials

$$\boldsymbol{\varepsilon}_{ij}^{cr} = A_{aniso}\sigma_{hill}^{\ n_{aniso}} \frac{d\sigma_{hill}}{d\sigma_{ij}} \tag{2.32}$$

This secondary creep formulation was extended by Peravali-Hyde et al [57] to account for tertiary creep damage. The creep damage behaviors of longitudinal and transverse material orientations are included within the damage evolution tensor as follows

$$\dot{\boldsymbol{\omega}} = \left\{ M_2 \left(1 - \mathbf{v}^{(1)} \cdot \mathbf{n}\right) + \left(\mathbf{v}^{(1)} \cdot \mathbf{n}\right) M_1 \right\} \left[\left(1 - r\right)\mathbf{I} + r\left(\mathbf{v}^{(1)} \otimes \mathbf{v}^{(1)}\right) \right] \tag{2.33}$$

where **v** is a vector representing the first principal stress direction, **n** is a vector corresponding to the longitudinal material behavior , r accounts for void induced anisotropy. The terms M_1 and M_2 are related to the longitudinal and transverse material properties in the following form

$$\begin{aligned} M_1 &= B_1 \left[\alpha_1 S^{(1)} + \left(1 - \alpha_1\right) S_{eq} \right]^{\chi_1} \\ M_2 &= B_2 \left[\alpha_2 S^{(1)} + \left(1 - \alpha_2\right) S_{eq} \right]^{\chi_2} \end{aligned} \tag{2.34}$$

where $S^{(1)}$ is the first principal stress, S_{eq} is some equivalent stress, B_1 and B_2 are material constants, and α_1, α_2, β_1,and β_2 are weight constants. Damage is related back to Cauchy stress via the Murakami symmetric effective stress tensor, Eq. (2.23). Damage is introduced into the creep rate by the effective Hill's equivalent stress, $\tilde{\sigma}_{Hill}$, resulting the following

$$\dot{\varepsilon}_{ij}^{cr} = A_{aniso}\left(\tilde{\sigma}_{Hill}\right)^{n_{anisp}} \frac{\partial \sigma_{Hill}}{\partial \sigma_{ij}} \tag{2.35}$$

This formulation is powerful but examination shows a number of limitations. Within the damage evolution tensor, the creep damage properties are resolved into a scalar value. This leads to the assumption that the creep-damage behavior in a uniaxially loaded DS material specimen is the

same in all orientations and only modified by void induced anisotropy. This produces an inaccurate damage evolution under multiaxial conditions. Creep-damage behavior is orientation-dependent and cannot be resolved as a scalar-valued term. The influence of the state of stress on damage evolution should be implemented more directly using Cauchy stress. The formulation does not include off-axis creep damage behavior. This limitation can be significant for materials that are sustainable to considerable slip plane damage.

2.7 Limitations

In the aerospace, power generation, and pressure vessel and piping industries, anisotropic composites and superalloys are becoming increasingly utilized. In the case of industrial gas turbines drives to increases temperature and pressure, have instigated further use of directionally-solidified materials. Only a limited number of investigations have been performed on the anisotropic creep damage modeling of transversely-isotropic material. In the most recent investigations, either the formulation is not shown to account for off-axis oriented creep damage behavior or damage is considered a scalar-valued term. In this thesis, it is desired to develop a formulation which accurately accounts for tensorial damage evolution and creep deformation of transversely-isotropic materials under any material orientation or state of stress.

CHAPTER THREE: MATERIAL

3.1 A Brief History of Directionally-Solidified Ni-base Superalloy

Nickel-base superalloys are commonly used as turbine blade materials due to their strength, creep-resistance, and corrosion resistance at high temperature. Applying directional solidification techniques, it was discovered that grain boundaries could be minimized perpendicular to the principal load direction and improved rupture strength could be achieved [2]. Early on, application of directionally-solidified (DS) turbine blade technology was strictly found in the aerospace gas turbine industry. A number of DS Ni-base superalloys were developed for cast turbine blades; MAR-M 247, MAR-M 200 Hf (1970), MAR-M 002 (1975), DS IN-6203 (1981), and etc [2]. Nominal compositions are listed in Table 3.1 [72]. Their use in IGTs was restricted. Manufacturing capabilities prohibited the casting of large components in quantity and with significant enough yield to be economically viable. Between the 1960's to the 1980's "aero-derivative" industrial gas turbines, were mainly used as peak power machines. Serious interest began in the 1980's where a series of government sponsored studies for marine IGTs and later land-based IGTs spurred industry development [14]. Drives to improve efficiency through higher firing temperatures and gas velocities necessitated creation of large scale DS turbine blades. General Electric's first application of DS blades in IGTs was on the first stage of the MS5001 unit in 1987 [2]. Over time, improvements in manufacturing techniques and the advent of computer-integrated manufacturing (CIM) has led to common implementation of DS and single-crystalline blades in modern IGTs.

Table 3.1 – Nominal chemical composition (wt%) of first-generation DS superalloys with extensive turbine blade applications [14]

Alloy	C	Cr	Co	Mo	W	Nb	Ta	Al	Ti	B	Zr	Hf	Ni
MAR-M200Hf	0.13	8	9	⋯	12	1	⋯	5	1.9	0.015	0.03	2	Bal.
René 80H	0.16	14	9	4	4	⋯	⋯	3	4.7	0.015	0.01	0.8	Bal.
MAR-M 002	0.15	8	10	⋯	10	⋯	2.6	5.5	1.5	0.015	0.03	1.5	Bal.
MAR-M 247	0.15	8	10	0.6	10	⋯	3	5.5	1	0.015	0.03	1.5	Bal.

3.2 Directionally-Solidified DS GTD-111

The subject material superalloy DS GTD-111, a dual-phase Ni-base superalloy, was developed in the 1987 as a first stage bucket material from uniaxial GTD-111 (derived from Rene' 80 [73]). Directionally-solidified GTD-111 is commonly used in gas turbine applications [74]. General Electric uses the material on the first stage in MS7F/MS9F, MS3002 and MS5002C units [1]. The structure of the grains has been found to produce enhanced creep life, impact strength, corrosion and thermal fatigue resistance compared to its equiaxed counterpart [8,75-77]. The material is transversely-isotropic in the x_1-x_2 plane while different materials properties are found on the x_3 normal plane (Figure 3.1).

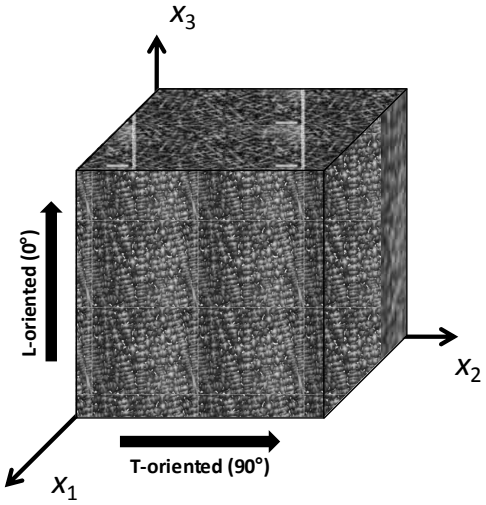

Figure 3.1 - Grain structure of DS GTD-111 with microstructure imposed

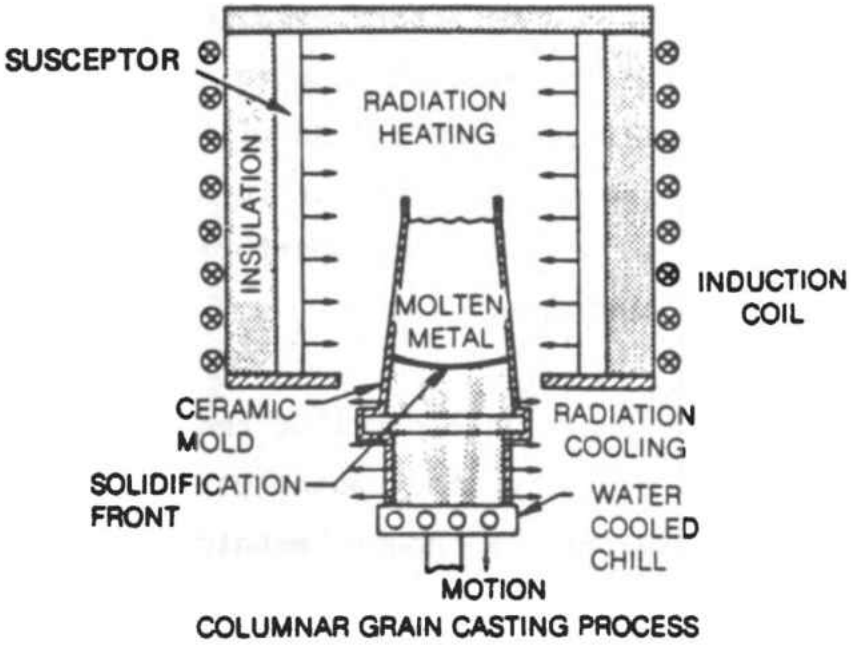

Figure 3.2 - Directional solidification method [78]

During casting, a columnar-grained structure is achieved by controlled withdrawal of a water cooled mold from the hot zone of a furnace. Induction heating methods provide an

adequate thermal gradient that prevents non-uniformities due to solidification in advance of the liquid-solid interface (Figure 3.2) [78]. The long grains inhibit intergranular cracking in the x_1-x_2 orientations, the major cause of failure in turbine blades. These long grains reduce the Young's modulus in the longitudinal (L) orientation, resulting in increased elastic strain and reduced thermal stresses. A consequence of long columnar grains is the (L) orientation exhibits enhanced strength, ductility, and the time before rupture compared to equiaxial (PC) GTD-111.

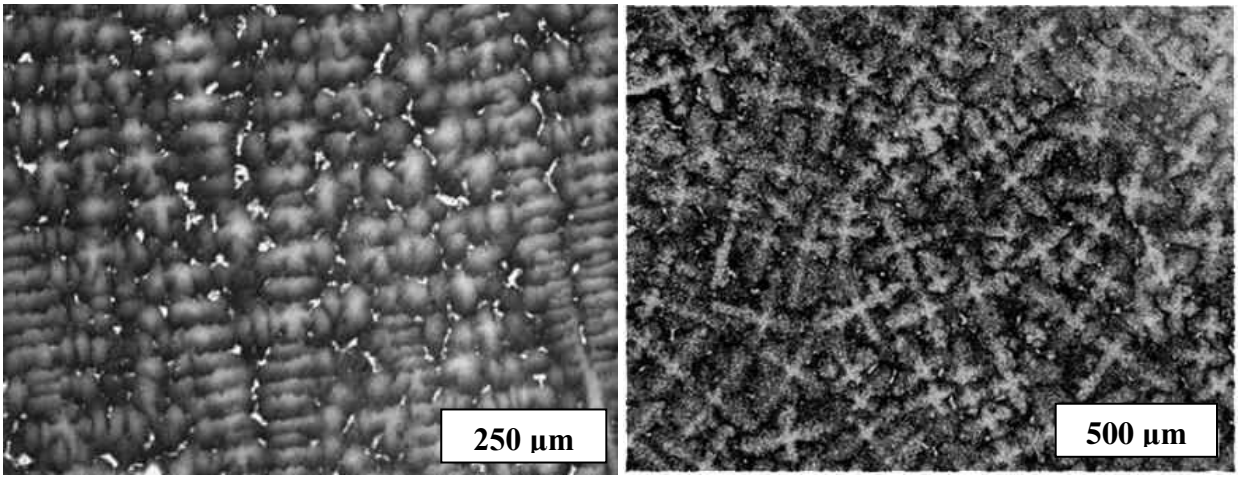

Figure 3.3 - Grain structure of GTD-111 (a) T-oriented Specimen (b) L-oriented Specimen

Through optical and scanning electron microscopy investigations, a closer look at the grain structure of the material was resolved. Figure 3.3 shows the grain structure of both (L) and (T) orientations. The long grains are observed in both (T) orientations. Solidification is shown to

be in the same general direction. Tighter control of the thermal gradient could produce improved grain direction uniformity. The end of the long grains is observed in the (L) orientation.

Microstructurally, DS GTD-111 is formed of a nickel austenite (γ) matrix, bimodal gamma prime (γ') precipitated particles, γ –γ' eutectic, carbides and small amounts of topological close-packed phases σ, δ, η and laves [30,76]. It is an intermetallic consisting of a matrix and (γ') precipitated particles are observed in Figure 3.4. It has a high volume fraction of gamma prime (γ') precipitated particles, (approximately 60%) which imparts enhanced impact strength, high temperature creep and fatigue resistance, and improved corrosion resistance. In the case of PC GTD-111 to obtain the desire microstructure, heat treatment is used then abruptly interrupted leading to a γ-γ' microstructure that is metastable. Polycrystalline GTD-111 contains 0.86 μm and 0.1 μm primary and secondary precipitated particles, respectively. The γ' precipitated particles can morph (shape, arrangement, size, and etc.) to decrease the local energy state of the lattice [79]. In the case of DS GTD-111 the microstructure is formed at the liquid-solid interface, slow cooling during processing produces large grains, 0.5 μm width primary cooling γ' precipitated particles, and 0.05 μm width secondary cooling γ' precipitated particles. The average grain size is 5x5x125 mm [80]. Components with this microstructure can be challenging to repair if extensively damaged, however; a number of methods are under investigation to mitigate this problem [73,77].

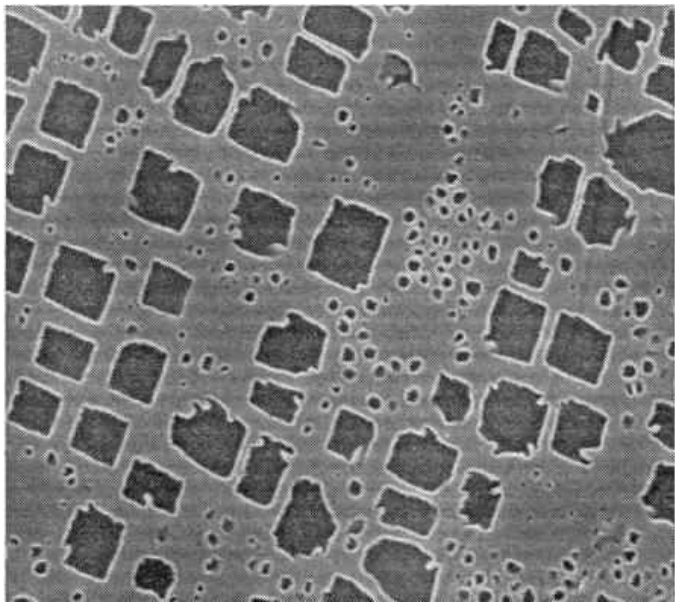

Figure 3.4 - Dark areas are the bimodal γ’ precipitated particles

The nominal composition of DS GTD-111 is found in Table 3.2. The γ matrix phase is FCC austenitic Nickel (Ni), while the γ' precipitated phase is $L1_2$ structured nickel-aluminde (Ni_3Al) with a bimodal distribution [80,81]. Nickel (Ni), aluminum (Al), and chromium (Cr) impart oxidation resistance. The elements titanium (Ti) and molybdenum (Mo) increase the volume fraction of γ' precipitate particles. Titanium is used to control lattice mismatch and the formation of anti-phase boundary energy (APBE). Carbides to pin grain boundaries are formed of carbon (C) and Ti, W, Mo, Cr, and Ta. Chromium (Cr) raises hot corrosion resistance. The elements Cr, Mo, and W are solid solution strengtheners. Various secondary elements are utilized to impart increased ductility, workability, and castability.

Table 3.2 - Nominal chemical composition (wt%) of DS GTD-111 superalloy [1]

Element	Cr	Co	Al	Ti	W	Mo	Ta	C	Zr	B	Fe	Si	Mn	Cu	P	S	Ni
Min	13.7	9.0	2.8	4.7	3.5	1.4	2.5	0.08	0.005	-	-	-	-	-	-	-	Bal.
Max	14.3	10.0	3.2	5.1	4.1	1.7	3.1	0.12	0.040	0.020	0.35	0.3	0.1	0.1	0.015	0.005	Bal.

3.3 Elastic Behavior

In general linear elasticity can be described by the Hooke's law generalized by Cauchy as

$$\begin{aligned} \tau_{ij} &= c_{ijkl} e_{kl} \\ \boldsymbol{\sigma} &= \mathbf{C}_{EL} \boldsymbol{\varepsilon} \end{aligned} \tag{3.1}$$

where τ_{ij} are the components of the Cauchy stress tensor $\boldsymbol{\sigma}$ (9 terms), e_{kl} are the components of the Cauchy strain tensor $\boldsymbol{\varepsilon}$ (9 terms), and c_{ijkl} are components of the elastic stiffness tensor $\mathbf{C}_{EL}$ (81 terms) containing the mechanical properties of the material. Symmetry of the Cauchy stress and strain shear terms (down to 6 independent terms) reduces the 81 components of the elastic stiffness tensor to 36. Rearranging Eq. (3.1) to

$$\begin{aligned} \boldsymbol{\varepsilon} &= \mathbf{S}_{EL} \boldsymbol{\sigma} \\ \mathbf{C}_{EL} &= \left(\mathbf{S}_{EL} \right)^{-1} \end{aligned} \tag{3.2}$$

gives $\mathbf{S}_{EL}$, the elastic compliance tensor. In the case of isotropic (PC) materials linear elasticity takes the following form

$$\boldsymbol{\varepsilon} = \frac{1+\nu}{E} \boldsymbol{\sigma} - \frac{\nu}{E} tr\left(\boldsymbol{\sigma} \right) \mathbf{I} \tag{3.3}$$

and when taken into matrix form produces

$$\begin{bmatrix} e_{11} \\ e_{22} \\ e_{33} \\ e_{12} \\ e_{23} \\ e_{31} \end{bmatrix} = \begin{bmatrix} \frac{1}{E} & -\frac{\nu}{E} & -\frac{\nu}{E} & 0 & 0 & 0 \\ -\frac{\nu}{E} & \frac{1}{E} & -\frac{\nu}{E} & 0 & 0 & 0 \\ -\frac{\nu}{E} & -\frac{\nu}{E} & \frac{1}{E} & 0 & 0 & 0 \\ 0 & 0 & 0 & (1+\nu)/E & 0 & 0 \\ 0 & 0 & 0 & 0 & (1+\nu)/E & 0 \\ 0 & 0 & 0 & 0 & 0 & (1+\nu)/E \end{bmatrix} \begin{bmatrix} \tau_{11} \\ \tau_{22} \\ \tau_{33} \\ \tau_{12} \\ \tau_{23} \\ \tau_{31} \end{bmatrix} \tag{3.4}$$

where only two material properties are necessary to characterize the mechanical behavior; E, elastic modulus and ν, Poisson's ratio.

In the case of the transversely-isotropic materials, first the generalized 36 term elastic stiffness tensor is considered. Symmetry of the elastic stiffness tensor itself demonstrates there are only 21 independent terms. Maxwell's reciprocal theorem brings this down to 9 terms. Symmetry on the x_1-x_2 plane further reduces this to 5 independent terms; however, for the purposes of this research, 6 material constants are available and used. In matrix form, the relation reads as follows

$$\begin{bmatrix} e_{11} \\ e_{22} \\ e_{33} \\ e_{12} \\ e_{23} \\ e_{31} \end{bmatrix} = \begin{bmatrix} \frac{1}{E_p} & -\frac{\nu_p}{E_p} & -\frac{\nu_{zp}}{E_z} & 0 & 0 & 0 \\ -\frac{\nu_p}{E_p} & \frac{1}{E_p} & -\frac{\nu_{zp}}{E_z} & 0 & 0 & 0 \\ -\frac{\nu_{pz}}{E_p} & -\frac{\nu_{pz}}{E_p} & \frac{1}{E_z} & 0 & 0 & 0 \\ 0 & 0 & 0 & \frac{1}{2G_{zp}} & 0 & 0 \\ 0 & 0 & 0 & 0 & \frac{1}{2G_{zp}} & 0 \\ 0 & 0 & 0 & 0 & 0 & \left(\frac{1+\nu_p}{E_p}\right) \end{bmatrix} \begin{bmatrix} \tau_{11} \\ \tau_{22} \\ \tau_{33} \\ \tau_{12} \\ \tau_{23} \\ \tau_{31} \end{bmatrix} \tag{3.5}$$

where the Young's moduli, Poisson's ratios, and shear modulus are E_p, E_z, ν_p, ν_{zp}, ν_{pz}, and G_{zp} respectively. Reduction to 5 independent terms can be done with the following simple relation.

$$\frac{\nu_{zp}}{E_z} = \frac{\nu_{pz}}{E_p} \tag{3.6}$$

The subscripts p and z refer to the x_1-x_2 plane of symmetry and the x_3 normal plane, respectively. These elastic material properties for DS GTD-111 have been characterized for temperature-dependence in Figures 3.6. Using regression analysis, temperature-dependent functions are defined using a third order polynomial of the form

$$A(T) = a_3 T^3 + a_2 T^2 + a_1 T^1 + a_0 \tag{3.7}$$

where the terms of the polynomial, a_i, are in units divide by $°C^i$ and temperature, T is in units $°C$. The terms of the polynomial for each elastic material property is provided in Table 3.3.

Table 3.3 - Polynomial terms for temperature-dependent function of elastic material properties

Constant	*Units*	a_3	a_2	a_1	a_0
E_p	*MPa*	-4.767361E-05	4.574147E-02	-5.474389E+01	1.706597E+05
E_z	*MPa*	-4.030000E-05	3.202410E-02	-4.212748E+01	1.340900E+05
G_{zp}	*MPa*	-4.327437E-05	4.898472E-02	-4.609633E+01	1.205202E+05
ν_p	*unitless*	-8.019135E-11	8.250335E-08	4.378935E-05	1.495837E-01
ν_{zp}	*unitless*	-2.073542E-10	3.524660E-07	-2.775134E-05	4.478843E-01
ν_{pz}	*unitless*	4.588126E-12	3.592104E-08	-2.145816E-05	3.951884E-01

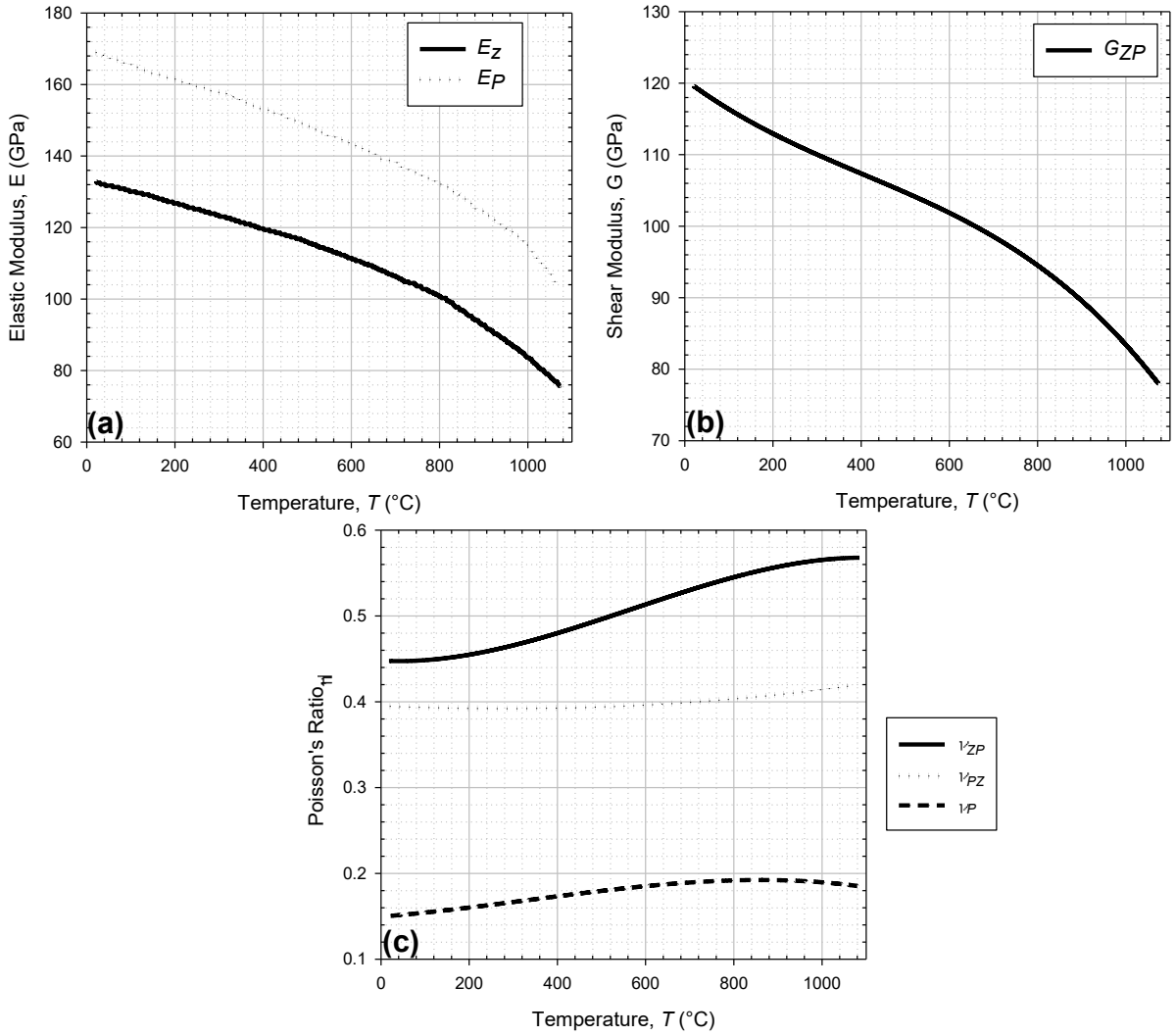

Figure 3.5 – Elastic material properties of DS GTD-111 (a) Young's moduli (b) shear modulus (c) Poisson's ratio

3.4 Plastic Behavior

The morphology of γ' precipitated particles in the γ-γ' microstructure produces lattice mismatch between the γ matrix and γ' precipitated particles phases respectively. The coherency strain, δ, is the strain necessary to maintain a coherent interface between γ and γ' phases, i.e,

$$\delta = 2\left(\frac{a_{\gamma'} - a_{\gamma}}{a_{\gamma'} + a_{\gamma}}\right) \tag{3.8}$$

where $a_{\gamma'}$ and a_{γ} are lattice parameters of the precipitate particles and matrix respectively. Strengthening of the material stems from the cooling γ' precipitated particles. At low temperature dislocations can be found throughout the γ-γ' microstructure. These dislocations inhibit a coherent interface between the two phases. The coherency strain is high, thus the local internal energy at the lattice is high. At high temperature, the morphology of the γ' precipitated particles leads to dislocations mainly found across γ channels between γ' precipitated particles. Dislocations climb and loop around γ' precipitated particles. Dislocations are uniformly distributed within the matrix. The coherency strain is lowered, thus the local internal energy at the lattice is reduced. However, this effect peaks at a critical temperature, afterwards additional thermal energy leads to a degradation of the γ-γ' microstructure that results in rapid weakening of the material.

The morphology of the γ' precipitated particles has a profound effect on the material properties of DS GTD-111. The strength of γ' is found to increase as temperature increases while γ is found to weaken as temperature increases. In general, the law of mixtures for composite

materials can be adapted to estimate the strength developed due to solid-solution hardening; however, when precipitated particles account for 50%-70% of volume fraction, precipitation hardening has a great effect on the material strength [82]. In the case of DS GTD-111, γ' precipitated particles account for approximately 60% of the volume fraction. The material exhibits a slight strengthening behavior in both the ultimate tensile strength and 0.2% yield strength of DS GTD-111 that can be observed between 649 and 760°C in Table 3.4.

Table 3.4 - Yield strength and ultimate tensile strength of DS GTD-111

	Temperature		Yield Strength, σ_{YS}		Ultimate Tensile Strength, σ_{UTS}	
	(°C)	(°F)	(MPa)	(ksi)	(MPa)	(ksi)
(L)	21	70	977	142	1115	162
	649	1200	825	120	1110	161
	760	1400	903	131	1108	161
	871	1600	669	97	802	116
(T)	21	70	817	119	837	121
	649	1200	731	106	876	127
	760	1400	776	113	974	141
	871	1600	666	97	834	121

Figure 3.6 contains a comparison between equiaxial PC GTD-111 and DS GTD-111 [80]. For both materials γ' thermally activated strengthening is observed. The T orientation is found to be slightly less strong than the PC GTD-111 at low temperatures but is stronger at high temperature. The L orientation exhibits enhanced ductility and strength compared to PC GTD-111. The directionally-solidified nature of the grain structure of DS GTD-111 improves creep resistance.

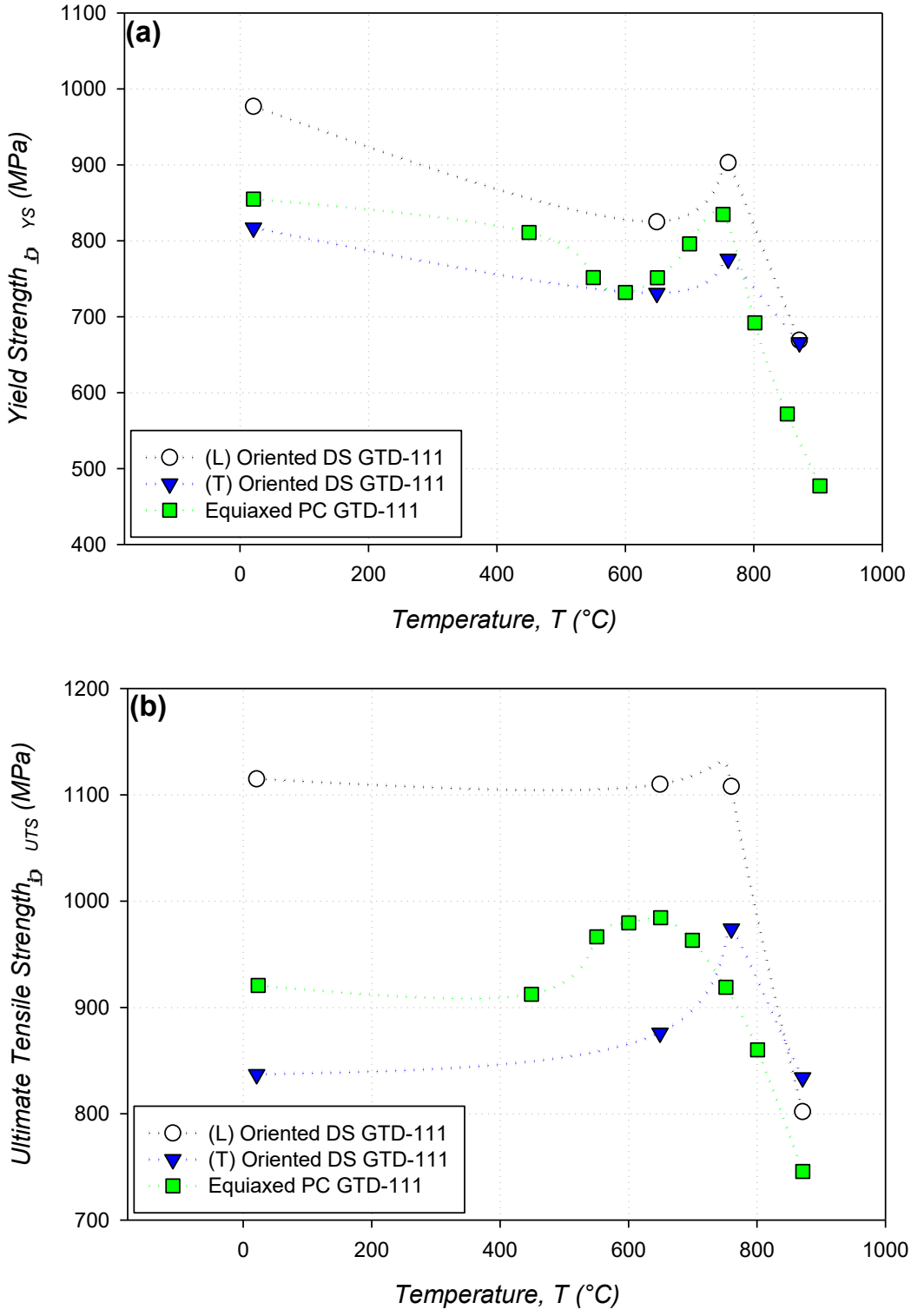

Figure 3.6 – Plastic material properties of DS GTD-111 (a) yield strength [80] (b) ultimate yensile strength [30]

3.5 Creep Test Data

Creep deformation and rupture experiments were conducted on L, T, and 45°-oriented specimen of DS GTD-111 according to an ASTM standard E-139 [83] at temperatures ranging from 649 to 982°C and various uniaxial tensile stress levels to determine the creep response of the material over a wide range of conditions. A list of all creep deformation and rupture tests used is shown in Table 3.5 [30,84]. It should be noted that the experiment at 649°C and 896MPa is above the yield strength and thus exhibits considerable plasticity. For all cases except those at 649°C, time-independent plasticity is ignored. Generally, creep rupture time increases with either decreasing applied stress or decreasing temperature. Specimens were obtained from a three batches of DS GTD-111, where each batch exhibited a slightly different creep response. In all the creep rupture data, scatter is present. This form of scatter, which is common in creep rupture data, is due to inconsistency in the microstructure or inadequate control of the heat treatment process. It also is a result of very slight differences that occur during testing. Manufacturers commonly use least-square linear regression analysis to determine the minimum creep rupture life of an alloy while neglecting scatter. Advancements by Zuo and coworkers [85] show that the maximum likelihood method produces more accurate predictions of creep-rupture life.

Table 3.5 - Creep deformation and rupture data for DS GTD-111 [30]

	Orientation	Temperature		Stress		Rupture Strain	Rupture Time	Estimated Primary Creep
		(°C)	(°F)	MPa	ksi	(%)	(hr)	(%)
1	**L**	649	1200	896	130	4.9	465.9	0.13%
2	**L**	760	1400	408	60	15.0	5624.0	0.30%
3	**L**	760	1400	613	89	13.2	243.6	0.24%
4	**T**	760	1400	517	75	6.9	375.7	0.60%
5	**T**	760	1400	613	89	1.8	42.6	0.36%
6	**L**	816	1500	455	66	21.5	321.5	0.26%
7	**T**	816	1500	455	66	4.6	127.0	0.21%
8	**L**	871	1600	241	35	18.8	2149.0	NA
9	**L**	871	1600	289	42	11.7	672.2	0.09%
10	**T**	871	1600	241	35	7.6	980.2	NA
11	**T**	871	1600	289	42	5.1	635.3	NA
12	**L**	940	1724	244	35	14.1	68.7	0.07%
13	**T**	940	1724	244	35	3.8	62.5	0.07%
14	**L**	982	1800	124	18	17.8	821.3	0.01%
15	**L**	982	1800	145	21	9.1	301.7	NA
16*	**45°**	871	1600	289	42	6.0	455.0	0.50%

*[84]

From the creep deformation and rupture experiments, the subject material DS GTD-111 exhibits primary, secondary, and tertiary creep strain depending on the combination of test temperature and stress, and material orientation. Based on these strain responses, the deformation mechanisms can be inferred from investigations that complemented mechanical experimentation with microscopic analysis. Deformation at 649°C at low stresses and short times is mostly due to elastic strain, along with primary and secondary creep. At higher temperatures (760°C and above), deformation is dominated by secondary and tertiary creep facilitated by the coalescence of grain boundary voids into microcracks.

3.6 Secondary Creep Constants

In order for the tertiary creep damage model to correctly predict creep deformation up to rupture, the secondary creep constants for DS GTD-111 need to be determined. Earlier work shows the classical Norton creep power law works well in predicting the steady-state strain found in the secondary regime. The Norton power law for secondary creep is as follows

$$\dot{\varepsilon}_{cr} = A\bar{\sigma}^{n}, \tag{3.9}$$

where A and n are the creep strain coefficient and exponent, respectively, and $\bar{\sigma}$ is the von Mises effective stress. Simple analytical methods can be used to determine the secondary creep constants, A and n at various temperatures [86]. These analytical methods, although good, require duplication of creep tests and then averaging to eliminate scatter. In the case of this study, limited test data is available, thus a numerical approach is used. The minimum creep strain rate and the specimen stress load are put into the Norton power law and a system solving algorithm is used to determine optimal A and n constants. For most materials, traditional methods tend to find A and n to be stress-independent but there are exceptions [87]. Hyde [88] showed for a Ni-base alloy Waspaloy that once a critical value of applied stress is reached the relationship between minimum creep strain and stress evolves. This leads to a two-stage relationship and stress dependence of the secondary material constants. Sajjadi and Nategh show that for equiaxial GTD-111 there is an abrupt shift in deformation mechanism at intermediate temperature and stress levels what causes a breakdown of power law creep [76]. Table 3.5 shows that for the collected creep deformation data, at the maximum two stress levels per temperature

were conducted. Any possible stress dependence of A and n is not visible in the current data; therefore, stress dependence of the secondary material constants is neglected.

Dorn [32] suggested that temperature-dependence should take the form of an Arrhenius equation

$$A(T) = B\,exp\left(\frac{-Q_{cr}}{RT}\right) \tag{3.10}$$

where B is the pre-exponential factor in units $MPa^{-1}\ hr^{-1}$, Q_{cr} is the activation energy for creep deformation in units $J\ mol^{-1}$, R is the universal gas constant 8.314 $J\ mol^{-1}\ K$, and T is temperature in units Kelvin. Jeong [89] demonstrated that while under stress relaxation short term transient behavior occurs where Q_{cr} and n are both stress-dependent at relativity short times (e.g. less than 10 minutes). After this transient stage, the Norton power law becomes independent of initial stress and strain. This transient behavior has been neglected here since the current study focuses on longer periods (e.g. 1-100,000 hours). For DS GTD-111, the activation energy for creep deformation, Q_{cr}, has been found as 3773 and 3636 *KJ/mol*. These values are much higher than the activation energy of self diffusion for equaxial PC GTD-111 and other polycrystalline Ni-base superalloys [76,24]. Ibanez suggests dislocation climbing is not a viable creep mechanism for DS GTD-111 [90]. The larger activation energy is a result of creep controlled dislocation motion, a common occurrence in multi-phase superalloys. Previously, efforts to model the secondary creep constants for DS GTD-111 were not easily fittable into temperature-dependent form [30]. Temperature-dependence of A and n in this study is proposed as

$$A(T) = A_0\,exp\left(A_1 T\right) \tag{3.11}$$

$$n(T) = n_1 T + n_0 \tag{3.12}$$

where A_0, A_1, n_0, and n_1 are constants and T is in units Celsius. A plot of these functions in Figure 3.7 shows accurate predictions (R^2>0.9672). Using these formulations temperature-dependence of secondary creep can be modeled.

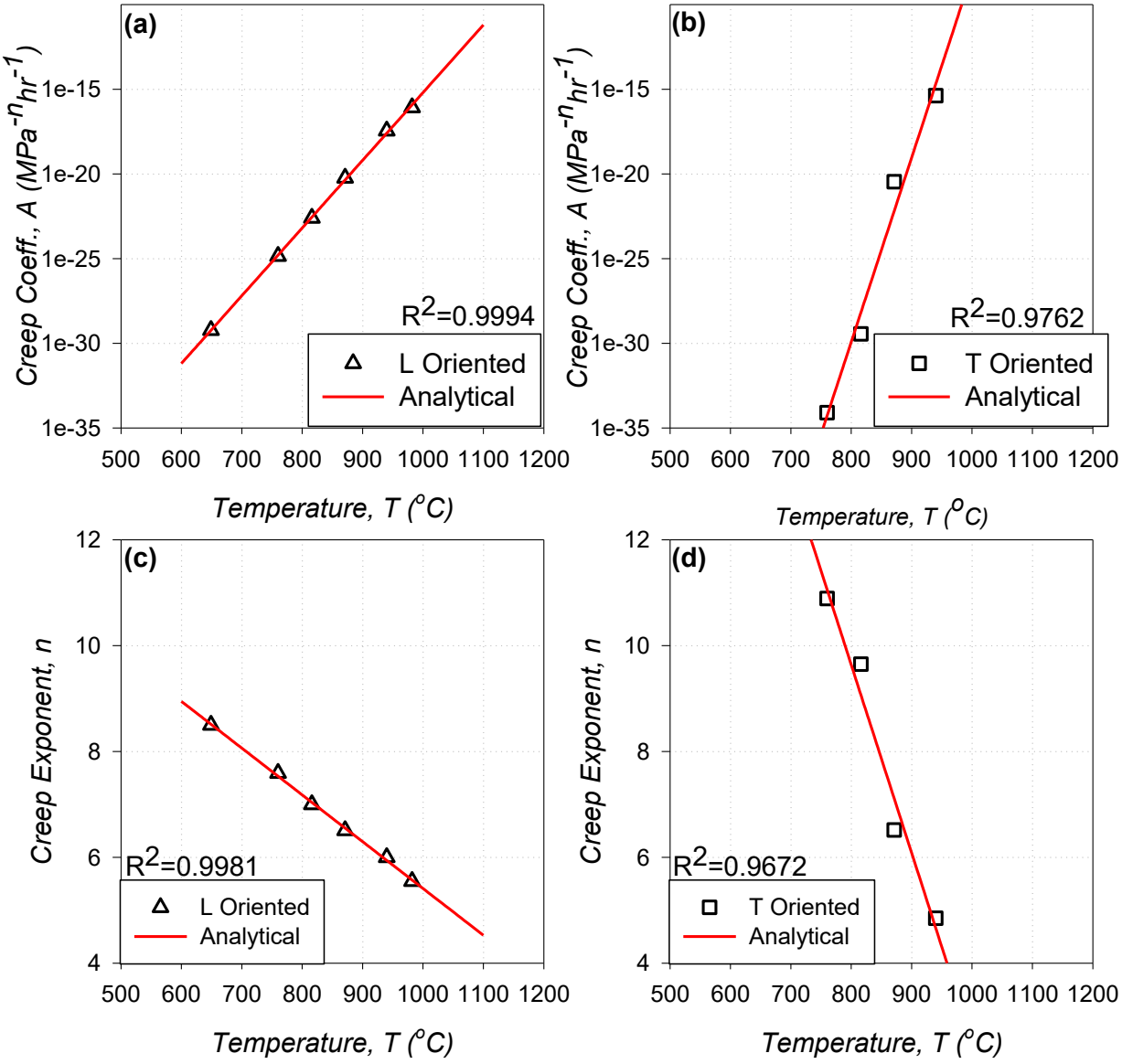

Figure 3.7 - Secondary creep constants for DS GTD-111

Limited creep test experimental data is available for 45°-oriented specimen; therefore, temperature-dependence of the secondary creep constants for a 45°-oriented specimen is not considered. Using traditional methods, the *A* and *n* constants at a temperature of 871°C are obtained as 1.374E-23 and 7.6 respectively and can be found in Figure 3.8.

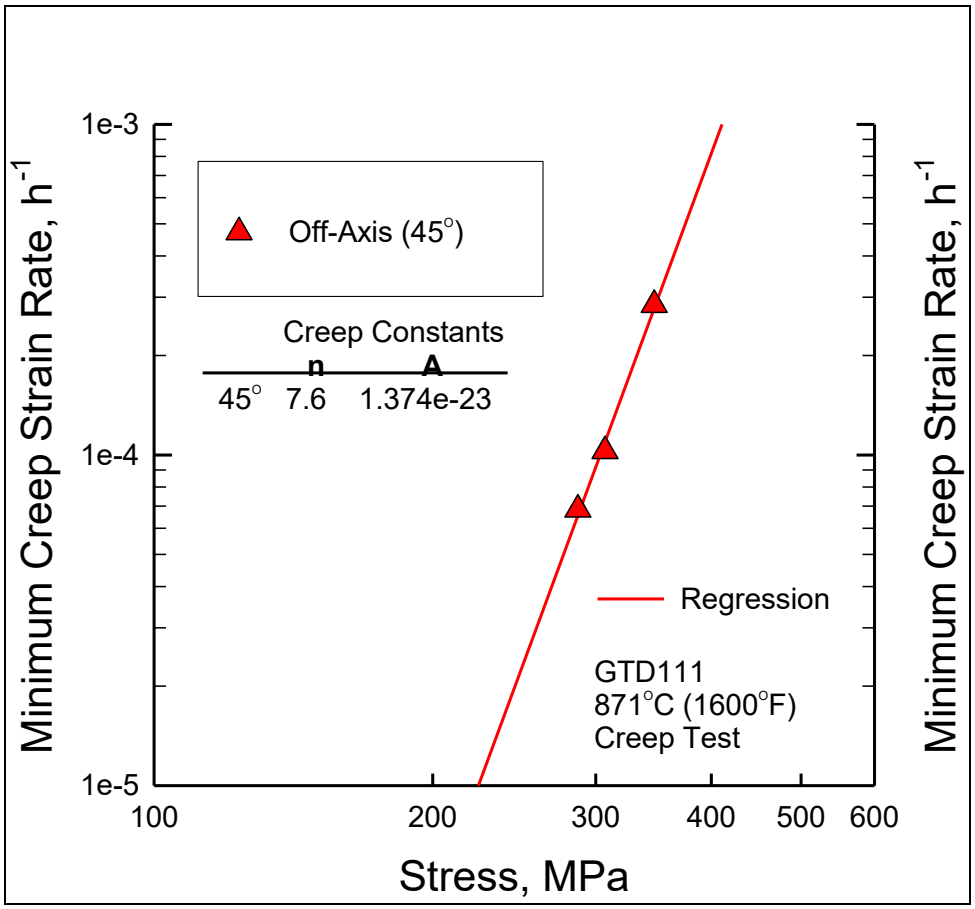

Figure 3.8 - Secondary creep constants for DS GTD-111 (45°-oriented specimen)

CHAPTER FOUR: ISOTROPIC CREEP DAMAGE MODEL

4.1 Introduction

In order to produce an accurate multiaxial representation of the creep deformation of a transversely-isotropic material it is first necessary to accurately model the uniaxial x_1-x_2 plane of symmetry and x_3 normal represented by L and T specimen, respectively.

In the current study, the classical isotropic Kachanov-Rabotnov model for tertiary creep damage is implemented in the non-linear FEA software, ANSYS® [91]. Creep deformation and rupture experiments are conducted on samples of the DS GTD-111 Ni-base superalloy, tested at temperatures between 649 and 982°C and two orientations: longitudinally (L) and transversely (T) oriented (Table 3.5). The secondary creep constants previously determined in Chap. 3.5 are used. A rupture prediction model is derived from the Kachanov-Rabotnov model and used to determine an initial guess of damage constants. The simulated annealing optimization routine is utilized to determine the optimal damage constants.

4.2 Constitutive Model

A constitutive model must be developed which can account for several creep regimes: secondary and tertiary. In the current case, the development of a primary creep model is not

necessary due to the minimal amount of primary creep strain recorded during creep tests. The relatively short regime is approximated by a static primary creep strain applied upon loading. The first step in developing an adequate model is selection of a formulation which can account for steady-state secondary creep. The Norton Power law for creep, a first order differential equation for the creep strain rate is used

$$\dot{\varepsilon}_{cr} = \frac{d\varepsilon_{cr}}{dt} = A\bar{\sigma}^{n} \tag{4.1}$$

where A and n are the creep strain coefficient and exponent and $\bar{\sigma}$ is the Von Mises effective stress. Temperature-dependence of the A and n constants is discussed in Chap. 3.5.

To account for tertiary creep a continuum damage mechanics model was applied. This involves the use of a damage variable which accounts for microstructural evolution. During the transition from secondary to tertiary creep, microcracks along grain boundaries of polycrystalline materials act as stress concentrations. The amplified stress due to local reduction of cross-sectional area is the phenomenological basis of the damage variable, ω, that is coupled with the creep strain rate and has a stress-dependent evolution, i.e.,

$$\begin{aligned} \dot{\varepsilon}_{cr} &= \dot{\varepsilon}_{cr}\left(\bar{\sigma}, T, \omega, \ldots\right) \\ \dot{\omega} &= \dot{\omega}\left(\bar{\sigma}, T, \omega, \ldots\right) \end{aligned} \tag{4.2}$$

A straightforward formulation implies that the damage variable is the net reduction in cross-sectional area due to the presence of defects such as voids and/or cracks, e.g.

$$\bar{\sigma}_{net} = \bar{\sigma}\frac{A_0}{A_{net}} = \frac{\bar{\sigma}}{\left(1-\frac{A_0 - A_{net}}{A_0}\right)} = \frac{\bar{\sigma}}{(1-\omega)} \tag{4.3}$$

where $\bar{\sigma}_{net}$ is called the net (area reduction) stress, A_0 is the undeformed area, A_{net} is the reduced area due to deformation, and ω is the damage variable. Some models account for the variety of physically observed creep damage mechanisms with multiple damage variables [92]. An essential feature of damage required for application of continuum damage mechanics concepts is a continuous distribution of damage. Generally, micro-defect interaction (in terms of stress fields, strain fields, driving forces) is relatively weak until impingement or coalescence is imminent.

The damage variable is applied in a first order differential equation for the damage evolution and coupled with the creep strain rate. Work by Kachanov [5] and later Rabotnov [6] led to the coupled Kachanov-Rabotnov equations of creep

$$\dot{\varepsilon}_{cr} = \frac{d\varepsilon_{cr}}{dt} = A\left(\frac{\bar{\sigma}}{1-\omega}\right)^n \tag{4.4}$$

$$\dot{\omega} = \frac{d\omega}{dt} = \frac{M\bar{\sigma}^{\chi}}{(1-\omega)^{\phi}} \tag{4.5}$$

where the coefficient A and M and the exponents n, χ, and ϕ are damage constants. Johnson and colleagues [96] show the importance of modeling beyond simple uniaxial tension conditions and focused on multi-axial states of stress. A model which can implement complex states of stress is necessary to accurately model gas turbine components. Tensile/compressive asymmetry and

multi-axial behavior can be accounted for by using the damage evolution equation developed by Hayhurst [95]

$$\dot{\omega} = \frac{d\omega}{dt} = \frac{M\sigma_r^{\chi}}{\left(1-\omega\right)^{\phi}} \tag{4.6}$$

$$\sigma_r = \left\langle \alpha\sigma_1 + 3\beta\sigma_m + \left(1-\alpha-\beta\right)\bar{\sigma} \right\rangle \cdot \tag{4.7}$$

where the Von Mises stress, $\bar{\sigma}$ is replaced by the Hayhurst triaxial stress, σ_r. The Hayhurst triaxial stress is related to the principal stress, σ_1, hydrostatic (mean) stress, σ_m, and the Von Mises effective stress, $\bar{\sigma}$, and includes two weight factors α and β that are determined from multiaxial creep experiments. The Hayhurst triaxial stress becomes incompressible when $\alpha + 2\beta \geq 1$. More recent investigations have extended this damage evolution description to account for anisotropic damage of isotropic materials resulting from multiaxial states of stress [47,[51]. In these cases, damage is described by a second-rank tensor.

Using Eqs. (4.4), (4.6), and (4.7), a suitable tertiary creep damage model is resolved. The tertiary creep damage model can be reverted back to secondary creep when $M = 0$. Damage evolution becomes zero and the strain rate reverts back to the Norton power law for secondary creep with the exception that $\bar{\sigma}$ is replaced by σ_r. This is a useful property that has been exploited in a previous study to determine the transition time when the dominant creep regime shifts from secondary to tertiary creep [24].

This tertiary creep damage model has been used in a variety of studies of turbine and rotor materials. The constants A, n, M, χ, and ϕ are considered material properties. For example,

in Waspaloy at 700°C, $A = 9.23\times10^{-34}$ $MPa^{-n}hr^{-1}$, $n = 10.65$, $M = 1.18\times10^{-25}$ $MPa^{-\chi}hr^{-1}$, $\chi = 8.13$, and $\phi = 13.0$ [93]. For stainless steel at 650°C, $A = 2.13\times10^{-13}$ $MPa^{-n}hr^{-1}$, $n = 3.5$, $M = 9.0\times10^{-10}$ $MPa^{-\chi}hr^{-1}$, and $\chi = \phi = 2.8$ [94]. Stewart and Gordon show that by determining the creep material constants at multiple temperatures for Ni-base alloy IN-617, functions can be developed that introducing temperature-dependence to the tertiary creep damage model [24]. This has the effect of making the creep strain rate and damage evolution equations temperature dependent. As temperature changes over time, the material constants change, altering the creep strain rate and damage evolution predicted at the current time step.

4.3 Rupture Prediction Model

A prediction of the rupture time can be achieved using the damage evolution equation (4.6). Integration of the equation leads to the following

$$\begin{aligned} (1-\omega)^{\phi}\, d\omega &= M\sigma_r^{\chi}\, dt \\ -\frac{(1-\omega)^{\phi}}{1+\phi}\Bigg|_{\omega_o}^{\omega} &= M\sigma_r^{\chi}\Big|_{t_o}^{t} \end{aligned} \tag{4.8}$$

where under creep experiment conditions, stress is constant and t_o and ω_o equal 0.0. Simplification leads to the rupture time and damage predictions

$$t = \left[1-(1-\omega)^{\phi+1}\right]\left[(\phi+1)M\sigma_r^{\chi}\right]^{-1} \tag{4.9}$$

$$\omega(t) = 1 - \left[1 - (\phi + 1) M \sigma_r^{\chi} t\right]^{\frac{1}{\phi+1}} \tag{4.10}$$

When adequate damage constants are determined, a quality prediction of rupture time can be achieved. Plotting stress versus rupture time on a log scale produces a linear relationship similar to what is observed for brittle failure of other PC Ni-base superalloys [43]. However; under short life and high stress conditions (particularly near the ultimate tensile strength) the rupture time predictions deteriorate. This is due to the formulation not directly including the effects of the ultimate tensile strength in damage evolution. Applying it would provide a criterion by which the model could converge to the instantaneous failure when loaded beyond the ultimate tensile strength. Under actual service conditions, components are typically under significantly less stress and designed for longer life than the typical creep test. Secondary creep is dominant therefore; the rupture time equation is quite useful in predicting failure. Additionally, the rupture time equation can be applied to determine an initial guess set of damage constants. This can be done through optimization when it is assumed that $\omega(t)$ equals 1.0 at the experimental rupture time, t_r.

4.4 Numerical Approach

The constitutive model described in Eqs. (4.4), (4.6), and (4.7) has been implemented in a general-purpose finite element analysis (FEA) software in order to determine the constants for the constitutive model used in the secondary-tertiary creep formulation. The formulation was implemented into a FORTRAN subroutine in the form of a usercreep.f user-programmable

feature (UPF) in ANSYS. The subroutine is incorporated with an implicit integration algorithm. This backward Euler integration algorithm is more accurate over long time periods than other practical numerical integration methods. This allows larger time steps that reduce the numerical solve time. Since the viscoplastic/creep behavior of materials is significant at extended histories, the backward Euler method is the desired method for integration of creep constitutive models [97].

This implementation allows for the update of the internal state variable, ω. Initially, ω equals 0.0 and during loading, ω increases. To prevent the singularity that is caused by rupture (e.g. ω equals 1.0), the damage is restricted to a maximum of 0.90. Comparison of creep rupture data to numerical simulations shows that rupture occurs at ω between 0.4 and 0.6; therefore, rupture can be achieved before a singularity occurs. To prevent an excessive model solve time and large deformation errors, a simulation was terminated once the total strain reached 100%. If needed, this model can be applied with time-independent and time-dependent plasticity models in a straightforward manner.

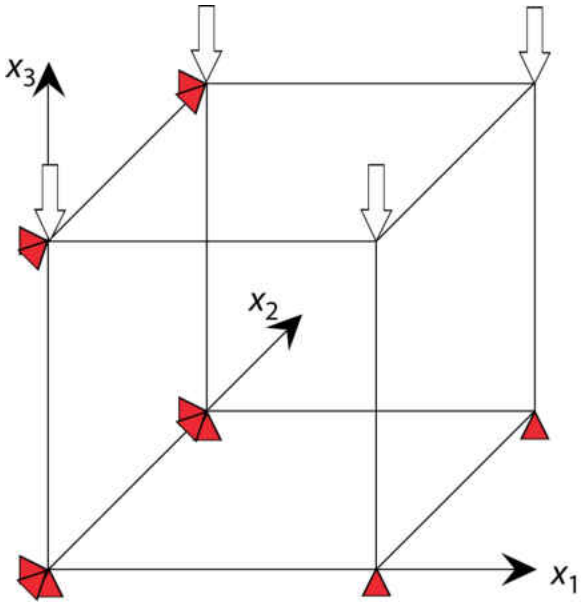

Figure 4.1 - Single element FEM geometry used with force and displacement applied

The UPF has been used to simulate the temperature and stress loading conditions of a series of uniaxial creep and rupture experiments. A single, solid, three-dimensional, 8-noded element was used, and the appropriate initial and boundary conditions were applied to numerically simulate a uniaxial creep tests. The loads and temperatures applied numerically simulated those of the obtained creep rupture experiments. Figure 4.1 demonstrates how these conditions are applied on the FEM geometry. The constant axial force load experience during tensile testing was applied as a force load on the top surface of the element. A uniform temperature was applied across the element. Displacement controls were set to match the constraints experienced during tensile testing. These conditions lead to an accurate assessment of the creep deformation within a single element model. Histories of creep deformation, $\varepsilon_{cr}(t)$, were recorded to a data file and subsequently compared with experiments. Using this method,

expansion beyond a single element to multi-element simulations will produce an accurate measure of creep deformation.

4.5 Optimization

To determine the creep damage parameters M, χ, and ϕ, an automated optimization routine, called uSHARP, was used [98]. Screenshots of this optimization software are available in Appendix A. Finite element model (FEM) simulations were carried out and compared with their corresponding experimental data sets. In each case, the stress and temperature specified in the ANSYS simulation matched those of the corresponding experimental data set. ANSYS simulations were then executed in an iterative optimization process until the least squares values between the simulated and experimental datasets were minimized. The least squares objective function was based on creep strain, and is presented as

$$S = \frac{\sum_{i=1}^{m} \left(\varepsilon_{FEM,i} - \varepsilon_{EXP,i} \right)^2}{m} \tag{4.11}$$

where $\varepsilon_{FEM,i}$ and $\varepsilon_{EXP,i}$ are the strain values obtained by FEM simulation and experimental testing, respectively. The parameter m is the total number of data points resulting from an individual simulation used to determine the least squares value during a single iteration. In Eq. (4.11), the objective function assumes the strains correspond to an identical load time. Since the

cardinality of the data sets always differed, an automated smoothing routine was carefully developed to unify time basis of the data. This feature is built into uSHARP.

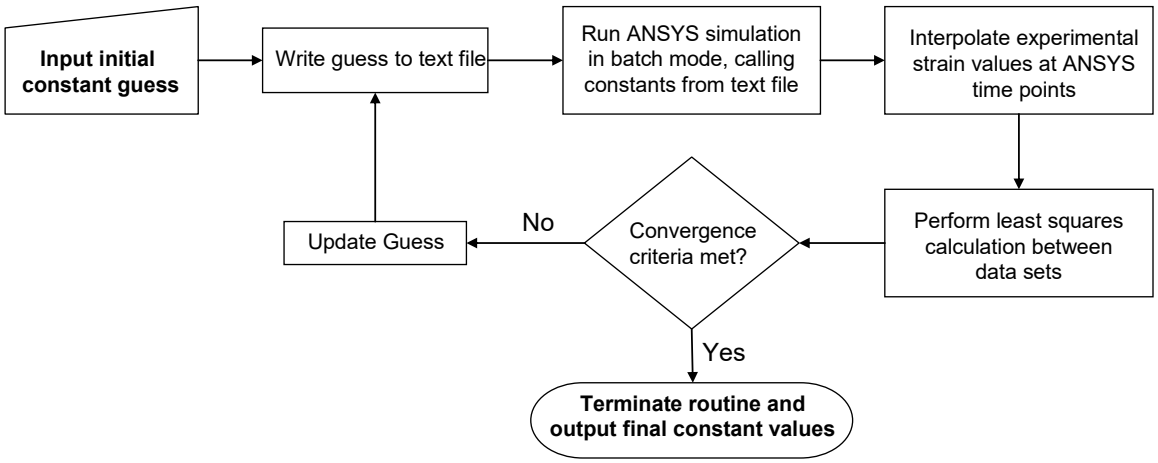

Figure 4.2 - uSHARP optimization procedure [98]

The Corana et al. simulated annealing multimodal algorithm was used as the optimization algorithm [99]. It is a robust optimizer which has the capability to find the global optimal by both uphill and downhill moves. This capability allows it to effectively climb out of local minima when necessary. Additionally, its implementation into the uSHARP routine was very straightforward [100]. The uSHARP code automatically executes ANSYS at each iteration, evaluates the objective function, and updates the guess for the material constants on the basis of the simulated annealing algorithm. An overview of the optimization procedure used can be seen in Figure 4.2.

Due to simulated annealing being a non-conventional algorithm, it requires an extensive number of iterations before final convergence to the global optima occurs. To reduce solve time, the solve space or target range to be optimized needed to be determined. To do this, the lowest and highest temperature experiments were conducted first. The solve space was set such that the lower and upper bound for all three damage constants was $\pm 1.0 \text{x} 10^{10}$. The results of these simulations were analyzed and target ranges for the intermediate temperature experiments was set as $0.0 \leq M \leq 700$, $1.7 \leq \chi \leq 2.3$, and $0.0 \leq \phi \leq 60$. The simulated annealing routine requires an initial guess. To determine a suitable set of initial constants the derived rupture time model, Eq. (4.9), was compared with experimental data. Manual iteration of the M, χ, and ϕ was performed until the relative error between experimental and simulated rupture time was minimized. This produced constants which were readily applicable in the uSHARP routine.

The Kachanov-Rabotnov damage evolution equations do not account for primary creep. Primary creep strain was therefore approximated from experimental data and added to the finite element solution. These modified creep strain values were applied in the least squares calculations and plotted with the experimental data. As a result, the secondary creep regions of each curve conferred a better fit on the tertiary creep region. This ensured that more accurate material constants were determined. The primary creep values used for each dataset are presented in Table 4.1.

As the optimization routine progressed, the least squares values were recorded at every iteration. This provided a clear display of convergence using the simulated annealing algorithm, as presented for every tenth iteration in Figure 4.3. It is observed that simulated annealing

continuously moved both up and downhill towards a minimal least squares value. Depending on the quality of the initial guess the number of iterations till convergence greatly varies. A least square value less than 10 was necessary during each optimization run. Otherwise, an improved initial guess would be selected and optimization preformed again until a suitable value was obtained.

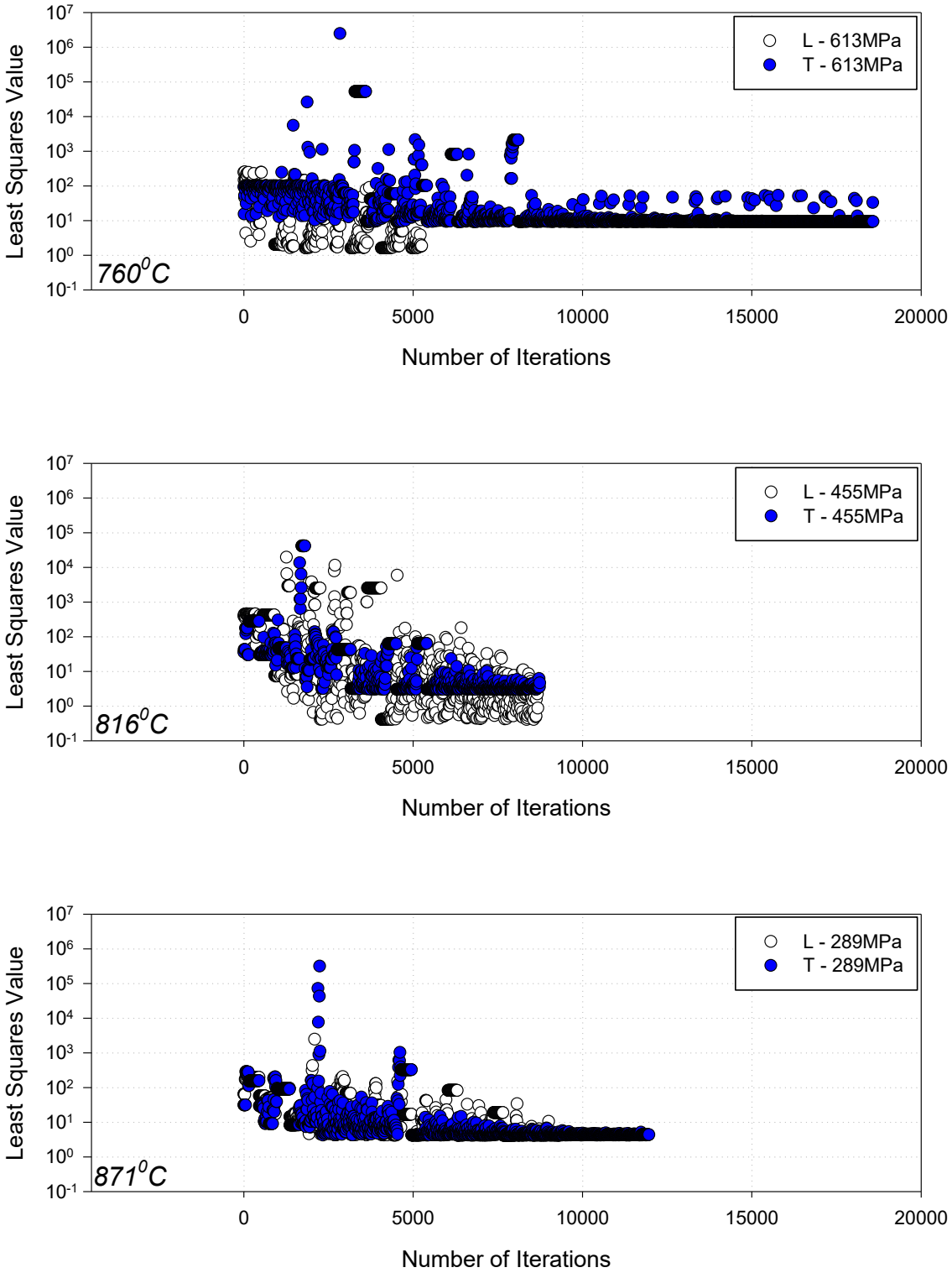

Figure 4.3. Least squares values presented for every tenth iteration during optimization

Table 4.1 – Primary creep and least squares values for DS GTD-111

	Orientation	Temperature		Stress		Primary Creep Strain	Least Squares Value
		(°C)	(°F)	MPa	Ksi	(%)	
1*	L	649	1200	896	130	0.13	2.0588
2*	L	760	1400	408	60	0.30	9.6451
3	L	760	1400	613	89	0.24	1.6003
4	T	760	1400	517	75	0.60	9.029
5	T	760	1400	613	89	0.36	9.2964
6	L	816	1500	455	66	0.26	0.4058
7	T	816	1500	455	66	0.21	2.9972
8	L	871	1600	241	35	NA	3.7922
9	L	871	1600	289	42	0.09	4.1546
10	T	871	1600	241	35	NA	8.3388
11	T	871	1600	289	42	NA	4.2331
12	L	940	1724	244	35	0.07	0.8296
13*	T	940	1724	244	35	0.07	7.7568
14	L	982	1800	124	18	0.01	5.7186
15	L	982	1800	145	21	NA	0.6798
16	45	871	1600	289	42	0.005	1.8893

*Manually Fit

A list of the least squares values found is in Table 4.1. In all cases, the optimization routine on average produces better least square values for the L-orientation. This can be attributed to the slight variability in alignment of the long grains between different specimens. Further discussion of the optimized constants can be found later in Chap. 7.1. For a number of experimental datasets, simulated annealing was unable to determine a suitable set of constants. In these experiments, strain softening beyond the minimum creep rate was minimal. As a consequence, the creep damage parameters could not properly be optimized by uSHARP. Instead, the values for the material constants were obtained manually until a suitable set of constants could be realized. Then the least squares formulation was applied to determine the quality of fit. Damage constants were optimized for every combination of temperature and stress.

CHAPTER FIVE: NOVEL ANISOTROPIC CREEP DAMAGE MODEL

5.1 Introduction

In order to produce an accurate multiaxial representation of the creep deformation of a transversely-isotropic material it is first necessary to accurately model the uniaxial x_1-x_2 plane of symmetry and x_3 normal represented by L and T specimen, respectively. Isotropic creep damage models are commonly implemented for simple cases involving uniaxially loaded isotropic materials. Anisotropic models can be developed for complex states of stress and anisotropic materials.

This chapter describes the development of a novel anisotropic creep damage model for transversely-isotropic materials implemented in a general-purpose finite element analysis (FEA) software. An advanced tensorial damage formulation is implemented which includes both material orientation relative to loading and the degree of damage anisotropy in the model. A variation of the Norton-power law for steady state (e.g. secondary) is implemented which includes the Hill's anisotropic analogy for equivalent stress [26]. The new model is found to regress to the Kachanov-Rabotnov isotropic tertiary creep damage model allowing the direct implementation of previously determined constants. Rupture time and damage prediction models are derived from the damage rate tensor. The theoretical model is implemented in a user-programmable feature (UPF) in the non-linear FEA software, ANSYS® [91].

5.2 Constitutive Model

This novel anisotropic creep damage model for transversely-isotropic materials is based on the isotropic Kachanov-Rabotnov creep damage model [5,6]. The influence of the state of damage, $\boldsymbol{\omega}$ is accounted for via the effective (net) stress tensor, $\tilde{\boldsymbol{\sigma}}$. A number of formulations for the effective stress have been proposed [34]. Murakami [50] and Murakami and Ohno [47] proposed the symmetric effective (net) stress, $\tilde{\boldsymbol{\sigma}}$ and damage applied, $\boldsymbol{\Omega}$ as

$$\begin{aligned} \boldsymbol{\Omega} &= (\mathbf{I} - \boldsymbol{\omega})^{-1} \\ \tilde{\boldsymbol{\sigma}} &= \frac{1}{2}(\boldsymbol{\sigma}\boldsymbol{\Omega} + \boldsymbol{\Omega}\boldsymbol{\sigma}) \end{aligned} \tag{5.1}$$

where $\boldsymbol{\sigma}$ is the Cauchy stress tensor and $\boldsymbol{\Omega}$ is damage applied.

For anisotropic materials, the orientation of the material grain structure relative to the general coordinates system can significantly alter the damage developed. Thus to account for material orientation the material damage constants need to be formulated into a tensor that alters each tensorial term based on a material orientation vector, $\mathbf{v}$ where the vector represents the direction of longitudinal grains. The rotated damage constant tensor, **B** is defined here as

$$\mathbf{B} = \left[M_2 \left(\sigma_{Hill}\right)^{\chi_2} \left(\mathbf{I} - \mathbf{v}\mathbf{v}^{\mathrm{T}}\right) + M_1 \left(\sigma_{Hill}\right)^{\chi_1} \left(\mathbf{v}\mathbf{v}^{\mathrm{T}}\right) \right] \tag{5.2}$$

where M_1, M_2, χ_1, χ_2 are damage constants and σ_{Hill} is the Hill equivalent stress [26] from the Cauchy stress defined as

$$\sigma_{Hill} = \sqrt{\mathbf{s}^T \mathbf{M} \mathbf{s}} \tag{5.3}$$

$$\mathbf{s} = VEC(\boldsymbol{\sigma})$$

$$\mathbf{M} = \begin{bmatrix} G+H & -H & -G & 0 & 0 & 0 \\ -H & F+H & -F & 0 & 0 & 0 \\ -G & -F & F+G & 0 & 0 & 0 \\ 0 & 0 & 0 & 2N & 0 & 0 \\ 0 & 0 & 0 & 0 & 2L & 0 \\ 0 & 0 & 0 & 0 & 0 & 2M \end{bmatrix}$$

where $\mathbf{s}$ is the vector form of the Cauchy stress tensor, $\boldsymbol{\sigma}$, and $\mathbf{M}$ is the Hill compliance tensor consisting of the F, G, H, L, M, and N unitless material constants that can be obtained from creep tests [27]. The derivations needed to determine the Hill constants are found in Appendix B. The rotated damage constant tensor, $\boldsymbol{\Phi}$ is defined as

$$\begin{aligned} \boldsymbol{\Phi}^R &= \left[\phi_2\left(\mathbf{I} - \mathbf{v}\mathbf{v}^{\mathrm{T}}\right) + \phi_1\left(\mathbf{v}\mathbf{v}^{\mathrm{T}}\right)\right] \\ \boldsymbol{\Phi} &= \mathrm{ABS}\left(\boldsymbol{\Phi}^R\right) \quad \text{or} \quad \Phi_{ij} = \left|\Phi_{ij}^R\right| \end{aligned} \tag{5.4}$$

where ϕ_1, and ϕ_2 are damage constants. The rotated damage constant tensor, $\boldsymbol{\Phi}$ is used as an element-wise exponent in later mathematics so it is necessary to ensure each element remains positive. The ABS function is introduced which represents an element-wise absolute value of the argument tensor. This is necessary to prevent possible inversion in later mathematics dependent on the selected isotropy plane. The rotated damage constant tensors allow the creep material properties to be directly related to the orientation of the material grain structure.

In the isotropic damage formulation Eq. (4.6), it is observed that previous scalar-valued damage is related by $(1-\omega)^{-\phi}$. An equivalent tensor form is produced by use of the

elementwise Schur (or Hadamard) power of the damage applied tensor, $\boldsymbol{\Omega}$ and the rotated damage constant tensor, $\boldsymbol{\Phi}$ as follows

$$\mathbf{D} = \overrightarrow{\boldsymbol{\Omega}^{\boldsymbol{\Phi}}} = \boldsymbol{\Omega}^{\circ(\boldsymbol{\Phi})}$$

$$\mathbf{D} = \begin{bmatrix} \Omega_{11}^{\Phi_{11}} & \Omega_{12}^{\Phi_{12}} & \Omega_{13}^{\Phi_{13}} \\ \Omega_{21}^{\Phi_{21}} & \Omega_{22}^{\Phi_{22}} & \Omega_{23}^{\Phi_{23}} \\ \Omega_{31}^{\Phi_{31}} & \Omega_{32}^{\Phi_{32}} & \Omega_{33}^{\Phi_{33}} \end{bmatrix} \tag{5.5}$$

where the convenient tensor, $\mathbf{D}$ is later implemented in the damage rate tensor [101,102]. To account for both aluminum and copper-like, the damage control variable, γ is introduced. This term is applied in the first principal stress influence tensor as follows

$$\mathbf{X} = \left[(1-\gamma)\mathbf{I} + \gamma \left(\mathbf{n}_1 \mathbf{n}_1^{\mathrm{T}} \right) \right]$$
$$0.0 \le \gamma \le 1.0 \tag{5.6}$$

where $\mathbf{n_1}$ represents the first principal stress direction vector. When γ = 0.0 isotropic damage is isotropically distributed while when γ = 1.0 damage induced anisotropy is allowed to occur.

To produce the damage rate tensor, $\dot{\boldsymbol{\omega}}$, a multiplicative superposition of the rotated damage constant tensor, $\mathbf{B}$ and the convenient tensor, $\mathbf{D}$ which both account for material orientation is performed. This is followed by a symmetric product with the first principal stress influence tensor, $\mathbf{X}$. The elementwise Schur (or Hadamard) product is used

$$\dot{\boldsymbol{\omega}} = \frac{1}{2}\left[(\mathbf{B} \circ \mathbf{D}) \cdot \mathbf{X} + \mathbf{X} \cdot (\mathbf{B} \circ \mathbf{D}) \right] \tag{5.7}$$

$$\mathbf{B} \circ \mathbf{D} = \begin{bmatrix} B_{11}D_{11} & B_{12}D_{12} & B_{13}D_{13} \\ B_{21}D_{21} & B_{22}D_{22} & B_{23}D_{23} \\ B_{31}D_{31} & B_{32}D_{32} & B_{33}D_{33} \end{bmatrix}$$

The **B** and **D** tensors are both rotations of the material orientation [101,102]. As discussed earlier undesirable terms develop in tensor **D**. The Schur product with **B** eliminates them. An analytical exercise of the damage rate tensor for various material and stress rotations is provided Appendix C. The damage rate tensor is coupled with the anisotropic creep strain rate equation defined as follows

$$\mathbf{e}^{cr} = A_{aniso}\tilde{\sigma}_{Hill}^{\ n_{aniso}} \frac{\mathbf{Ms}}{\sigma_{Hill}} \tag{5.8}$$

where A_{aniso}, n_{aniso} are secondary creep material constants found via creep tests, **M** is the Hill compliance tensor, **s** is the Cauchy stress vector, and $\tilde{\sigma}_{\text{Hill}}$ is the Hill equivalent (net) stress due to the effective stress tensor, $\tilde{\boldsymbol{\sigma}}$. To ease the implementation of the model into finite element code, the symmetric stress and strain tensors are converted back and forth to stress and strain vectors (e.g. $\tilde{\boldsymbol{\sigma}} \rightleftarrows \tilde{\mathbf{s}}$, $\boldsymbol{\varepsilon}^{cr} \rightleftarrows \mathbf{e}^{cr}$). Material rotation can be performed in the creep strain rate equation as follows

$$\mathbf{e}^{cr} = A_{aniso}\sqrt{\tilde{\mathbf{s}}^T\mathbf{TMT}^T\tilde{\mathbf{s}}}^{\,n_{aniso}} \frac{\mathbf{TMT}^T\mathbf{s}}{\sqrt{\mathbf{s}^T\mathbf{TMT}^T\mathbf{s}}} \tag{5.9}$$

where **T** represents a material orientation transformation tensor about the x_1 axis of the form

$$\mathbf{T}=\begin{bmatrix} 1 & 0 & 0 & 0 & 0 & 0 \\ 0 & \cos(\alpha)^2 & \sin(\alpha)^2 & 0 & 0 & \cos(\alpha)\sin(\alpha) \\ 0 & \sin(\alpha)^2 & \cos(\alpha)^2 & 0 & 0 & -\cos(\alpha)\sin(\alpha) \\ 0 & 0 & 0 & \cos(\alpha) & -\sin(\alpha) & 0 \\ 0 & 0 & 0 & \sin(\alpha) & \cos(\alpha) & 0 \\ 0 & -2\cos(\alpha)\sin(\alpha) & 2\cos(\alpha)\sin(\alpha) & 0 & 0 & \cos(\alpha)^2-\sin(\alpha)^2 \end{bmatrix} \quad (5.10)$$

5.3 Rupture Prediction Model

A prediction of the rupture time can be achieved using the damage evolution equation (5.7). First it is assumed that the material behaves isotropically (γ = 0.0). Induced anisotropy is disabled for the purpose of simplicity in integration. Assuming an isotropic behavior provides the most conservatism as well as a damage rate tensor along the diagonal of the following form

$$\dot{\boldsymbol{\omega}}(\gamma=0.0)=\begin{bmatrix} \dfrac{M_2\sigma_{Hill}^{\chi_2}}{(1-\omega_{11})^{|\phi_2|}} & 0 & 0 \\ 0 & \dfrac{M_2\sigma_{Hill}^{\chi_2}}{(1-\omega_{22})^{|\phi_2|}} & 0 \\ 0 & 0 & \dfrac{M_1\sigma_{Hill}^{\chi_1}}{(1-\omega_{33})^{|\phi_1|}} \end{bmatrix}$$

An examination of first principal influence tensor is provided

$$(\gamma=0.0) \qquad (\gamma=0.5) \qquad (\gamma=1.0)$$

$$\mathbf{n}_1 = \begin{pmatrix} 0 \\ 0 \\ 1 \end{pmatrix} \qquad \mathbf{X} = \begin{bmatrix} 1.0 & 0 & 0 \\ 0 & 1.0 & 0 \\ 0 & 0 & 1.0 \end{bmatrix} \qquad \mathbf{X} = \begin{bmatrix} 0.5 & 0 & 0 \\ 0 & 0.5 & 0 \\ 0 & 0 & 1.0 \end{bmatrix} \qquad \mathbf{X} = \begin{bmatrix} 0 & 0 & 0 \\ 0 & 0 & 0 \\ 0 & 0 & 1.0 \end{bmatrix}$$

$$\mathbf{n}_1 = \begin{pmatrix} 0 \\ 0 \\ 1 \end{pmatrix} \qquad \mathbf{X} = \begin{bmatrix} 1.0 & 0 & 0 \\ 0 & 1.0 & 0 \\ 0 & 0 & 1.0 \end{bmatrix} \qquad \mathbf{X} = \begin{bmatrix} 0.5 & 0 & 0 \\ 0 & 0.5 & 0 \\ 0 & 0 & 1.0 \end{bmatrix} \qquad \mathbf{X} = \begin{bmatrix} 0 & 0 & 0 \\ 0 & 0 & 0 \\ 0 & 0 & 1.0 \end{bmatrix}$$

where rotation of the principal stress is observed to create shear term when $\gamma \neq 0.0$. Thus $\gamma = 0.0$ provides a simple more workable damage rate tensor. Now it is assumed that the material experiences an arbitrary rotation about the x_1 axis at an angle α via the material orientation vector, $\mathbf{v}$. This produces a damage rate tensor of the following form

$$\dot{\boldsymbol{\omega}} = \frac{d\omega}{dt} = \begin{bmatrix} \dfrac{M_2 \sigma_{Hill}^{\chi_2}}{\left(1-\omega_{11}\right)^{|\phi_2|}} & 0 & 0 \\ 0 & \dfrac{M_1 \sigma_{Hill}^{\chi_1} \sin^2\alpha - M_2 \sigma_{Hill}^{\chi_2}\left(\sin^2\alpha - 1\right)}{\left(1-\omega_{22}\right)^{\left|\phi_1 \sin^2\alpha - \phi_2\left(\sin^2\alpha - 1\right)\right|}} & 0 \\ 0 & 0 & \dfrac{M_1 \sigma_{Hill}^{\chi_1} \cos^2\alpha - M_2 \sigma_{Hill}^{\chi_2}\left(\cos^2\alpha - 1\right)}{\left(1-\omega_{33}\right)^{\left|\phi_1 \cos^2\alpha - \phi_2\left(\cos^2\alpha - 1\right)\right|}} \end{bmatrix}$$

It is observed that each term of the damage rate tensor can be taken independently. Separation of variables provides

$$\int \left(1-\omega_{11}\right)^{|\phi_2|} d\omega = \int M_2 \sigma_{Hill}^{\chi_2} dt$$

$$\int \left(1-\omega_{22}\right)^{\left|\phi_1 \sin^2\alpha - \phi_2\left(\sin^2\alpha - 1\right)\right|} d\omega = \int M_1 \sigma_{Hill}^{\chi_1} \sin^2\alpha - M_2 \sigma_{Hill}^{\chi_2} \left(\sin^2\alpha - 1\right) dt$$

$$\int \left(1-\omega_{33}\right)^{\left|\phi_1 \cos^2\alpha - \phi_2\left(\cos^2\alpha - 1\right)\right|} d\omega = \int M_1 \sigma_{Hill}^{\chi_1} \cos^2\alpha - M_2 \sigma_{Hill}^{\chi_2} \left(\cos^2\alpha - 1\right) dt$$

where integration and further simplification leads to rupture time predictions as followings

$$t_{x1} = \left[1-\left(1-\omega_{11}\right)^{|\phi_2|+1}\right]\left[\left(|\phi_2|+1\right) M_2 \sigma_r^{\chi_2}\right]^{-1}$$

$$t_{x2} = \left[1-\left(1-\omega_{22}\right)^{\left|\phi_1 \sin^2\alpha - \phi_2\left(\sin^2\alpha - 1\right)\right|+1}\right]\left[\begin{array}{l}\left(\left|\phi_1 \sin^2\alpha - \phi_2\left(\sin^2\alpha - 1\right)\right|+1\right)\cdot \\ \left(M_1 \sigma_{Hill}^{\chi_1} \sin^2\alpha - M_2 \sigma_{Hill}^{\chi_2}\left(\sin^2\alpha - 1\right)\right)\end{array}\right]^{-1}$$

$$t_{x3} = \left[1-\left(1-\omega_{33}\right)^{\left|\phi_1 \cos^2\alpha - \phi_2\left(\cos^2\alpha - 1\right)\right|+1}\right]\left[\begin{array}{l}\left(\left|\phi_1 \cos^2\alpha - \phi_2\left(\cos^2\alpha - 1\right)\right|+1\right)\cdot \\ \left(M_1 \sigma_{Hill}^{\chi_1} \cos^2\alpha - M_2 \sigma_{Hill}^{\chi_2}\left(\cos^2\alpha - 1\right)\right)\end{array}\right]^{-1} \quad (5.11)$$

$$T = \begin{bmatrix} t_{x1} & 0 & 0 \\ 0 & t_{x2} & 0 \\ 0 & 0 & t_{x3} \end{bmatrix}$$

And rearrangement provides damage predictions

$$\omega_{x1}\left(t\right) = 1-\left[1-\left(|\phi_2|+1\right) M_2 \sigma_r^{\chi_2} t\right]^{\frac{1}{|\phi_2|+1}}$$

$$\omega_{x2}\left(t\right) = 1-\left[\begin{array}{l}1-\left(\left|\phi_1 \sin^2\alpha - \phi_2\left(\sin^2\alpha - 1\right)\right|+1\right)\cdot \\ \left(M_1 \sigma_{Hill}^{\chi_1} \sin^2\alpha - M_2 \sigma_{Hill}^{\chi_2}\left(\sin^2\alpha - 1\right)\right) t\end{array}\right]^{\frac{1}{\left|\phi_1 \sin^2\alpha - \phi_2\left(\sin^2\alpha - 1\right)\right|+1}} \quad (5.12)$$

$$\omega_{x3}(t) = 1 - \left[\begin{array}{l} 1 - \left(\left| \phi_1 \cos^2\alpha - \phi_2 \left(\cos^2\alpha - 1 \right) \right| + 1 \right) \cdot \\ \left(M_1 \sigma_{Hill}^{\chi_1} \cos^2\alpha - M_2 \sigma_{Hill}^{\chi_2} \left(\cos^2\alpha - 1 \right) \right) t \end{array} \right]^{\frac{1}{\left| \phi_1 \cos^2\alpha - \phi_2 \left(\cos^2\alpha - 1 \right) \right| + 1}}$$

$$\boldsymbol{\omega} = \begin{bmatrix} \omega_{x1} & 0 & 0 \\ 0 & \omega_{x2} & 0 \\ 0 & 0 & \omega_{x3} \end{bmatrix}$$

The influence of the first principal stress direction can be optionally be re-introduced as follows

$$t_f = \mathbf{n}_1^{\mathrm{T}} \mathbf{T} \mathbf{n}_1 = \begin{pmatrix} 0 & \sin\beta & \cos\beta \end{pmatrix} \begin{bmatrix} t_{x1} & 0 & 0 \\ 0 & t_{x2} & 0 \\ 0 & 0 & t_{x3} \end{bmatrix} \begin{pmatrix} 0 \\ \sin\beta \\ \cos\beta \end{pmatrix} = t_{x2} \sin^2\beta + t_{x3} \cos^2\beta$$

$$\omega_f = \mathbf{n}_1^{\mathrm{T}} \boldsymbol{\omega} \mathbf{n}_1 = \begin{pmatrix} 0 & \sin\beta & \cos\beta \end{pmatrix} \begin{bmatrix} \omega_{x1} & 0 & 0 \\ 0 & \omega_{x2} & 0 \\ 0 & 0 & \omega_{x3} \end{bmatrix} \begin{pmatrix} 0 \\ \sin\beta \\ \cos\beta \end{pmatrix} = \omega_{x2} \sin^2\beta + \omega_{x3} \cos^2\beta$$

such that a scalar-valued solution for rupture time and damage can be obtained under both material reorientation and stress rotation. However, it is suggested that the minimum value in the diagonal of the tensor be set as rupture time and critical damage. When adequate damage constants are determined, a quality prediction of rupture time can be achieved for L and T specimen. In the case of intermediate orientations, data is not available to quantify rupture time and damage prediction accuracy.

5.4 Numerical Approach

The novel anisotropic creep damage model for transversely-isotropic material is implemented into the finite element analysis (FEA) software ANSYS®. This is achieved by coding a usermat3d.f user-programmable feature (UPF) in FORTRAN. The usermat3d.f UPF allows coding of unique material constitutive equations within the ANSYS general material framework. For each Newton-Raphson iteration, at every material integration point, the USERMAT UPF is called. At the beginning time increment the state of stress, strain, and state variables are provided. An updated state of stress, state variables, and the material Jacobian matrix (total stiffness tensor) are required outputs [103]. In the current code the material Jacobian matrix is described as follows

$$\begin{gathered} \boldsymbol{\varepsilon}^{tot} = \mathbf{T}\mathbf{S}_{EL}\mathbf{T}^{\mathrm{T}} \cdot \boldsymbol{\sigma} + \mathbf{S}_{INEL} \cdot \boldsymbol{\sigma} \\ \mathbf{C}_{EL} = \left(\mathbf{S}_{EL}\right)^{-1} \quad \mathbf{C}_{INEL} = \left(\mathbf{S}_{INEL}\right)^{-1} \\ \mathbf{C}_{TOT} = \mathbf{C}_{EL} + \mathbf{C}_{INEL} \end{gathered} \tag{5.13}$$

where $\boldsymbol{\varepsilon}^{tot}$ is the total strain tensor, $\boldsymbol{\sigma}$ is the Cauchy stress tensor, $\mathbf{T}$ is a material orientation transformation tensor that coincides with the material orientation vector, $\boldsymbol{\nu}$, $\mathbf{S}_{\mathrm{EL}}$ and $\mathbf{S}_{\mathrm{INEL}}$ are the elastic and inelastic compliance tensors, $\mathbf{C}_{\mathrm{EL}}$ and $\mathbf{C}_{\mathrm{INEL}}$ are the elastic and inelastic stiffness tensors, and $\mathbf{C}_{\mathrm{TOT}}$ is the total stiffness tensor. In the case of transversely-isotropic materials the elastic compliance tensor, $\mathbf{S}_{\mathrm{EL}}$ is provided as

$$\mathbf{S}_{EL} = \begin{bmatrix} \frac{1}{E_p} & -\frac{\nu_p}{E_p} & -\frac{\nu_{zp}}{E_z} & 0 & 0 & 0 \\ -\frac{\nu_p}{E_p} & \frac{1}{E_p} & -\frac{\nu_{zp}}{E_z} & 0 & 0 & 0 \\ -\frac{\nu_{pz}}{E_p} & -\frac{\nu_{pz}}{E_p} & \frac{1}{E_z} & 0 & 0 & 0 \\ 0 & 0 & 0 & \frac{1}{2G_{zp}} & 0 & 0 \\ 0 & 0 & 0 & 0 & \frac{1}{2G_{zp}} & 0 \\ 0 & 0 & 0 & 0 & 0 & \left(\frac{1+\nu_p}{E_p}\right) \end{bmatrix} \tag{5.14}$$

where the Young's moduli, Poisson's ratios, and shear modulus are E_p, E_z, ν_p, ν_{zp}, ν_{pz}, and G_{zp} respectively. The inelastic compliance tensor is derived using the creep strain rate tensor Eq. (5.8) and Cauchy stress tensor, $\boldsymbol{\sigma}$ into the following symmetric form.

$$\mathbf{S}_{INEL} = \frac{d\boldsymbol{\varepsilon}^{cr}}{d\boldsymbol{\sigma}}$$

$$\mathbf{S}_{INEL} = \begin{bmatrix} S_{11} & S_{12} & S_{13} & S_{14} & S_{15} & S_{16} \\ & S_{22} & S_{23} & S_{24} & S_{25} & S_{26} \\ & & S_{33} & S_{34} & S_{35} & S_{36} \\ & & & S_{44} & S_{45} & S_{46} \\ & & & & S_{55} & S_{56} \\ SYM & & & & & S_{66} \end{bmatrix} \tag{5.15}$$

CHAPTER SIX: IMPROVED ANISOTROPIC CREEP DAMAGE MODEL

6.1 Introduction

The previously developed anisotropic creep damage formulations for transversely-isotropic assume state of stress induced anisotropy through an attached influence tensor. Damage evolution is based on material rotation where only the L and T material properties are utilized. This produces a less than ideal tensorial prediction of damage which does not account for possible strain hardening due to slip planes at arbitrary intermediate orientations nor does it implicitly include state of stress induced anisotropy.

This chapter describes the development of an improved anisotropic creep damage model for transversely-isotropic materials implemented in a general-purpose finite element analysis (FEA) software. An advanced tensorial damage formulation is implemented which implicitly includes the effect of material rotation and stress transformation using the Cauchy stress tensor and two Hill compliance tensors. A variation of the Norton-power law for steady state (e.g. secondary) is implemented which includes the Hill's anisotropic analogy for equivalent stress [26]. The new model is found to regress to the Kachanov-Rabotnov isotropic tertiary creep damage model allowing the direct implementation of previously determined constants. Rupture time and damage prediction models are derived from the damage rate tensor. The theoretical model is implemented in a user-programmable feature (UPF) in the non-linear FEA software, ANSYS® [91].

6.2 Continuum Damage Mechanics Theory

In the development of an improved constitutive model, it is necessary to first dissect the problem. To do so, a theoretical examination of fracture in transverse-isotropic materials and its application in continuum damage mechanics (CDM) is necessary. In typical CDM, the subject material is assumed to be homogenous. Grain boundaries are neglected. Local creep strain softening is accounted for via the damage variable which increases the net/effective stress thus equivalence is achieved between the physical and effective space.

In the case that creep test experimental data is available, the damage evolution and rupture time can be optimized using the isotropic Kachanov-Rabotnov creep damage formulation. As depicted in Figure 6.1, this creates material properties dependent on the materials orientation.

In terms of early creep crack propagation of transversely-isotropic materials rupture behavior is driven by the interaction of orthotropic and slip plane damage. Fracture occurs along planes of weakness; directions where the energy release rate is maximized. Material weakness is found between grain boundaries, a common location of crack propagation.

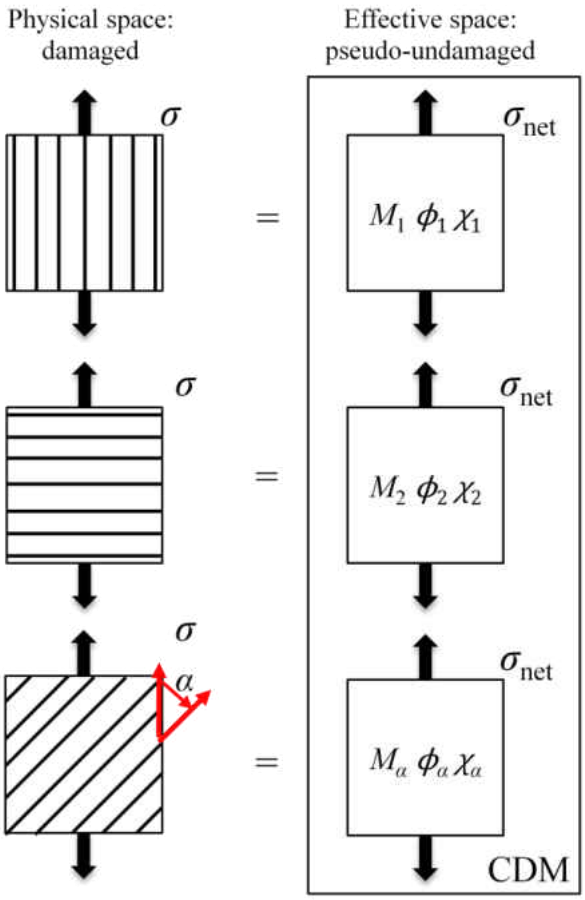

Figure 6.1 - Equivalence of Physical and Effective (CDM) space

An L-oriented specimen under tensile is shown in Figure 6.2a. Fracture occurs across the long grains in either a transgranular or intergranular fashion dependent on grain size relative to gage length. For the subject material, DS GTD-111, the gage length is smaller than the average grain size resulting in transgranular factor. However, in the case of intergranular fracture the crack path moves up and down grain boundaries until a suitable weakness (energy release rate maximized) is found in the adjacent grain resulting in mixed mode spitting between grain boundaries.

A T-oriented specimen under tensile is shown in Figure 6.2b. Fracture occurs along the available grain boundary until failure occurs. In transversely-isotropic materials this orientation of intergranular fracture is extensively studied due to the minimal amount of inelastic strain is found in this orientation before failure.

An arbitrary angled specimen under tensile is shown in Figure 6.3. The arbitrary angled specimen exhibits a mixed mode fracture. Early stage creep crack growth is dependent on the stress field and the damage parameters attributed to long and transverse orientations. Crack propagation can occur across the long grains when the energy release rate is maximized. The direction of crack growth is strongly driven by grain boundary orientation [112].

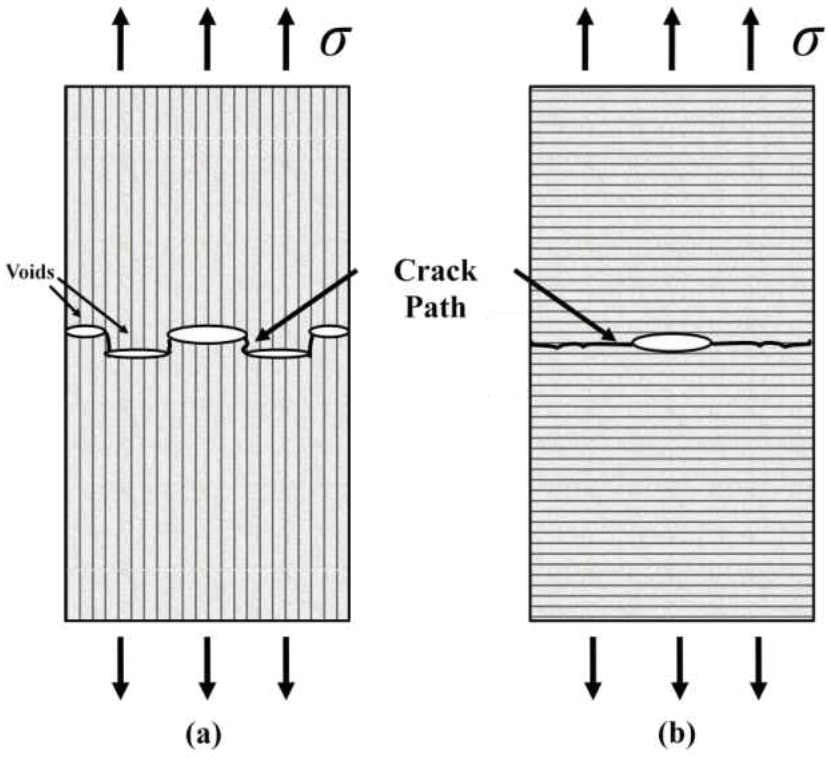

Figure 6.2 - Intergranular fracture of an (a) L and (b) T specimen

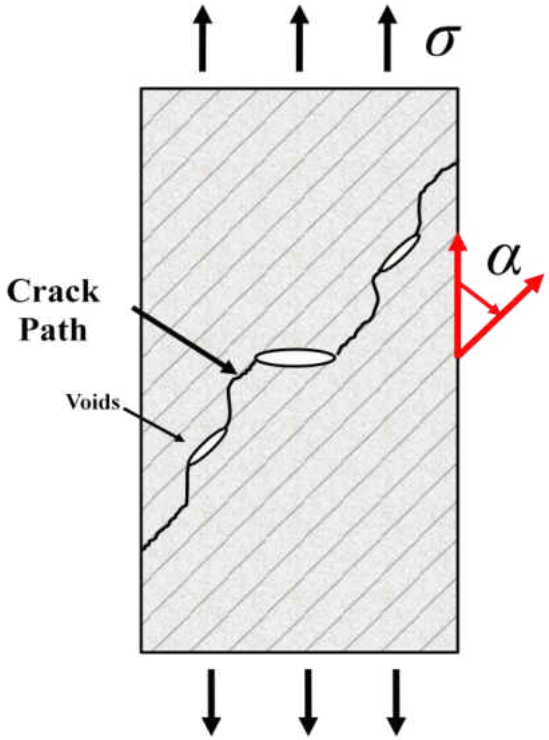

Figure 6.3 - Intergranular fracture of an arbitrary angled specimen

When considering continuum damage mechanics, grain boundary orientation must be considered. For transversely-isotropic materials, identical damage mechanisms exist on orthotropic directions but they evolve uniquely for each orientation (except on the plane of symmetry). Additionally, different damage mechanisms can exist on intermediate orientation where lattice mismatch induces slip plane damage.

Examining the developed novel anisotropic damage mechanics formulation, it is observed that the tertiary creep damage constants tensors Eqs. (5.2) and (5.4) account for dominant damage mechanism along L and T orientations; however, the model neglects possible

interaction between terms which would arise due to lattice mismatch acting on the slip plane. The slip induces strain hardening which increases the creep strain rate, and decreases time till rupture. Not accounting for this behavior leads to an inaccurate prediction of damage evolution and rupture time at intermediate orientations; therefore, an improved tensorial damage formulation is required to better prediction damage evolution, the creep strain rate, and rupture time.

6.3 Constitutive Model

The foundation of the improved anisotropic creep model is very similar to the previously developed novel anisotropic creep model. The improved model is based on the isotropic Kachanov-Rabotnov creep damage model [5,6]. The influence of the state of damage, $\boldsymbol{\omega}$ is accounted for via the effective (net) stress tensor, $\tilde{\boldsymbol{\sigma}}$. The Murakami and Ohno [47] symmetric effective (net) stress, $\tilde{\boldsymbol{\sigma}}$ and a simplified damage applied, $\boldsymbol{\Omega}$ are applied

$$\begin{aligned} \boldsymbol{\Omega} &= (\mathbf{I} - \boldsymbol{\omega})^{-1} \\ \tilde{\boldsymbol{\sigma}} &= \frac{1}{2}(\boldsymbol{\sigma}\boldsymbol{\Omega} + \boldsymbol{\Omega}\boldsymbol{\sigma}) \end{aligned} \tag{6.1}$$

where $\boldsymbol{\sigma}$ is the Cauchy stress tensor and $\boldsymbol{\Omega}$ is damage applied. Damage is represented by multiple principle damage variables due to induced anisotropy [45,46] in the form of a damage tensor

$$\omega = \begin{bmatrix} \omega_1 & 0 & 0 \\ 0 & \omega_2 & 0 \\ 0 & 0 & \omega_3 \end{bmatrix} \tag{6.2}$$

where each term of damage corresponds to the orthogonal planes of a material.

Creep damage anisotropy is introduced via two damage constant tensors. The tertiary creep damage constants are generalized into a vector (6x1) form using the anisotropic Hill potential theory transformed into damage constant tensors (3x3). The vectors take the following form

$$\begin{aligned} \mathbf{b}^R &= M_{aniso}\sigma_{Hillb}^{\chi_{aniso}} \frac{\mathbf{M}_b \mathbf{s}_p}{\sigma_{Hillb}} & \boldsymbol{\lambda}^R &= \phi_{aniso} \frac{\mathbf{M}_\lambda \mathbf{s}_p}{\sigma_{Hill\lambda}} \\ \mathbf{b} &= \mathrm{ABS}\left(\mathbf{b}^R\right) & \boldsymbol{\lambda} &= \mathrm{ABS}\left(\boldsymbol{\lambda}^R\right) \\ \mathbf{b} &= \mathrm{VEC}\left(\mathbf{B}\right) & \boldsymbol{\lambda} &= \mathrm{VEC}\left(\boldsymbol{\Phi}\right) \end{aligned} \tag{6.3}$$

where M_{aniso}, χ_{aniso}, and ϕ_{aniso} are tertiary creep damage constants and $\mathbf{s}_p$ is the vector form of the principal stress which can be found solving the following

$$\det\left[\boldsymbol{\sigma} - \sigma_n \mathbf{I}\right] = 0$$

$$\boldsymbol{\sigma}_p = \begin{bmatrix} \sigma_{n,1} & 0 & 0 \\ 0 & \sigma_{n,2} & 0 \\ 0 & 0 & \sigma_{n,3} \end{bmatrix} \tag{6.4}$$

$$\mathbf{s}_p = VEC\left(\boldsymbol{\sigma}_p\right)$$

where $\boldsymbol{\sigma}_p$ is a tensor of the principal stress where the subscripts (1,2,3) denote the orthogonal material plane on which each principal stress lies. For example, an imposed Cauchy stress of

$$\boldsymbol{\sigma} = \begin{bmatrix} 0 & 0 & 0 \\ 0 & 0 & \frac{\sigma_0\sqrt{3}}{3} \\ 0 & \frac{\sigma_0\sqrt{3}}{3} & 0 \end{bmatrix}$$

would resolve into the following principal stress tensor form

$$\boldsymbol{\sigma}_p = \begin{bmatrix} 0 & 0 & 0 \\ 0 & \frac{-\sigma_0\sqrt{3}}{3} & 0 \\ 0 & 0 & \frac{\sigma_0\sqrt{3}}{3} \end{bmatrix}$$

The stresses σ_{Hill}, σ_{Hillb}, and $\sigma_{Hill\lambda}$ are Hill equivalent stress defined as

$$\sigma_{Hill} = \sqrt{\mathbf{s}^T\mathbf{M}\mathbf{s}} \qquad \sigma_{Hillb} = \sqrt{\mathbf{s}_p{}^T\mathbf{M}_b\mathbf{s}_p} \qquad \sigma_{Hill\lambda} = \sqrt{\mathbf{s}_p{}^T\mathbf{M}_\lambda\mathbf{s}_p}$$

$$\mathbf{s} = VEC(\boldsymbol{\sigma})$$

$$\mathbf{M} = \begin{bmatrix} G+H & -H & -G & 0 & 0 & 0 \\ -H & F+H & -F & 0 & 0 & 0 \\ -G & -F & F+G & 0 & 0 & 0 \\ 0 & 0 & 0 & 2N & 0 & 0 \\ 0 & 0 & 0 & 0 & 2L & 0 \\ 0 & 0 & 0 & 0 & 0 & 2M \end{bmatrix} \tag{6.5}$$

where **s** is the vector form of the Cauchy stress tensor, $\boldsymbol{\sigma}$ and **M** is the Hill compliance tensor [26] consisting of the *F*, *G*, *H*, *L*, *M*, and *N* unitless material constants that can be obtained from creep tests [27]. The damage constant vectors, **b** (hr^{-1}) and $\boldsymbol{\lambda}$ (unitless), require a unique Hill compliance tensor, $\mathbf{M}_b$ and $\mathbf{M}_\lambda$, respectively. Each compliance tensor requires 6 unitless material constants that can be determined analytically. Using a generalized form of the derivation outlined in APPENDIX B, the material constants for the compliance tensors can easily be analytically determined and are based on the uniaxial tertiary creep constants, M_1, M_2, χ_1, $\chi_{2,}$ $\phi_{1,\text{ and }}$ ϕ_2. The strength of this new method is that induced anisotropy is implicitly stated through the direct use of the Cauchy stress vector and the Hill compliance tensor. The ABS function, which represents an element-wise absolute value of the argument vector, is introduced to enforce damage accumulation.

In the isotropic damage formulation Eq. (4.6), it is observed that previous scalar-valued damage is related by $(1-\omega)^{-\phi}$. An equivalent tensor form is produced by use of the elementwise Schur (or Hadamard) power of the damage applied tensor, $\boldsymbol{\Omega}$ and the rotated damage constant tensor, $\boldsymbol{\Phi}$ as follows

$$\mathbf{D} = \overrightarrow{\boldsymbol{\Omega}^{\boldsymbol{\Phi}}} = \boldsymbol{\Omega}^{\circ(\boldsymbol{\Phi})}$$

$$\mathbf{D} = \begin{bmatrix} \Omega_{11}^{\Phi_{11}} & \Omega_{12}^{\Phi_{12}} & \Omega_{13}^{\Phi_{13}} \\ \Omega_{21}^{\Phi_{21}} & \Omega_{22}^{\Phi_{22}} & \Omega_{23}^{\Phi_{23}} \\ \Omega_{31}^{\Phi_{31}} & \Omega_{32}^{\Phi_{32}} & \Omega_{33}^{\Phi_{33}} \end{bmatrix} \tag{6.6}$$

where the convenient tensor, **D** is later implemented in the damage rate tensor [101,102].

The damage rate tensor, $\dot{\boldsymbol{\omega}}$, is multiplicative superposition of the damage constant tensors, **B** and the convenient tensor, **D** using the elementwise Schur (or Hadamard) product as follows

$$\dot{\boldsymbol{\omega}} = \mathbf{B} \circ \mathbf{D}$$

$$\mathbf{B} \circ \mathbf{D} = \begin{bmatrix} B_{11}D_{11} & B_{12}D_{12} & B_{13}D_{13} \\ B_{21}D_{21} & B_{22}D_{22} & B_{23}D_{23} \\ B_{31}D_{31} & B_{32}D_{32} & B_{33}D_{33} \end{bmatrix} \tag{6.7}$$

The damage rate tensor is coupled with the anisotropic creep strain rate equation defined as follows

$$\mathbf{e}^{cr} = A_{aniso}\tilde{\sigma}_{Hill}^{\,n_{aniso}} \frac{\mathbf{Ms}}{\sigma_{Hill}} \tag{6.8}$$

where A_{aniso}, n_{aniso} are secondary creep material constants found via creep tests, **M** is the Hill compliance tensor, **s** is the Cauchy stress vector, and $\tilde{\sigma}_{\text{Hill}}$ is the Hill equivalent (net) stress due to the effective stress tensor, $\tilde{\boldsymbol{\sigma}}$. To ease the implementation of the model into finite element code, the symmetric stress and strain tensors are converted back and forth to stress and strain vectors (e.g. $\tilde{\boldsymbol{\sigma}} \rightleftarrows \tilde{\mathbf{s}}$, $\boldsymbol{\varepsilon}^{cr} \rightleftarrows \mathbf{e}^{cr}$). Material rotation can be performed in the damage rate tensor as follows

$$\mathbf{b}^R = M_{aniso}\sqrt{\mathbf{s}_p{}^T\mathbf{TMT}^T\mathbf{s}_p}\,\chi_{aniso}\,\frac{\mathbf{TM}_b\mathbf{T}^T\mathbf{s}_p}{\sqrt{\mathbf{s}_p{}^T\mathbf{TM}_b\mathbf{T}^T\mathbf{s}_p}}$$

$$\boldsymbol{\lambda}^R = \phi_{aniso}\,\frac{\mathbf{TM}_\lambda\mathbf{T}^T\mathbf{s}_p}{\sqrt{\mathbf{s}_p{}^T\mathbf{TM}_\lambda\mathbf{T}^T\mathbf{s}_p}} \tag{6.9}$$

and in the creep strain rate equation as follows

$$\mathbf{e}^{cr} = A_{aniso}\sqrt{\tilde{\mathbf{s}}^T\mathbf{TMT}^T\tilde{\mathbf{s}}}^{n_{aniso}}\frac{\mathbf{TMT}^T\mathbf{s}}{\sqrt{\mathbf{s}^T\mathbf{TMT}^T\mathbf{s}}} \tag{6.10}$$

where **T** represents a material orientation transformation tensor about the x_1 axis of the form

$$\mathbf{T} = \begin{bmatrix} 1 & 0 & 0 & 0 & 0 & 0 \\ 0 & \cos(\alpha)^2 & \sin(\alpha)^2 & 0 & 0 & \cos(\alpha)\sin(\alpha) \\ 0 & \sin(\alpha)^2 & \cos(\alpha)^2 & 0 & 0 & -\cos(\alpha)\sin(\alpha) \\ 0 & 0 & 0 & \cos(\alpha) & -\sin(\alpha) & 0 \\ 0 & 0 & 0 & \sin(\alpha) & \cos(\alpha) & 0 \\ 0 & -2\cos(\alpha)\sin(\alpha) & 2\cos(\alpha)\sin(\alpha) & 0 & 0 & \cos(\alpha)^2 - \sin(\alpha)^2 \end{bmatrix} \tag{6.11}$$

The strengths of the improved model is that induced anisotropy is directly included. Changing the state of stress directly modifies the damage rate through the Hill compliance tensors. Damage evolution is thus dependent on the direction of principal loading. The use of Hill compliance tensors provide a great method by which both the secondary and tertiary creep behavior of the material can be modeled under material reorientation.

To apply this model a fair number of constants are necessary. Six secondary creep constants need to be analytically determine and can be easily found via uniaxial creep tests (A_L, A_T, A_{45}, n_L, n_T, and n_{45}). The method is discussed in Section 3.6. Using the ISO formulation and an iterative optimization scheme, nine tertiary creep constants need to be numerically determined (M_1, M_2, M_{45}, χ_1, $\chi_{2,}$ χ_{45}, ϕ_1, ϕ_2, and ϕ_{45}). For the subject material, these constants were obtained using the uSHARP automated optimization software and is discussed in Section 4.5. Lastly, three sets of six Hill constants need to be analytically determined for the **M**, $\mathbf{M}_b$, and $\mathbf{M}_\lambda$ Hill

compliance tensors. The analytical solutions for these sets of constants are found in APPENDIX B.

6.4 Rupture Prediction Model

The improved anisotropic creep damage formulation greatly simplifies prediction of rupture time and critical damage for transversely-isotropic materials. Symbolic expansion of the damage rate tensor Eq. (6.7), provides the following

$$\dot{\boldsymbol{\omega}} = \begin{bmatrix} \dfrac{b_1}{(1-\omega_{11})^{\lambda_1}} & 0 & 0 \\ 0 & \dfrac{b_2}{(1-\omega_{22})^{\lambda_2}} & 0 \\ 0 & 0 & \dfrac{b_3}{(1-\omega_{33})^{\lambda_3}} \end{bmatrix}$$

where b_i (hr^{-1}) and λ_i are expressed in Eq. (6.3). The apriori disappears of shear damage rate due to the use of principal stresses occurs. Assuming that each term of damage is independent, component wise derivation provides

$$t_i = \left[1-\left(1-\omega_i\right)^{\lambda_i+1}\right]\left[\left(\lambda_i+1\right)b_i\right]^{-1}$$

$$t_r = min\left\{t_i\right\} \tag{6.12}$$

$$\omega_i\left(t\right) = 1-\left[1-\left(\lambda_i+1\right)b_i t\right]^{\frac{1}{\lambda_i+1}}$$

$$i = 1,2,3$$

where full vector predictions are produced. Rupture time, t_r, can be considered equal to the minimal component found in the **t** vector. Additionally, rupture time could be determined using some effective approach but this is left for future study. Critical damage is assumed to be equal to that found in the **ω** component where rupture is expected to occur. Additionally, the final direction of rupture can be estimated based on the critical damage tensor.

The strength of the improved anisotropic model is that it provides the ability to predict rupture time and/or critical damage for any state of stress or material orientation.

6.5 Numerical Approach

The improved anisotropic creep damage model for transversely-isotropic materials is implemented into the finite element analysis (FEA) software ANSYS® identical to the previous model outlined in Section 5.4.

CHAPTER SEVEN: RESULTS

7.1 Introduction

This chapter presents and discusses the finite element and analytical results produced by using the isotropic and novel anisotropic creep damage deformation and life prediction formulations. The tertiary creep damage constants optimized using the isotropic creep damage formulation are listed. Using the optimized tertiary creep damage constants, the isotropic creep damage FE solutions are compared to available creep test experimental data. The tertiary creep damage constants are then characterized for temperature-dependence. Next, the method employed to determine the secondary, tertiary creep damage, and Hill constants required for the novel anisotropic novel anisotropic creep damage formulation is outlined. The secondary creep behavior of the novel formulation is analytically verified using the known minimum creep strain rates for L, T, and 45°-oriented specimen. An examination of damage evolution is performed. The novel formulation is shown to produce an accurate creep strain tensor for transversely-isotropic materials. Finally, the two previously discussed life prediction models are compared to rupture times from experiments. Finite element, analytical, and MacLachlan-Knowles damage estimates are used to determined life and compared.

7.2 Isotropic Model

Optimization of the Kachanov-Rabotnov isotropic creep damage formulation to the creep test experimental data has been used to determine the tertiary creep damage constants, M, χ, and ϕ as mentioned in Chapter 4. A list of these optimized constants is presented in Table 7.1. For each of the available creep tests, the final optimized finite element solution has been superimposed with creep deformation data, as shown in Figure 7.1. It should be noted that primary creep approximations where added directly to the collected FEM deformation data to account for the primary creep regime. It is observed that for all 16 creep tests, high-caliber fits to the creep deformation data was achieved. The isotropic creep damage model is found to accurately model the creep deformation as measured from a uniaxial specimen.

The behavior of the tertiary creep damage constants with respect to temperature is very important. Temperature-dependent functions of the tertiary creep damage constants for both L and T orientations of DS GTD-111, would allow accurate modeling of creep strain that develops in directionally-solidified components under a thermal gradient. Taking the results of the optimization routine, an automated curving-fitting tool was used to determine suitable functions for the damage evolution constants. The tertiary creep damage coefficient, M, was found to work well in an exponential equation of the form

$$M(T) = \lambda_1 M_1 \, exp(\lambda_2 M_0 T)$$

$$\begin{pmatrix} \mathbf{L} \\ \mathbf{T} \end{pmatrix} orientation = \begin{cases} \lambda_1 = \lambda_2 = 1 \\ \lambda_1 = 1.2128, \lambda_2 = .93265 \end{cases} \tag{7.1}$$

Table 7.1– Tertiary creep damage constants for DS GTD-111

Matl. Orient.	Temperature		Stress		Tertiary creep damage constants			Functional fit, f(T)					
α	(°C)	(°F)	(MPa)	(ksi)	M $(MPa^{-\chi}hr^{-1})$	χ	ϕ	M $(MPa^{-\chi}hr^{-1})$	χ	ϕ	Relative Error	Relative Error	Relative Error
L (0°)	649	1200	896	130	10.000	1.880	55.000	6.009	2.129	55.093	66.42%	-11.70%	-0.17%
L (0°)	760	1400	408	60	20.847	1.900	8.500	28.556	2.129	10.342	-27.00%	-10.76%	-17.81%
L (0°)	760	1400	613	89	19.784	2.231	13.261	28.556	2.129	10.342	-30.72%	4.80%	28.22%
T (90°)	760	1400	517	75	36.161	2.106	14.810	50.881	2.099	29.210	-28.93%	0.30%	-49.30%
T (90°)	760	1400	613	89	51.801	2.203	39.931	50.881	2.099	29.210	1.81%	4.93%	36.70%
L (0°)	816	1500	455	66	64.127	2.257	3.792	62.686	2.129	6.249	2.30%	5.99%	-39.32%
T (90°)	816	1500	455	66	167.590	1.981	28.224	118.221	2.099	17.444	41.76%	-5.64%	61.80%
L (0°)	871	1600	241	35	96.015	2.022	7.161	135.691	2.129	7.351	-29.24%	-5.06%	-2.58%
L (0°)	871	1600	289	42	131.010	2.054	9.698	135.691	2.129	7.351	-3.45%	-3.53%	31.93%
T (90°)	871	1600	241	35	263.010	2.098	2.296	270.579	2.099	9.446	-2.80%	-0.05%	-75.70%
T (90°)	871	1600	289	42	345.840	1.919	6.823	270.579	2.099	9.446	27.81%	-8.61%	-27.77%
L (0°)	940	1724	244	35	579.120	2.310	7.069	357.522	2.129	8.018	61.98%	8.51%	-11.84%
T (90°)	940	1724	244	35	600.000	2.290	7.069	764.588	2.099	4.396	-21.53%	9.07%	60.81%
L (0°)	982	1800	124	18	655.930	2.221	3.278	644.780	2.129	4.070	1.73%	4.30%	-19.46%
L (0°)	982	1800	145	21	665.200	2.288	5.126	644.780	2.129	4.070	3.17%	7.45%	25.95%
45°*	871	1600	289	42	53.296	2.156	20.933	---	---	---	---	---	---

*[84]

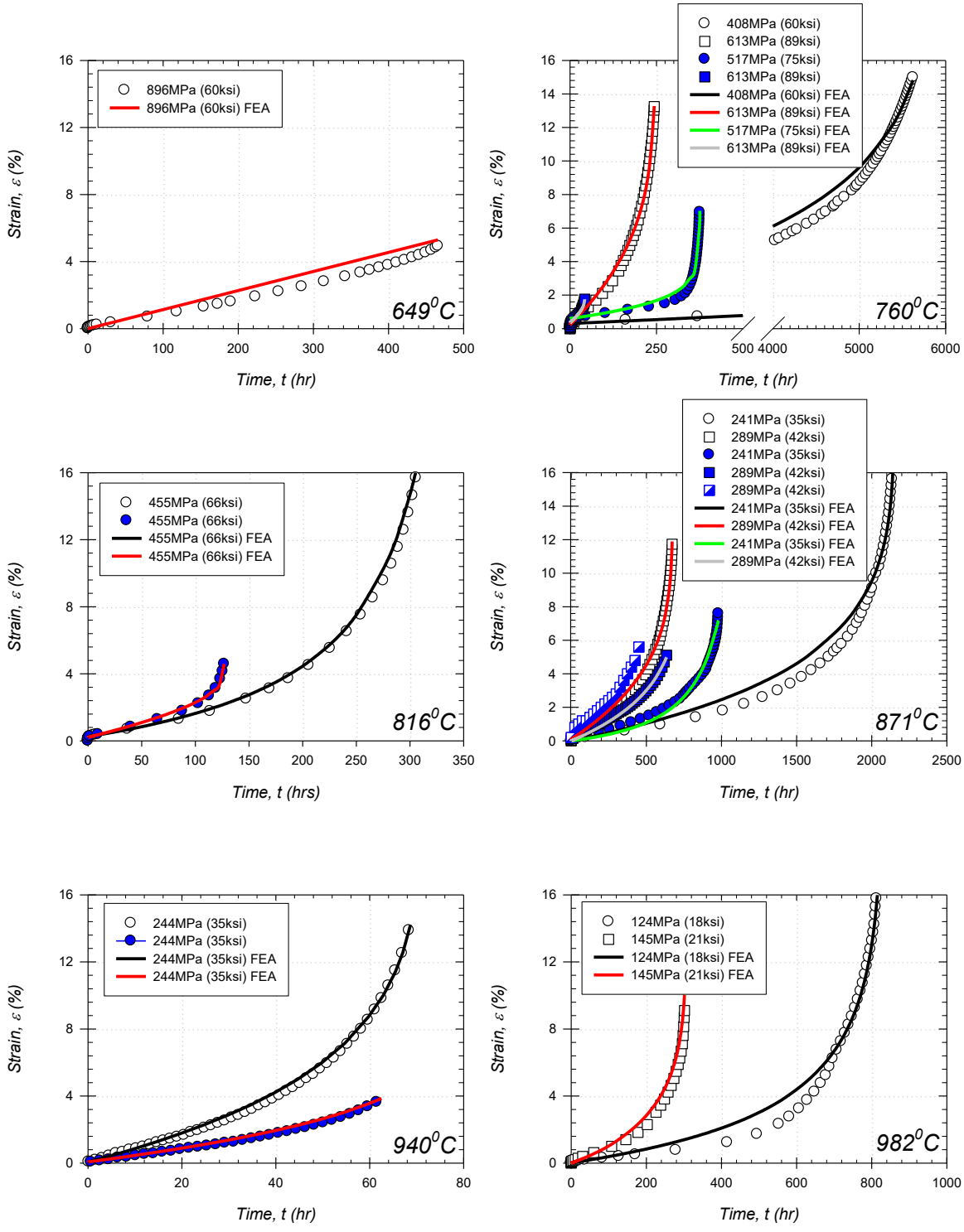

Figure 7.1 - Creep deformation fits of L (open), T (filled), and 45°-oriented (half-filled) DS GTD-111 at temperatures from 649-982°C using the isotropic Kachanov-Rabotnov formulation

where T is in unit Celsius and M_1 ($MPa^{-\chi}hr^{-1}$) and M_0 (unitless) are constants. The unitless weight values λ_1 and $\lambda_{2,}$ were used to implement the formulation for both L and T orientations. Ideally, the creep constants would be expressed in terms of tensile data (e.g yield strength, UTS, etc); however, that is saved for future study. Figure 7.2 shows the regression fit of the temperature-dependent function to the optimized constants. The temperature-dependent functions for the tertiary creep damage coefficient, M, carry an R^2 value of 0.9593 and 0.9409 for L and T-oriented specimen, respectively.

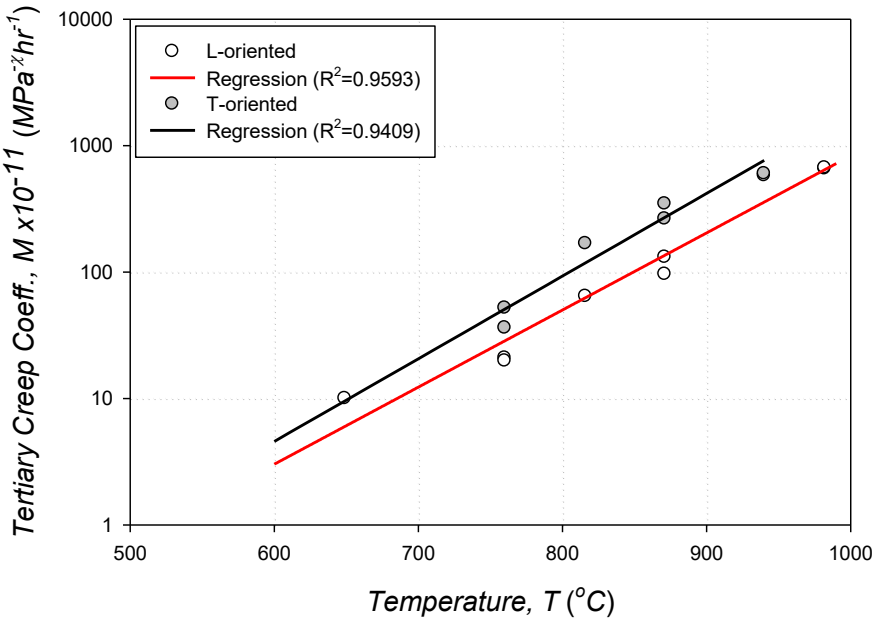

Figure 7.2 – Temperature-dependence of the M tertiary creep damage constants for DS GTD-111

The tertiary creep damage exponent, χ (unitless), was found to exhibit no perceivable temperature-dependence. The average value for L and T was observed as 2.1292 ± 0.2160 and 2.0994 ± 0.2834, respectively. Small changes in the χ tertiary creep damage exponent have a strong effect on the damage rate and consequently the M and ϕ tertiary creep damage constants. The placement of the tertiary creep damage exponent, χ as a power of stress, σ, sets the χ constant as a stress sensitivity factor. The fluctuations in the χ tertiary creep damage constants found in the optimized fits (Table 7.1) have a detrimental effect on the caliber of the temperature-dependent regression fits for the M and ϕ tertiary creep damage constants.

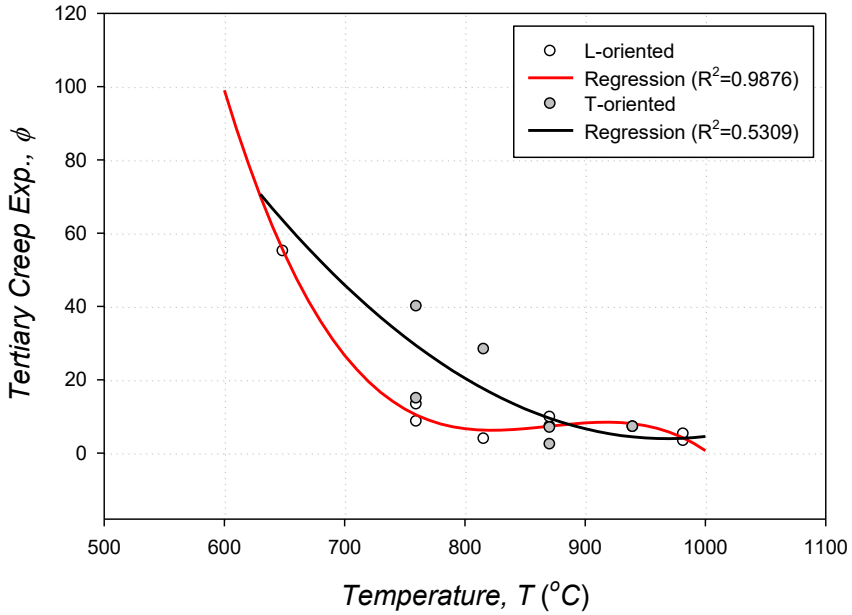

Figure 7.3 – Temperature-dependence of the ϕ tertiary creep damage constants for DS GTD-111

Again, ideally, the temperature-dependence of creep constants would be expressed in terms of tensile data but this is saved for future study. In the current study, the tertiary creep damage exponent, ϕ, was found to produce a less than ideal fit to temperature in a polynomial equation of the form

$$\phi(\sigma) = \phi_3 T^3 + \phi_2 T^2 + \phi_1 T + \phi_0 \tag{7.2}$$

where T is in units Celcius, and ϕ_0, ϕ_1, ϕ_2, and ϕ_3 are constants (independent sets for both L and T). Figure 7.3 shows the regression fit of the temperature-dependent function to the optimized constants. The temperature-dependent functions for the tertiary creep damage constants, ϕ, carry an R^2 value of 0.9876 and 0.5309 for L and T-oriented specimen, respectively. The low R^2 value in the T-oriented specimen data is likely due to the fluctuations observed in the χ tertiary creep damage constants. These slight fluctuations necessitate an observable shift in the ϕ tertiary creep damage constants to produce an accurate damage rate. This issue could be eliminated by conducting another batch optimization where the χ tertiary creep damage constants is negated as a possible temperature-dependent variable. Setting the χ tertiary creep damage constants as the known average from the initial optimization, could improve the modeling of temperature-dependence of the tertiary creep damage constants. Additionally, the weak dependence could be a symptom of the lower number of experimental tests available for the T orientation and/or microstructural inconsistency due to the use of three different material batches. In general, the R^2 achieved could be improved by conducting additional experiments in the L and T orientations and removing outlier data points.

The formulation could be modified by relating the tertiary creep damage constants as a function of temperature-dependent material properties. This could be done with quantitative analysis of the correlation between elastic and plastic material properties with the M and ϕ constants.

The implication of using these temperature-dependent functions is that it allows model structures whose boundary conditions include thermal gradients. Regions at elevated temperature will undergo a higher level of creep deformation compared to those at lower temperature. Using these functions leads to simulations that more accurately predict the locally critical points. Along similar lines, creep deformation during thermal cycling can be considered.

7.3 Anisotropic Model

Previous optimization using the isotropic Kachanov-Rabotnov formulation produced tertiary creep damage constants which can be directly applied in the novel anisotropic creep damage formulation. The anisotropic creep damage formulation requires uniaxial creep test experimental data for L, T, and 45°-oriented specimen in order to work correctly. This is due to the use of Hill's analogy as both a compliance tensor and equivalent stress in the creep strain rate Eq. (5.9). To determine the Hill constants, the creep strain rate, Eq. (5.9), is taken with the damage rate, Eq. (5.7), disabled via M_1=0.0 and M_2=0.0. Various stress transformations and material orientation transformations (about the x_1 normal) are performed. The Hill constants are found to be dependent on the uniaxial Norton power law for L, T, and 45°-oriented specimen.

Subsequently, the Hill constants can be referred back to the minimum strain rates found for L, T, and 45°-oriented specimen. The derivation of the Hill constants with an extended discussion can be found in Appendix B. For this study, L, T, and 45°-oriented specimen creep tests were conducted at a temperature of 871°C and 289 MPa uniaxial load. The secondary and tertiary creep, and derived Hill constants for DS GTD-111 required by the novel anisotropic creep damage formulation under these conditions are found in Table 7.2.

Table 7.2 - Secondary, Hill, and tertiary creep damage constants for DS GTD-111 at 871°C

$A_{aniso}(MPa^{-n_{aniso}}hr^{-1})$	n_{aniso}
5.7639×10^{-21}	6.5068

F	G	H	L	M	N
0.5	0.5	0.3866	1.6413	1.6413	1.2731

$M_1(MPa^{-\chi}hr^{-1})$	$M_2(MPa^{-\chi}hr^{-1})$	χ_1	χ_2	ϕ_1	ϕ_2
131.01×10^{-11}	345.84×10^{-11}	2.054	1.9186	9.698	6.8226

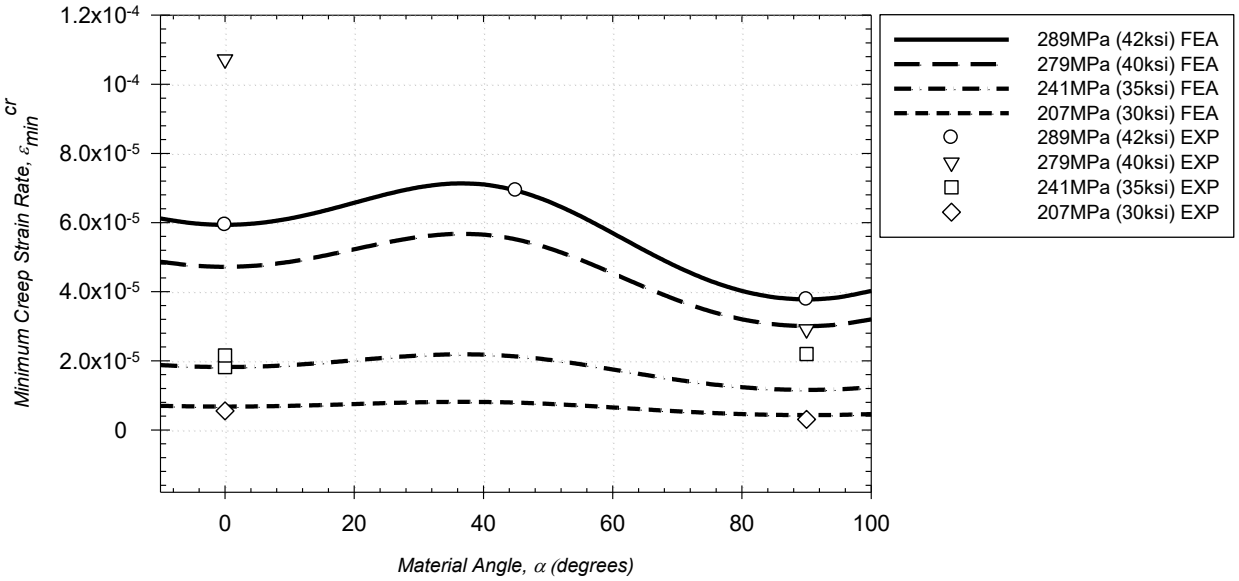

Figure 7.4 - Material orientation study of x_3 normal minimum creep strain rate at 871°C for various DS Ni-based materials

Verification of the secondary creep behavior can be achieved using the creep strain rate, Eq. (5.9), with the damage rate, Eq. (5.7), disabled. In general, the secondary creep response of the material is controlled by the A_{aniso}, n_{aniso} and Hill constants F, G, H, L, M, and N. Disabling damage (M_1=M_2=0.0) leads to the minimum creep strain rates found in Figure 7.4. The observed curve follows the trend expected of a Hill potential based model compared to other DS Ni-based superalloys [106-109]. The FEM prediction of minimum creep strain rates pass through the known rates for L, T, and 45°-oriented specimen at 289MPa. The material behavior observed in the 279 MPa experiment at α=0.0° is inconsistent with the study response. Pre-existing flaws in the specimen account for the observed high minimum creep strain rate.

Accurate estimates of damage evolution lead to high quality fits of the creep deformation data. For these purposes, the damage rate Eq. (5.7) is enabled. Simulations of L, T, and 45°-

oriented specimen are executed and compared with those developed using the isotropic creep damage formulation. Figure 7.5 shows that the novel anisotropic formulation produces similar damage evolution to the isotropic Kachanov-Rabotnov damage evolution for L and T-oriented specimen; however, the behavior of the 45°-oriented specimen is not accurately modeled. This disconnect is expected. Not directly including the tertiary creep damage constants associated with the 45°-oriented specimen will naturally lead to a less than ideal estimation of damage evolution when compared to the isotropic creep damage model. The damage behavior embedded in the novel anisotropic model considers a linear relationship between the L and T-oriented specimen based on material orientation transformation; however, the behavior of DS GTD-111 exhibits a maximized creep strain rate at an orientation between 35°-45°. While, the predicted damage evolution is not necessarily the same, it is found through examination of the available creep tests data that only slight tertiary creep behavior is found at 45° allowing for a good prediction of the creep strain rate at this orientation.

With the aid of available the creep test data, the creep strain versus time from experimental data is compared with both isotropic and novel anisotropic creep damage formulations. Figure 7.6 shows the novel anisotropic formulation performs very well in modeling the creep test experimental data. The accurate prediction of creep strain for a 45°-oriented specimen demonstrates that despite a damage evolution that diverges from the isotropic solution, the novel anisotropic creep damage formulation can accurately predict the creep deformation that develops in transversely-isotropic materials under arbitrary material orientations. Thus the relationship between creep behavior, material orientation, and state of stress are taken into account.

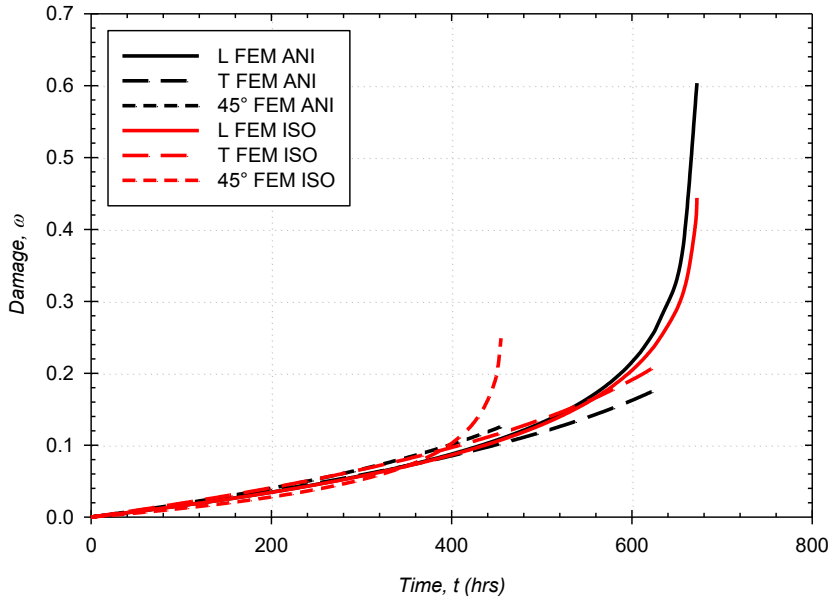

Figure 7.5 – Damage evolution on the x_3 normal of the isotropic and novel anisotropic creep damage formulations under 289MPa uniaxial load and 871°C

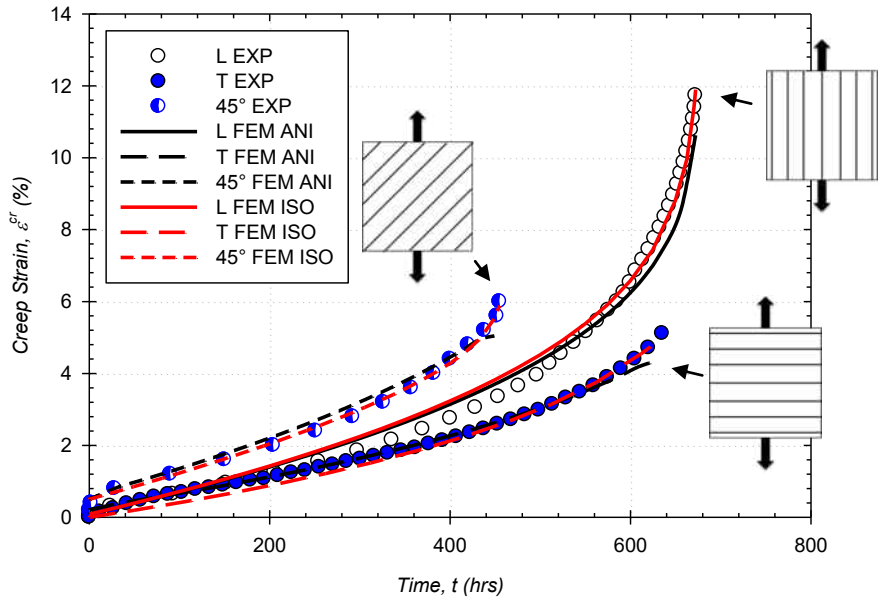

Figure 7.6 - Creep deformation on the x_3 normal of novel anisotropic and isotropic creep damage formulations compared with creep test data for DS GTD-111 under 289MPa uniaxial load and 871°C

The tensor creep strain behavior of the novel anisotropic creep damage model is of high importance. An accurate creep strain tensor for the subject material proves considerably improved estimations of creep deformation for directionally solidified components compared to the isotropic creep damage formulation.

Assuming $\gamma = 0.0$, the creep strain tensor response of L, T, and 45°-oriented specimens are presented in Figure 7.7. In the case of an L specimen (Figure 7.7a), the creep strains found on the x_2 and x_3 normals are equivalent. This is suitable as it shows that isotropy is found on the x_1-x_2 plane as expected of an L specimen. In the case of a T specimen (Figure 7.7b), the creep strain on the x_2 normal is higher than what develops on the x_3 normal. This is suitable because isotropic behavior is now found on the x_1-x_3 plane. The L grains produce a higher creep strain rate thus the x_2 normal is higher than the x_3 normal. In the case of a 45°-oriented specimen (Figure 7.7c), the creep behavior on the x_2 normal and x_3 normal is the same, however; due to uniaxial loading the creep strain that develops in the x_2 normal is compressive due to the deviatoric response.

In the case of the isotropic creep damage formulation, most FEM codes generalize a full strain tensor via isotropic material properties [110]. In the case of a transversely-isotropic material this would not produce an accurate result. Thus the novel anisotropic model is found to produce a more accurate strain tensor.

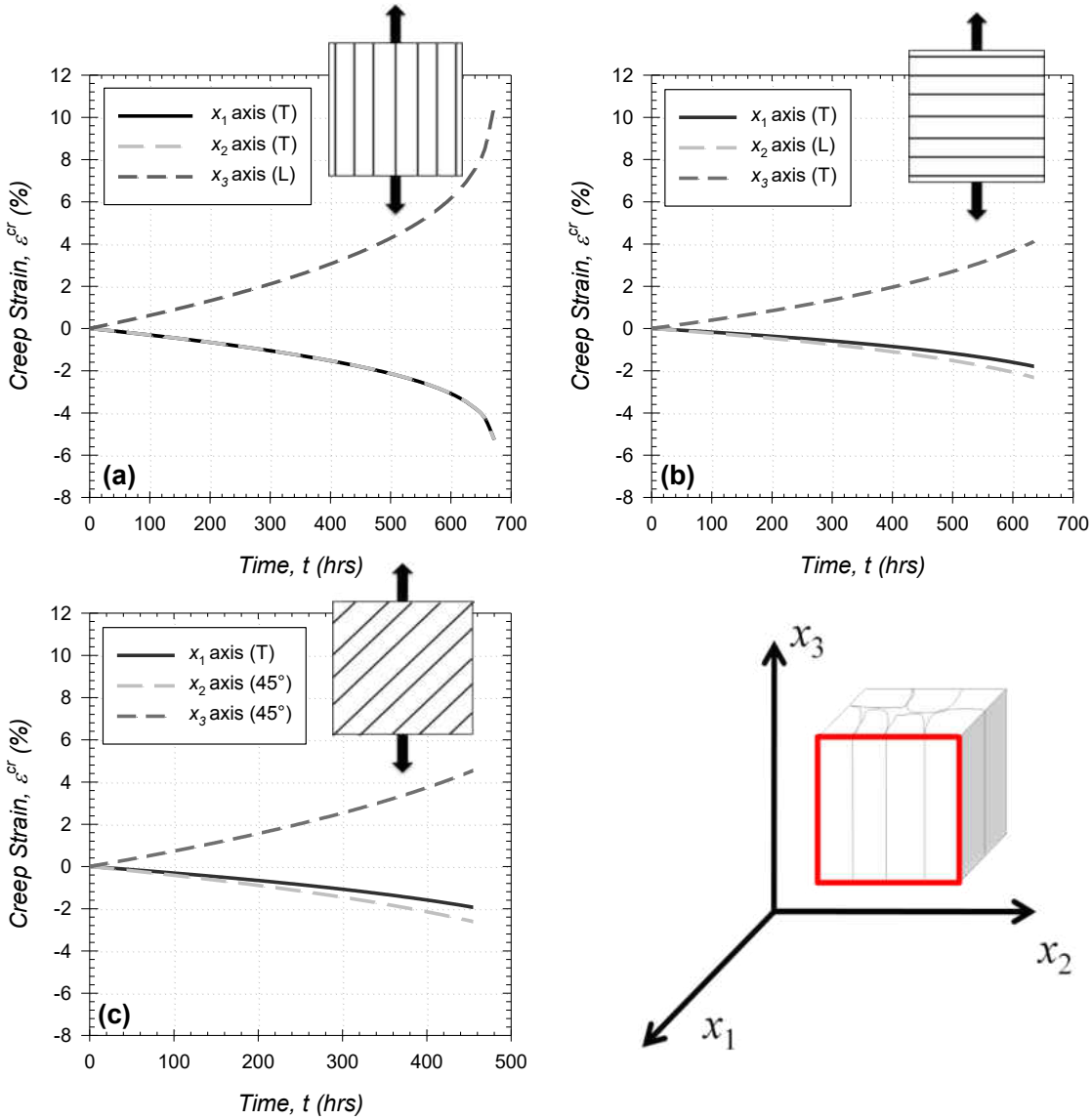

Figure 7.7 – Components of the creep deformation using the novel anisotropic creep damage formulation for (a) L, (b) T, and (c) 45°-oriented specimen under 289MPa uniaxial load and 871°C (note: primary creep is neglected)

7.4 Improved Anisotropic Model

The novel anisotropic model produced improved results over the isotropic model; however, the damage evolution in intermediate orientations is not accurate. This inaccuracy in damage evolution will later be shown to lead to inaccurate rupture time predictions. Therefore, it is necessary to develop an improved anisotropic creep damage formulation.

For the improved anisotropic formulation, the creep strain rate, Eq. (6.10), is exactly the same one used in the novel anisotropic formulation, Eq. (5.9). This leads to the secondary creep behavior (when disabled via M_1=0.0 and M_2=0.0) being identical to that previously found in Figure 7.4. The same secondary and tertiary creep, and derived Hill constants for DS GTD-111 are required and listed in Table 7.2l; however, additional constants associated with the 45°-oriented specimen are necessary, $M_{45} = 53.296\text{x}10^{-11}\ MPa^{-\chi}hr^{-1}$, $\chi_{45} = 2.1563$,and ϕ_{45}=20.933 at 289MPa and 871°C. Three versions of Hill's compliance tensor are developed, one for secondary creep, **M**, and two that account for the damage behavior, $\mathbf{M}_b$ and $\mathbf{M}_\lambda$, respectively. All three require a unique set of Hill constants. The derivation to find the Hill constants is found in APPENDIX B. For $\mathbf{M}_b$ and $\mathbf{M}_\lambda$, the following modification is necessary in the derivation.

$$\begin{array}{ll} \mathbf{M}_b & \mathbf{M}_\lambda \\ t_1 = \left(\dfrac{M_2 \sigma^{\chi_2}}{M_1 \sigma^{\chi_1}} \right)^{2/(\chi_{aniso}+1)} & t_1 = \left(\dfrac{\phi_2}{\phi_1} \right)^2 \\ t_2 = \left(\dfrac{M_{45^\circ} \sigma^{\chi_{45^\circ}}}{M_1 \sigma^{\chi_1}} \right)^{2/(n_{aniso}+1)} & t_2 = \left(\dfrac{\phi_{45^\circ}}{\phi_1} \right)^2 \end{array} \tag{7.3}$$

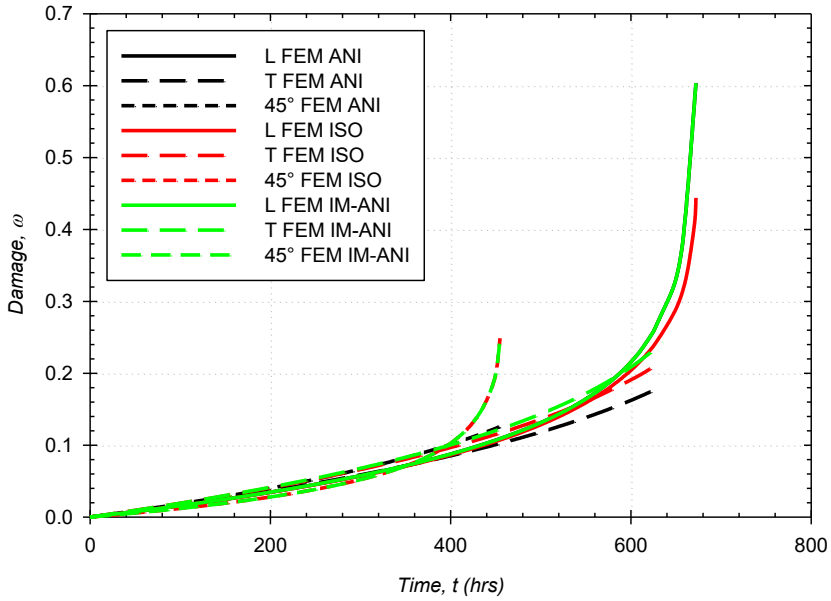

Figure 7.8 - Damage evolution on the x_3 normal of the ISO, ANI, and IM-ANI formulations under 289MPa uniaxial load and 871°C

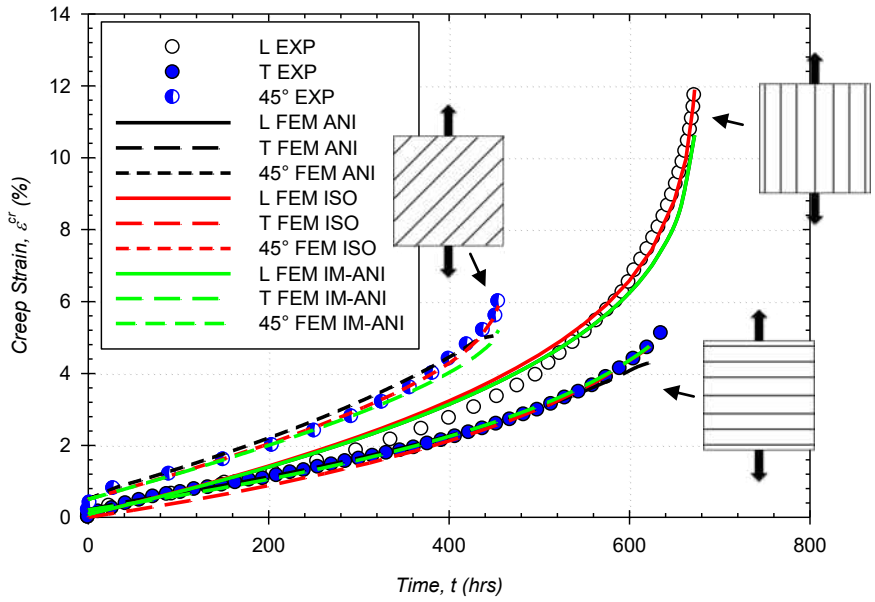

Figure 7.9 - Creep deformation on the x_3 normal of the ISO, ANI, and IM-ANI formulations compared with creep test data for DS GTD-111 under 289MPa uniaxial load and 871°C

Accurate modeling of damage evolution is critical to determine rupture time and a quality prediction of creep deformation. The improved anisotropic model (IM-ANI), produces greatly improved results over the anisotropic model (ANI) in terms of damage at intermediated orientations, particular at 45° as depicted in Figure 7.8. As observed IM-ANI matches exactly the damage evolution produced using the isotropic Kachanov-Rabotnov formulation (ISO) with optimized tertiary creep constants. Interestingly, IM-ANI produces the same damage evolution in the L orientation and a higher damage rate in the T orientation. The increase in the T orientation can be attributed to round of error due to rotation of the two (6x6) Hill compliance tensor associated with damage, in addition to slightly convergence differences between formulations. The damage evolution produce is highly accurate and while facilitate quality predictions of rupture.

Accurate modeling of creep deformation using IM-ANI is easily achieved. Figure 7.9 provides creep deformation using the ISO, ANI, and IM-ANI models compared to uniaxial creep tests experiments. It is observed that IM-ANI produces improved predictions in the 45° and T orientations compared to the ANI formulation. The modeling of the 45°-oriented tertiary creep behavior is greatly improved.

An examination of the tensorial creep deformation using IM-ANI is now necessary. Figure 7.10 depicts the components of creep deformation for L, T, and 45°-oriented specimen. IM-ANI produces components very similar to that produced using ANI. Slight changes are observed in the 45° and T-oriented specimen. This is due to increased damage rates compared to ANI.

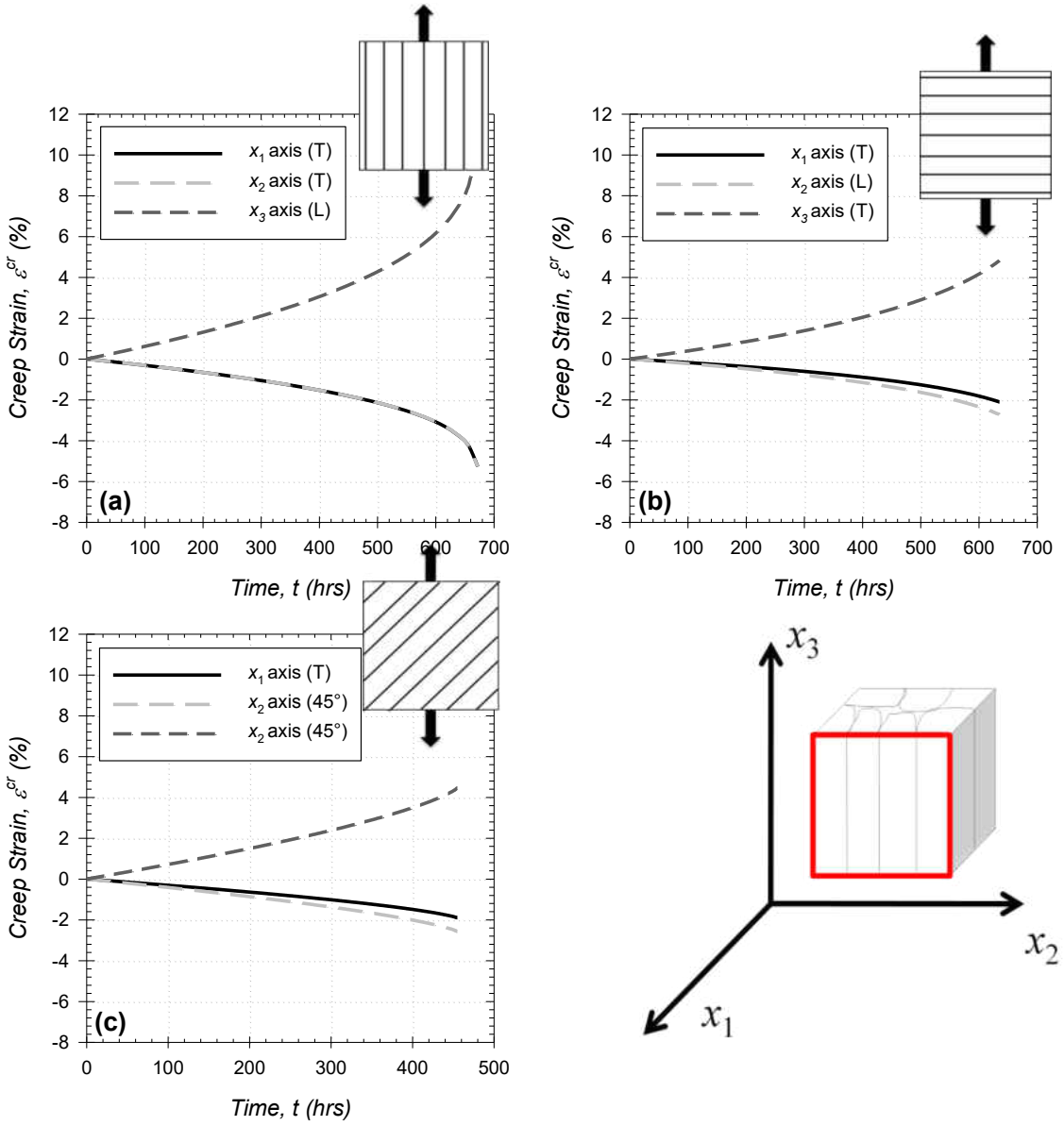

Figure 7.10 - Components of the creep deformation using the IM-ANI formulation for (a) L, (b) T, and (c) 45°-oriented specimen under 289MPa uniaxial load and 871°C (note: primary creep is neglected)

The use of the Cauchy stress vector and Hill compliance tensor directly in damage evolution, Eq. (6.7), results in implicit induced anisotropy. Thus the effect of multiaxial states of stress can be directly produced. A parametric look at various states of stress is provided in Chapter 8.

7.5 Isotropic Rupture Prediction

Before analyzing the rupture time predictions using the isotropic rupture time prediction model Eq. (4.9), it is necessary to study the isotropic damage prediction Eq. (4.10), which will help facilitate an accurate estimate of critical damage. Work by MacLachlan and Knowles [43] suggests that critical damage is a limited by the ultimate tensile strength (UTS). Since the UTS is the maximum resistance to fracture it is a justly assumed criterion. Failure is reached when the net/effective stress Eq. (4.3) is equivalent to the UTS and takes the form

$$\bar{\sigma}_{net} = \frac{\bar{\sigma}}{(1-\omega)} \Rightarrow \omega_f = \frac{UTS - \bar{\sigma}}{UTS} \tag{7.4}$$

where simplification provides a estimate of critical damage. Table 7.3 provides a comparison of the isotropic (ISO), MacLachlan-Knowles (M-K), and half M-K damage predictions. The negative values of relative error demonstrate that the isotropic model (ISO) produces much lower values of critical damage when compared to M-K estimates. This inconsistency can be explained. The MacLachlan and Knowles damage formulation directly includes the UTS in the form

$$\frac{d\omega}{dt} = C \times \left(\frac{\bar{\sigma}_{net}}{UTS - \bar{\sigma}_{net}} \right)^{v} \tag{7.5}$$

where C and v are constants. This provides a method by which failure is assumed when net/effective stress is equal UTS. The UTS directly influences not only the point of critical damage but also the rate of damage. The isotropic creep damage formulation does not directly

included UTS, thus the net/effective stress nears infinity at failure and the damage evolution is not altered. For the purposes of this study, it is found that reducing the M-K estimate by half greatly reduced the error between predicted critical damage. This has substantial benefits.

Of importance is the relationship between stress and critical damage. Inspection of the applied stress versus critical damage is provided in Figure 7.11. It is observed that the ISO critical damage prediction produces a similar trend to the half M-K estimates. With additional creep tests a well defined stress-critical damage curve can be obtained. A function could be created using either prediction methods to determine critical damage at a set temperature and orientation.

Table 7.3 - Damage Predictions for DS GTD-111

Matl. Orient.	Temperature		Stress		Ultimate Tensile Strength (UTS)	Critical Damage, ω_f			Relative Error	
α	(°C)	(°F)	(MPa)	(ksi)	(MPa)	M-K	M-K/2	ISO	M-K	M-K/2
L (0°)	649	1200	896	130	1110.00	0.19	0.10	0.05	-76.39%	-52.77%
L (0°)	760	1400	408	60	1108.00	0.63	0.32	0.35	-44.41%	11.18%
L (0°)	760	1400	613	89	1108.00	0.45	0.22	0.13	-71.20%	-42.39%
T (90°)	760	1400	517	75	974.00	0.47	0.23	0.13	-72.29%	-44.58%
T (90°)	760	1400	613	89	974.00	0.37	0.19	0.03	-91.00%	-81.99%
L (0°)	816	1500	455	66	991.16	0.54	0.27	0.58	7.71%	115.43%
T (90°)	816	1500	455	66	932.72	0.51	0.26	0.06	-87.56%	-75.12%
L (0°)	871	1600	241	35	802.00	0.70	0.35	0.25	-64.92%	-29.84%
L (0°)	871	1600	289	42	802.00	0.64	0.32	0.22	-65.35%	-30.71%
T (90°)	871	1600	241	35	834.00	0.71	0.36	0.43	-39.07%	21.85%
T (90°)	871	1600	289	42	834.00	0.65	0.33	0.26	-60.22%	-20.44%
L (0°)	940	1724	244	35	457.99**	0.47	0.29	0.31	-34.33%	6.98%
T (90°)	940	1724	244	35	626.57**	0.61	0.26	0.24	-61.24%	-10.37%
L (0°)	982	1800	124	18	191.38**	0.35	0.37	0.57	62.25%	54.53%
L (0°)	982	1800	145	21	191.38**	0.24	0.35	0.33	37.97%	-3.81%
45°*	871	1600	289	42	641.21**	0.55	0.27	0.11	-79.92%	-59.84%

*[84], **[111]

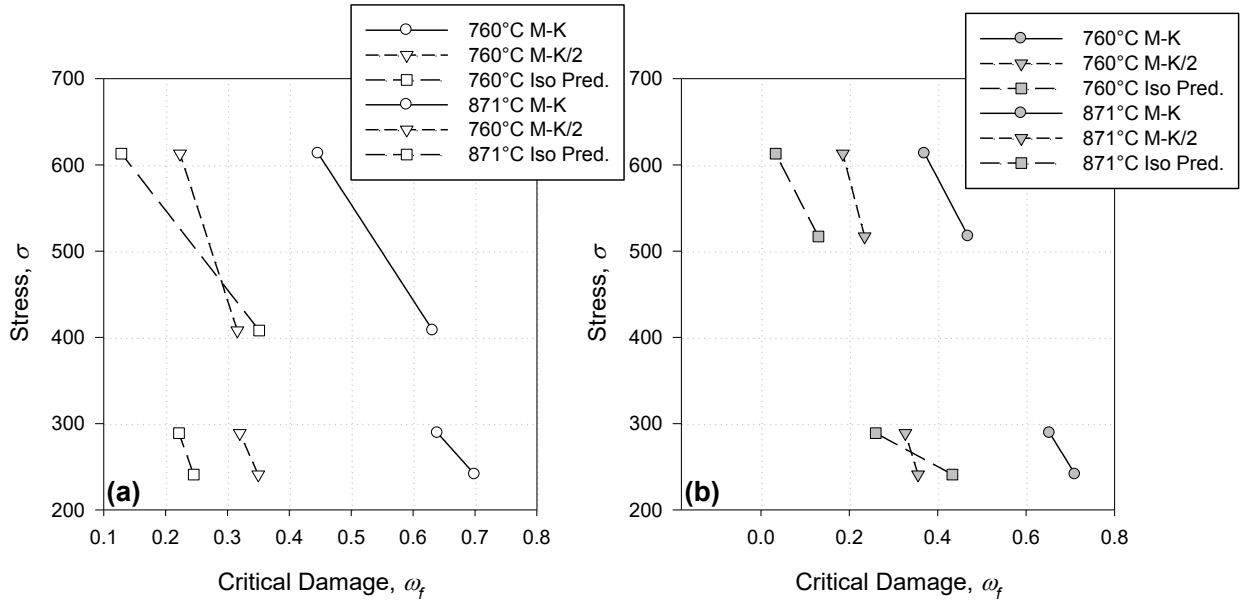

Figure 7.11 – Stress-Damage curves for (a) L and (b) T orientations at 760 and 871°C

Taking the lessons learned from critical damage prediction, rupture time predictions using Eq. (4.9) are performed. Table 7.4 provides rupture time predictions at various set levels of critical damage. The least conservative estimate is when critical damage is set to unity ($\omega_f = 1.0$). This assumes failure occurs at a net/effective stress of infinity. Four rupture predictions were non-conservative with the highest at $1.182t_f$. Next the critical damage is set to 0.25. This is approximately the average value produced using the isotropic critical damage predictions in Table 7.3. This provides the second best predictions in terms of conservatism, with only two non-conservative predictions the highest being $1.0794t_f$. Next critical damage is set to M-K. This generates the results similar to critical damage at unity. Four rupture predictions were non-conservative with the highest at $1.1622t_f$. Reducing to half M-K, generates the most conservative predictions with three non-conservative rupture predictions the highest at $1.0757t_f$.

Table 7.4 – Rupture Time Predictions for DS GTD-111

Matl. Orient.	Temperature		Stress		Experimental Rupture Time, t_f	Predicted Rupture Time, t_{rup} *(hr)*			
α	(°C)	(°F)	(MPa)	(ksi)	(hr)	ω = 1.0	ω = 0.25	ω = M-K	ω = M-K/2
L (0°)	649	1200	896	130	465.9	502.9	502.9	502.9	501.2
L (0°)	760	1400	408	60	5624.0	5533.2	5173.4	5532.8	5383.0
L (0°)	760	1400	613	89	243.6	213.6	210.1	213.6	207.8
T (90°)	760	1400	517	75	375.7	338.3	334.7	338.3	333.4
T (90°)	760	1400	613	89	42.6	34.1	34.1	34.1	34.1
L (0°)	816	1500	455	66	321.5	326.5	244.2	318.6	254.4
T (90°)	816	1500	455	66	127.0	110.8	110.8	110.8	110.8
L (0°)	871	1600	241	35	2149.0	1952.8	1766.2	1952.7	1894.6
L (0°)	871	1600	289	42	672.2	629.1	600.1	629.1	618.9
T (90°)	871	1600	241	35	980.2	1158.5	709.6	1139.2	886.2
T (90°)	871	1600	289	42	635.3	701.9	628.0	701.8	670.1
L (0°)	940	1724	244	35	68.7	65.3	58.9	64.9	61.0
T (90°)	940	1724	244	35	62.5	70.5	63.6	70.5	64.6
L (0°)	982	1800	124	18	821.3	799.9	566.3	675.0	688.9
L (0°)	982	1800	145	21	301.7	278.7	230.8	227.8	258.3
*45°	871	1600	289	42	455.0	422.4	421.7	422.4	422.1

*[84]

In most cases where non-conservative estimates were found, the least squares value at the end of optimization was high. This signifies that additional optimization using a more advanced routine could produce improved constants resulting in a better estimate of rupture time. In all cases, the rupture time predictions are within a factor of 1.2. When applying a factor of 1.2 or greater, rupture time predictions using a critical damage of unity can be taken as is. Figure 7.12 provides a visual representation of the rupture time predictions compared to experimental. It shows that reducing the value of critical damage increases the conservatism of rupture time

predictions. It also shows predictions with critical damage at unity, although the least conservative, are acceptable.

The following method should be used when attempting to produce the most conservative estimates of rupture time. The MacLachlan-Knowles (M-K) critical damage Eq. (7.4) should be found using the materials UTS. The M-K estimates should be reduced by half and applied within the rupture time prediction. The advantage of the M-K method is that it provides critical damage estimates for the temperature range of available UTS data and at level of applied stress. The disadvantage however, is that UTS data is needed at intermediate material orientations when estimate rupture time between $0° \leq \alpha \leq 90°$. For transversely-isotropic materials, the MacLachlan-Knowles estimate is not applicable without extensive mechanical testing.

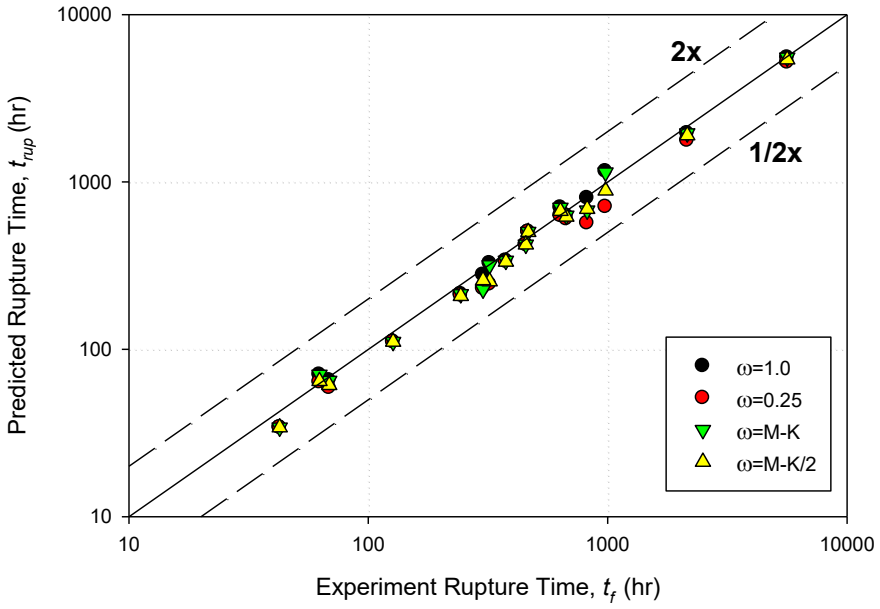

Figure 7.12 – Rupture Time Comparison

7.6 Anisotropic Rupture Prediction

Before analyzing the rupture time predictions using the derived anisotropic rupture time prediction model Eq. (5.11), it is necessary to study the derived anisotropic damage prediction Eq. (5.12), which will help facilitate an accurate estimate of critical damage. The anisotropic formulation requires creep test experimental data for L, T, and 45°-oriented specimen in order to function properly. Taking the material constants listed in Table 7.2 and the derived anisotropic damage prediction model Eq. (5.11), critical damage is predicted. Table 7.5 provides a comparison of the derived anisotropic (ANI), isotropic (ISO), and half M-K critical damage predictions at 871°C and 289 MPa. Similarly, Figure 7.13 presents this data in a graphical form. It is observed that in terms of critical damage the ANI model predictions aligned with that of the ISO model. It is similarly discovered that at intermediate orientations the critical damage is found to reducing using half M-K. This suggests that the creep rupture strength of the material between L and T orientations is reduced. The ANI and ISO models both successfully model this behavior but with higher reductions in critical damage at intermediate orientations. It should be noted that both the ANI and ISO prediction models require the experimental rupture time to predict critical damage; therefore, they cannot be used to predict critical damage at orientations where rupture time data is not available. It should also be noted that the M-K method requires UTS material data; therefore, it cannot be used to predict critical damage at orientations where UTS data is not available. In all situations extensive mechanical and/or creep tests are required to estimate critical damage at intermediate orientations. As suggested in the previous subsection,

using a critical damage of unity can provide a viable estimate of rupture time, despite slight non-conservatism in some cases.

Table 7.5 – Anisotropic Damage Predictions for DS GTD-111 at 871°C

	Temperature		Stress		Ultimate Tensile Strength (UTS)	Critical Damage, ω_f		
	(°C)	(°F)	(MPa)	(ksi)	(MPa)	M-K/2	ISO prediction	ANI prediction
L	871	1600	289	42	802.00	0.32	0.255	0.255
45°*	871	1600	289	42	641.21**	0.27	0.11	0.121
T	871	1600	289	42	834.00	0.33	0.26	0.26

*[84], **[111]

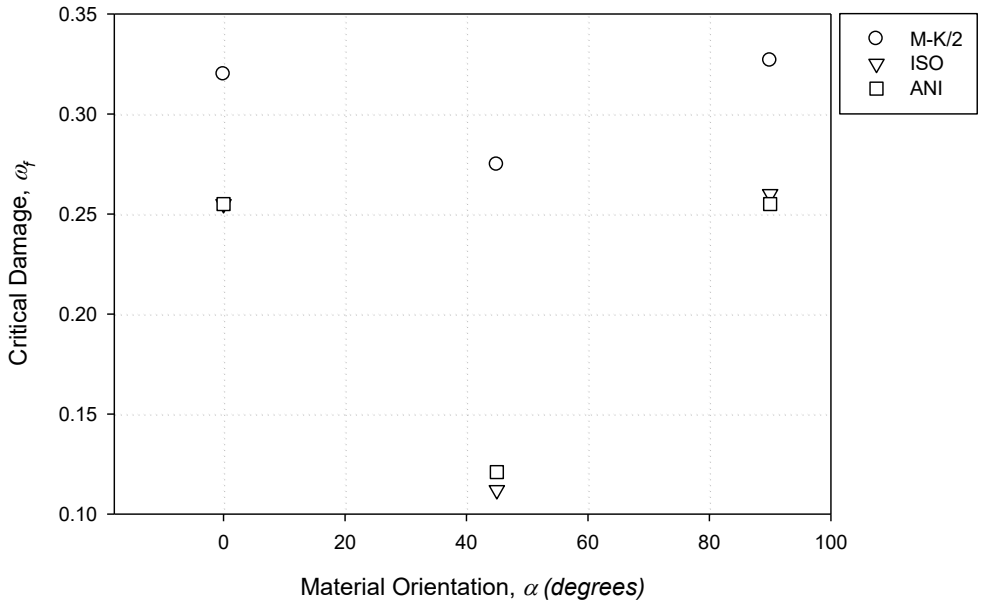

Figure 7.13 - Critical damage versus material orientation

Taking the lessons learned from critical damage prediction, rupture time predictions using Eq. (5.11) are performed. Table 7.6 provides rupture time predictions at critical damage of unity and half M-K. Examining the data, it is found that for L and T orientations, the ANI and ISO rupture time predictions are equal. The derived ANI rupture model, regresses to the ISO model at 0° and 90° material orientations. Thus the same predicted values found using ISO are found using ANI. A problem arises at the 45° material orientation. The ANI prediction is not similar to the ISO prediction. This inconsistency is a result of the damage formulation not accurately modeling damage evolution at 45° as discussed in subsection 6.3. In all cases, (L, T, and 45°-oriented) further optimization of the tertiary creep damage constants could improve rupture time predictions.

A parametric study of the rupture prediction with critical damage set to unity is provided in comparison to ISO predictions and experimental data is provided in Figure 7.14. The behavior observed is not consistent with the known behavior exhibited in transversely isotropic materials. This behavior should be similar to that found for minimum creep strain rate versus orientation (Figure 7.4) where strain hardening occurs. The strain hardening will cause a reduction in rupture time found at intermediate orientations. Using the half M-K critical damage it is found that there is a slight reduction in rupture time prediction at the 45° orientation but not enough to be applicable.

From the results of rupture time prediction (Figure 7.14) and of damage evolution (Figure 7.5) it is observed that a damage evolution formulation that can account for the strain hardening at intermediate orientations requires development.

Table 7.6 – Anisotropic Rupture Time Predictions for DS GTD-111

	Temperature		Stress		Experimental Rupture Time, t_f	Predicted Rupture Time, t_{rup}			
						ISO		ANI	
	(°C)	(°F)	(MPa)	(ksi)	(hr)	ω = 1.0	ω = M-K/2	ω = 1.0	ω = M-K/2
L	871	1600	289	42	672.2	629.1	618.9	629.1	618.9
45°*	871	1600	289	42	455.0	422.4	422.1	653.071	617.7
T	871	1600	289	42	635.3	701.9	670.1	701.9	670.1

*[84]

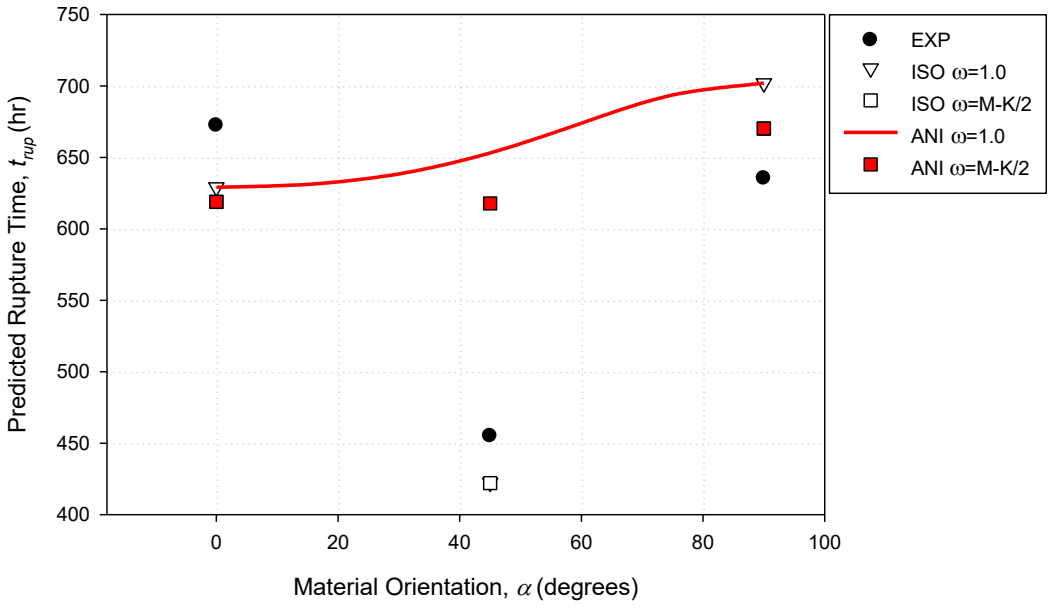

Figure 7.14 – Novel anisotropic rupture time predictions at various material orientations

7.7 Improved Anisotropic Rupture Prediction

As discussed in the previous section, the M-K method is not readily applicable to transversely-isotropic materials due to the requirement of UTS data which may not be available at intermediate material orientations. Thus for IM-ANI, M-K is not evaluated.

First an examination of critical damage predictions using IM-ANI, Eq. (6.12), is performed. A comparison of ISO, ANI, and IM-ANI is proved in Table 7.7. Again it is observed that the critical damage predictions only vary slightly between the three formulations. In the case of IM-ANI critical damage is assumed to be equal to that found in the component where fracture is expected to occur. In the current case, this is on the plane parallel to uniaxial loading. As previously states, the ISO, ANI, and IM-ANI formulations all require the final rupture time to be know in order to prediction critical damage, therefore critical damage predictions are not particularly useful because they require creep test data before a prediction can be made. However, when test data creep is available, a numerical formulation can be developed where critical damage is calculated for every element in a finite element component. Then as elements reach critical damage they can be removed, leading to a finite element creep-crack propagation method.

Table 7.7 – Improved Anisotropic Damage Predictions for DS GTD-111 at 871°C

	Temperature		Stress		Critical Damage, ω_f		
	(°C)	(°F)	(MPa)	(ksi)	ISO	ANI	IM-ANI
L	871	1600	289	42	0.255	0.255	0.255
45°*	871	1600	289	42	0.112	0.121	0.119
T	871	1600	289	42	0.26	0.26	0.26

*[84]

An examination of the rupture time prediction using IM-ANI is conducted. Using the derived analytical rupture time prediction model, Eq. (6.12), predictions are found for L, T, and intermediately oriented specimen. As observed in Figure 7.15, IM-ANI is able to produce results which intersect with ISO predictions at L(0°) ,T (90°), and 45°. Interestingly, the minimal rupture time is found at approximately 60°. This can be contributed to the state of stress. A Uniaxial loading is applied on the x_3 axis. The orientation of the material relative to the first principal stress direction contributes to a reduction in time before failure.

The remarkable ability of this rupture time prediction model to work for any arbitrary state of stress and/or material orientation allows interesting possibility in modeling. For instance, an elastic FE solution of a component can be found. Then using the known state of stress and material orientation, the time to rupture of each element can be predicted.

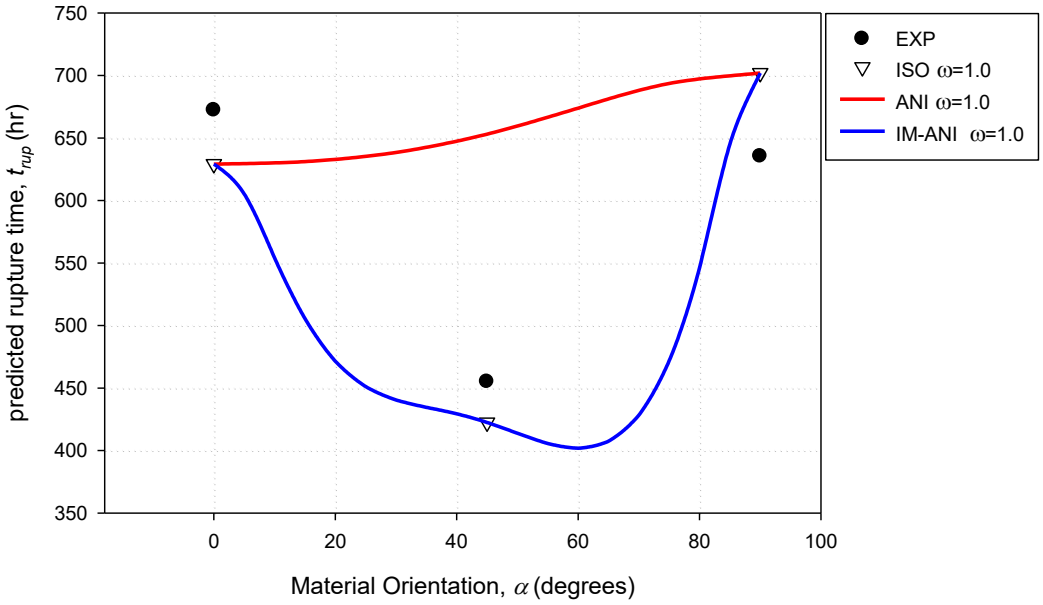

Figure 7.15 - Improved anisotropic rupture time predictions at various material orientations

CHAPTER EIGHT: PARAMETRIC STUDY

8.1 Introduction

Examining the results found in Chapter 7, it is determined that the improved anisotropic creep damage formulation (IM-ANI) produces the most accurate tensors for damage and creep strain compared to the isotropic Kachanov-Rabotnov formulation (ISO) and the developed novel anisotropic creep damage formulation (ANI).

It is important to note that the performance of the IM-ANI formulation when it is applied to various material orientations and states of stress. It is an important feature that the formulation accurately predicts damage evolution and creep deformation under these various conditions. First a material orientation study is performed under both uniaxial tension and compression. Rotation about the x_1 axis is performed where the body is rotated from L to T ($0° \leq \alpha \leq 90°$) and where creep deformation and damage evolution on the x_3 normal are collected. Next, a uniaxial stress rotation is performed on L, 45°, and T-oriented specimen ($0° \leq \beta \leq 90°$) where creep deformation and damage evolution on the x_3 normal are collected. This stress rotation process is repeated for biaxial, pure shear, and triaxial states of stress. Finally, rupture time predictions using Eq. (6.12), are performed for uniaxial, biaxial, pure shear, and triaxial states of stress for L,45°, and T-oriented specimen.

8.2 Material Orientations under Uniaxial Tension and Compression

Using the novel anisotropic model, a parametric study of the damage and creep strain that develops under different material orientations was performed (where an L specimen coincides with 0° and a T specimen with 90°). The material transformation tensor, **T** takes the following form

$$\mathbf{T}=\begin{bmatrix} 1 & 0 & 0 & 0 & 0 & 0 \\ 0 & \cos(\alpha)^2 & \sin(\alpha)^2 & 0 & 0 & \cos(\alpha)\sin(\alpha) \\ 0 & \sin(\alpha)^2 & \cos(\alpha)^2 & 0 & 0 & -\cos(\alpha)\sin(\alpha) \\ 0 & 0 & 0 & \cos(\alpha) & -\sin(\alpha) & 0 \\ 0 & 0 & 0 & \sin(\alpha) & \cos(\alpha) & 0 \\ 0 & -2\cos(\alpha)\sin(\alpha) & 2\cos(\alpha)\sin(\alpha) & 0 & 0 & \cos(\alpha)^2-\sin(\alpha)^2 \end{bmatrix} \tag{8.1}$$

where α represents an angle relative to the x_3 normal (L-orientation). Uniaxial loading is applied in on the x_3 normal.

Under 289MPa tensile loading and 871°C, the damage evolution and creep deformation is shown in Figure 8.1. It is observed that the most rapid damage evolution occurs at 60° while the least rapid occurs at 90°. Creep deformation in the L, 45°, and T orientations correspond to experimental data and the ISO formulation. Interestingly, the creep deformation at 30° and 45° orientations are very similar. While at 60° the damage evolution is maximized, the creep deformation is minimal. This is of major concern.

Under 289MPa compressive loading and 871°C, the damage evolution and creep deformation is shown in Figure 8.1. The damage evolution is shown to be exactly the same as that produce for tensile loading. In experimental data, it is observed that damage is reduced under compressive loading. Traditionally, this reduction in damage is neglected due to limited compressive creep test data being available; therefore, the absolute values of tensile and compressive creep deformation correspond.

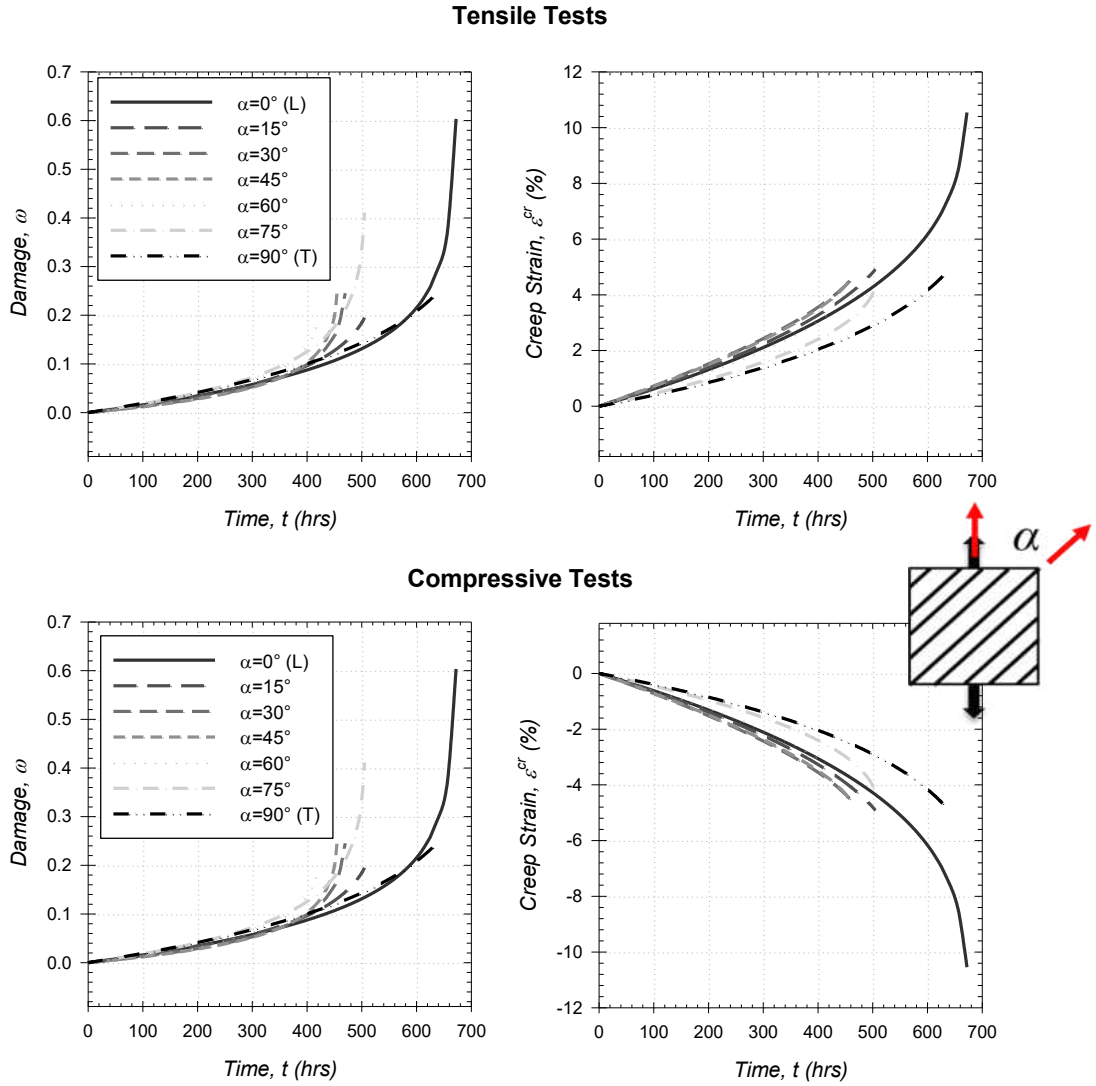

Figure 8.1 - Parametric material rotation study of creep deformation and damage evolution on the x_3 normal for tensile and compressive tests at 289MPa and 871°C

8.3 States of Stress

It is critical that the improved anisotropic creep damage (IM-ANI) formulation be able to successfully account for any applied state of stress; therefore, a parametric study under uniaxial, biaxial, pure shear, and triaxial loading conditions is performed.

First, a parametric uniaxial stress rotation study is performed for L, 45°, and T-oriented specimen under 289MPa and 871°C. The stress transformation tensor, **Q**, takes the following form

$$\boldsymbol{\sigma}' = \mathbf{Q}\boldsymbol{\sigma}\mathbf{Q}^T = \begin{bmatrix} 0 & 0 & 0 \\ 0 & 0 & 0 \\ 0 & 0 & \sigma_0 \end{bmatrix} \qquad \sigma_{vm} = \sigma_0 \qquad \mathbf{Q} = \begin{bmatrix} 1 & 0 & 0 \\ 0 & \cos(\beta) & \sin(\beta) \\ 0 & -\sin(\beta) & \cos(\beta) \end{bmatrix} \tag{8.2}$$

where rotation occurs about the x_1 axis. The creep deformation and damage evolution on the x_3 normal are collected and shown in Figure 8.5. Examining the damage evolution for all three specimen, the principal damage on the material x_3 orthogonal plane is found to reduce past β=45° as the first principal orientation switches to the material x_2 orthogonal plane. In the case of creep deformation, at β = 0°, for L,45°, and T-oriented specimen, the deformation is equivalent to that observed in the available experimental data, and predicted using the ISO formulation. For the remaining studies of biaxial, pure shear, and triaxial states of stress, tensorial terms of damage evolution and creep deformation may arise. To simplify interpretation of these results, the coordinate system (x_1,x_2,x_3) is replaced with the traditional to (X,Y,Z). This change is depicted in Figure 8.2.

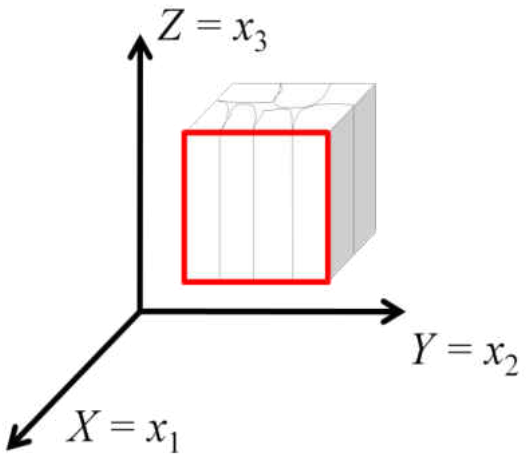

Figure 8.2 – Coordinate system transformation

Next, a study of the creep deformation and damage evolution tensors produced under biaxial loading of L, 45°, and T-oriented specimen is performed. The state of stress applied is in the following form

$$\boldsymbol{\sigma} = \begin{bmatrix} 0 & 0 & 0 \\ 0 & -\frac{\sqrt{3}\sigma_0}{3} & 0 \\ 0 & 0 & \frac{\sqrt{3}\sigma_0}{3} \end{bmatrix} \qquad \sigma_{vm} = \sigma_0 \qquad \sigma_m = 0 \tag{8.3}$$

where σ_0 equals 289MPa. The creep deformation and damage evolution tensors are collected and shown in Figure 8.6. Examining the damage evolution of all three specimen it is observed that the L and T specimen produce the same principal values with the exception that due to material rotation, the evolution in the L orientation on Y and Z switches to, in the T orientation, as Z and

Y. This is consistent with what is expected when under an equi-biaxial loading condition. Again it is observed that the 45° specimen produces an increased damage evolution compared to L and T. Creep deformation and damage evolution are still dependent on material orientation. In creep deformation, it is observed that the compressive stress on the Y normal produces a compressive creep strain on the Y normal. Under equibiaxial loading, the mean stress is zero thus the damage evolution on the X and Y normals is identical for the 45°-oriented specimen where damage behaviors the same on the X and Y normals. For the L and T-oriented specimen, the damage and creep deformation behavior is not identical. This can be attributed to the uniaxial creep damage behavior in associated with each normal. This slightly alters the damage evolution on each normal. A robustness of the IM-ANI formulation is observed.

A study of the creep deformation and damage evolution tensors produced under pure shear loading of L, 45°, and T-oriented specimen is performed. The state of stress applied is in the following form

$$\boldsymbol{\sigma} = \begin{bmatrix} 0 & 0 & 0 \\ 0 & 0 & \dfrac{\sqrt{3}\sigma_0}{3} \\ 0 & \dfrac{\sqrt{3}\sigma_0}{3} & 0 \end{bmatrix} \qquad \sigma_{vm} = \sigma_0 \qquad \sigma_m = 0 \tag{8.4}$$

where σ_0 equals 289MPa. The creep deformation and damage evolution tensors are collected and shown in Figure 8.7. The shear creep deformation observed in all three specimen is very near linear. This behavior is expected and is observed in other Ni-based superalloys [114]. It is

observed that for all three pure shear specimens, principal damage develops exactly the same as observed under biaxial loading. Under pure shear conditions, shear damage is shown by as

$$\tau = \frac{F}{A} \quad \Rightarrow \quad \tilde{\tau} = \frac{F}{A_D} \qquad D_s = 1 - \frac{A_D}{A} \tag{8.5}$$

where τ is the nominal shear strain, $\tilde{\tau}$ represents the effective shear strain, F is the nominal load, A is the undamaged area, and A_D is the reduced area. Similar to the assumptions made in ISO, ANI, and IM-ANI, the net are reduction is generalized into a phenomenological term, damage, ω, and is resolved on normal planes. Below is a figure that represents shear damage development in a single shear specimen (Figure 8.3).

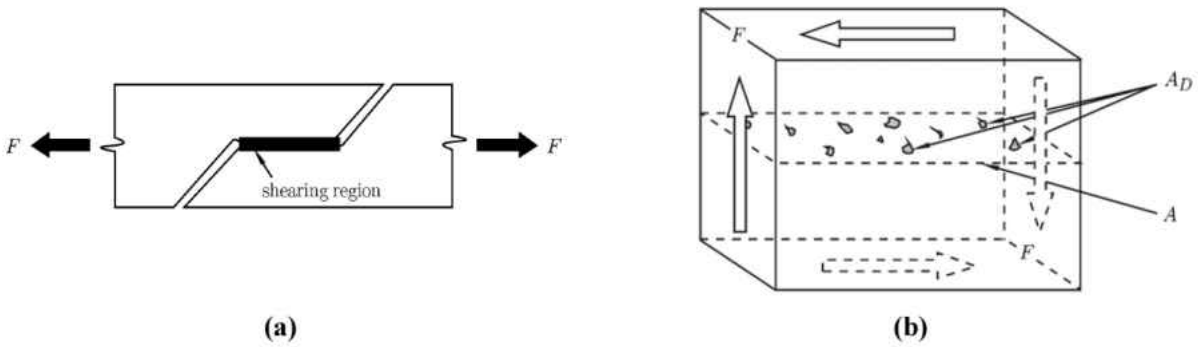

Figure 8.3 - Single shear specimen (a) shearing region (b) damage in representative element under pure shear strain [113]

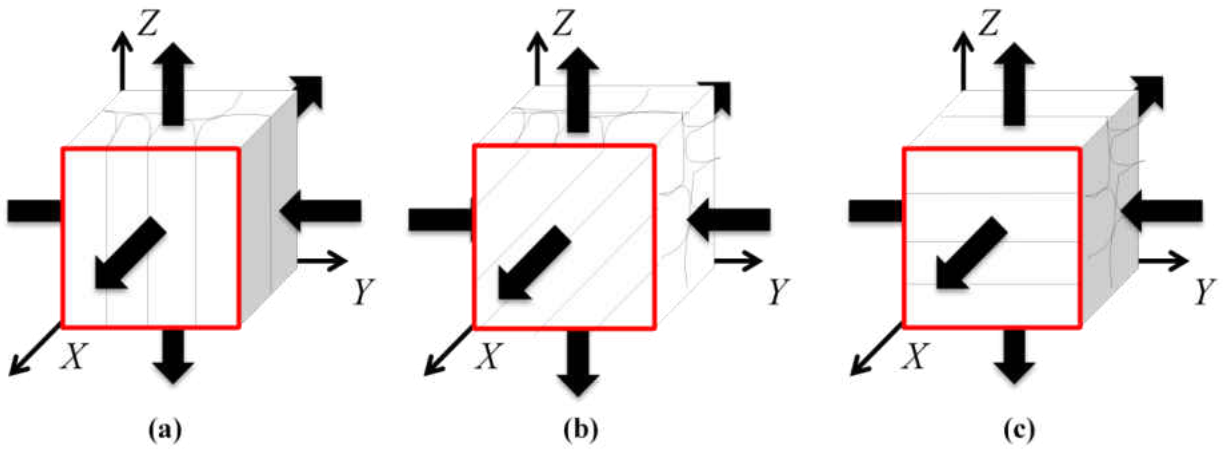

Figure 8.4 - Schematic of triaxial state of stress with visible material grain (note: under equitriaxial loading)

Finally, a study of the creep deformation and damage evolution tensors produced under triaxial loading of L, 45°, and T-oriented specimen is performed. The state of stress applied is in the following form

$$\boldsymbol{\sigma} = \begin{bmatrix} \frac{\sigma_0}{2} & 0 & 0 \\ 0 & -\frac{\sigma_0}{2} & 0 \\ 0 & 0 & \frac{\sigma_0}{2} \end{bmatrix} \qquad \sigma_{vm} = \sigma_0 \qquad \sigma_m = \frac{\sigma_0}{4} \tag{8.6}$$

where σ_0 equals 289MPa. The creep deformation and damage evolution tensors are collected and shown in Figure 8.8. Under triaxial loading conditions, the triaxiality of stress, (or the influence of mean stress and/or first principal stress on tensorial damage formation) can induce slightly counter intuitive results. Most famously, Hayhurst developed the following triaxial stress that replaces the effective stress in the isotropic formulations damage evolution [51,47].

$$\sigma_r = \left\langle \alpha\sigma_1 + 3\beta\sigma_m + (1-\alpha-\beta)\bar{\sigma} \right\rangle \cdot \tag{8.7}$$

The Hayhurst triaxial stress, σ_r, is related to the principal stress, σ_1, hydrostatic (mean) stress, σ_m, and the Von Mises effective stress, $\bar{\sigma}$, and includes two weight factors α and β that are determined from multiaxial creep experiments. Damage is found to evolve most briskly on the compressively loaded Y normal. Contributions from tensile loading on the X and Z normals accelerate Y normal damage evolution. For the L-oriented specimen (Figure 8.4a), equal tensile loading is found on the X and Z normals. The tensorial creep damage on X and Z are not the same. This is because the X and Z normals correspond to T and L uniaxial creep damage behaviors, respectively. For the 45°-oriented specimen (Figure 8.4b), again equal tensile loading is found on the X and Z normals. Similarly, the behavior on X and Z are not the same. This is because the X and Z normals correspond to T and 45° uniaxial creep damage behaviors, respectively. For the T-oriented specimen (Figure 8.4c), the exact same uniaxial creep damage behavior is expected and observed on the X and Z normals. This is due to equal tensile loading and uniaxial T creep damage behavior on both normals.

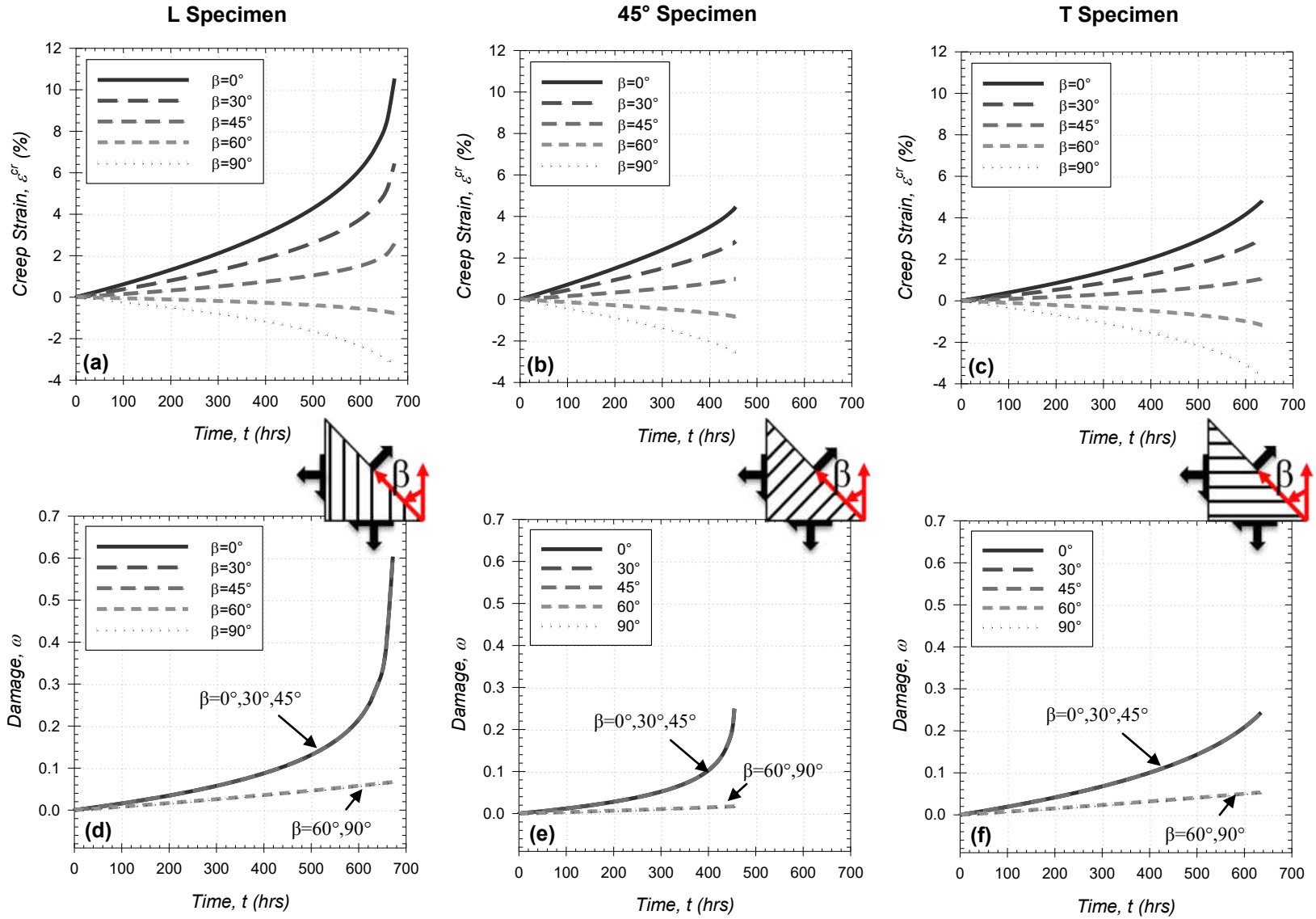

Figure 8.5 - Parametric uniaxial stress rotation study of creep deformation and damage evolution on the x_3 normal for an L, 45°,and T-oriented specimen (a), (b), and (c) respectively

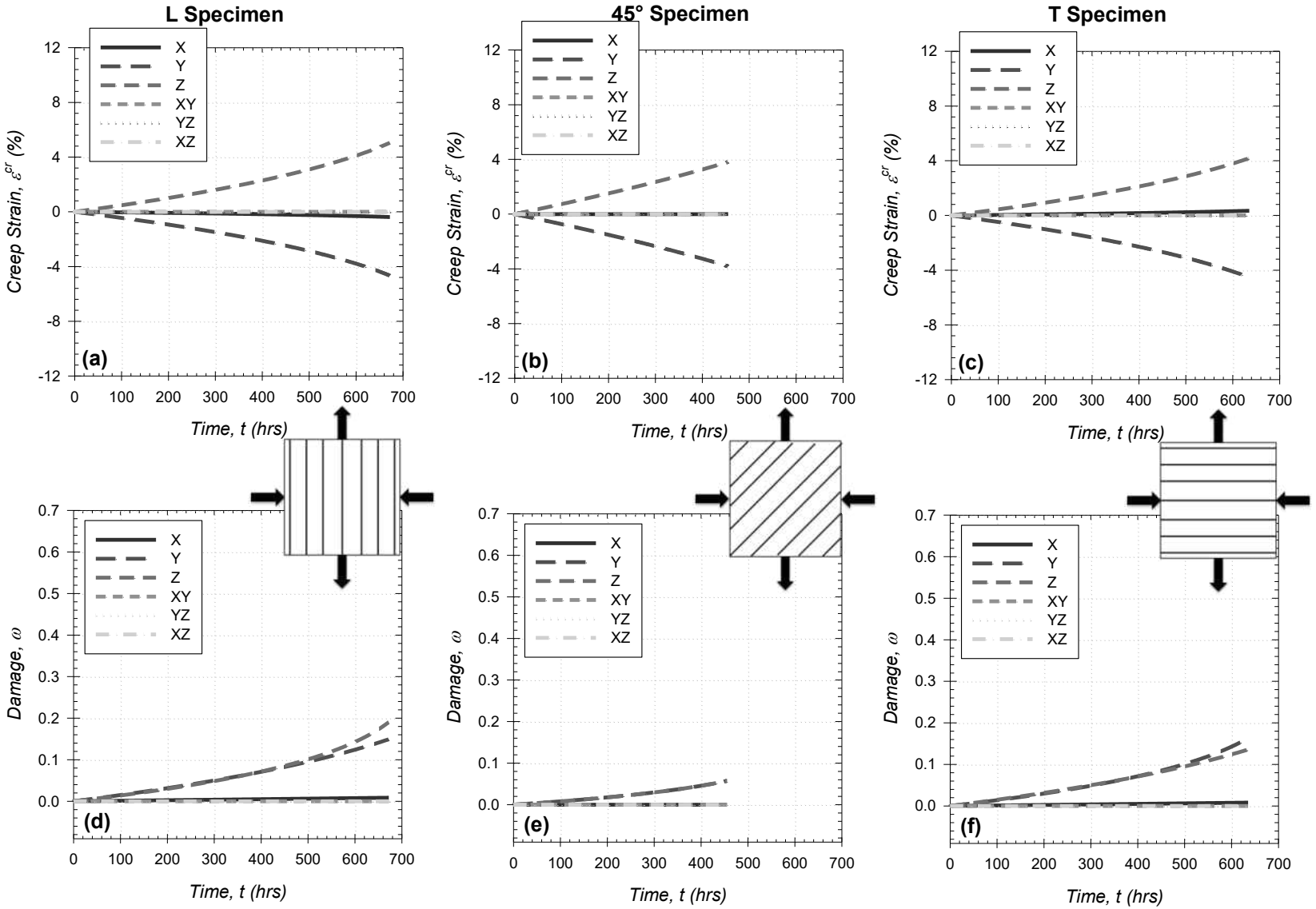

Figure 8.6 – Biaxially loaded creep deformation and damage evolution for an L, 45°,and T-oriented specimen (a), (b), and (c) respectively

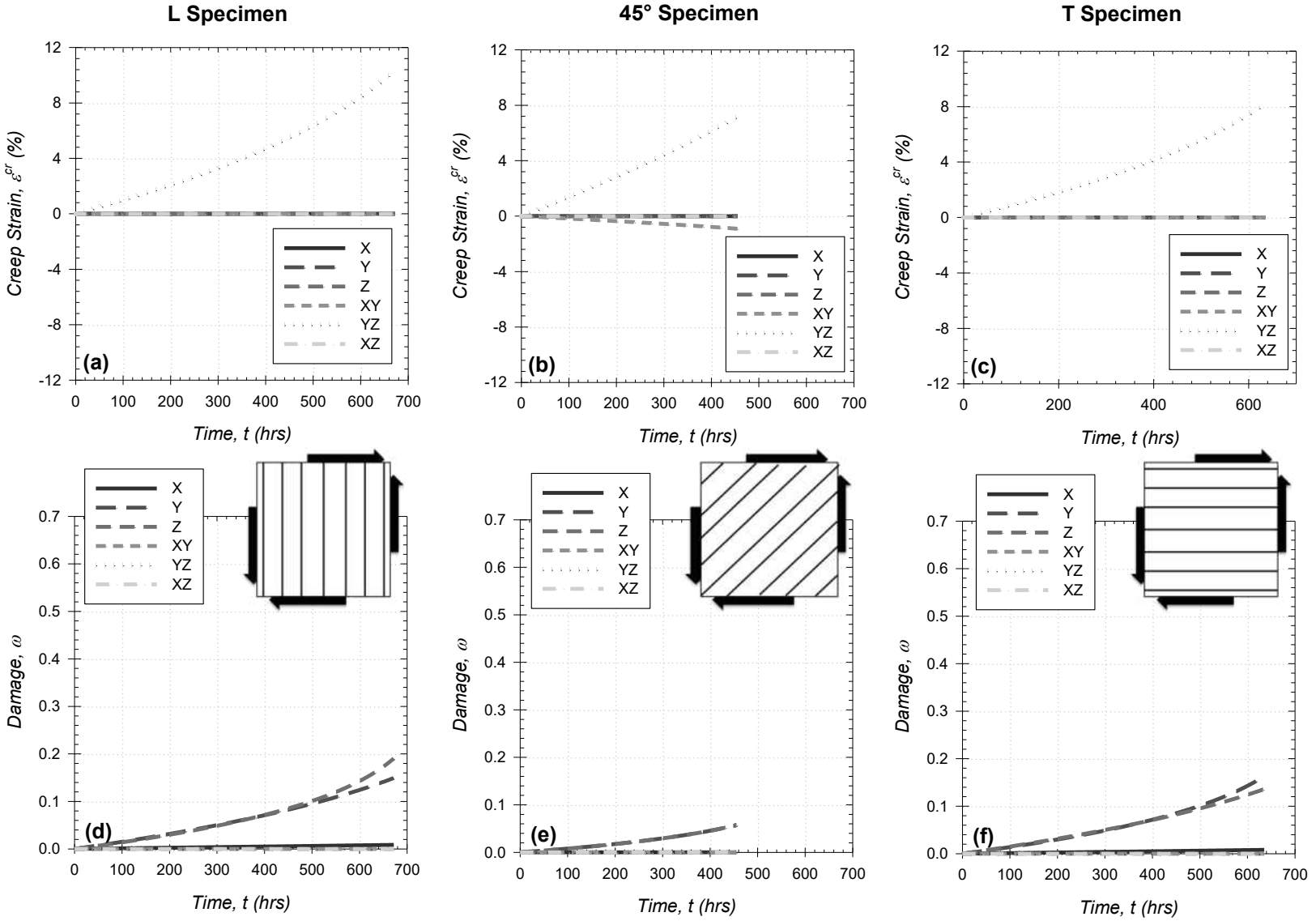

Figure 8.7 – Pure shear loaded creep deformation and damage evolution for an L, 45°,and T-oriented specimen (a), (b), and (c) respectively

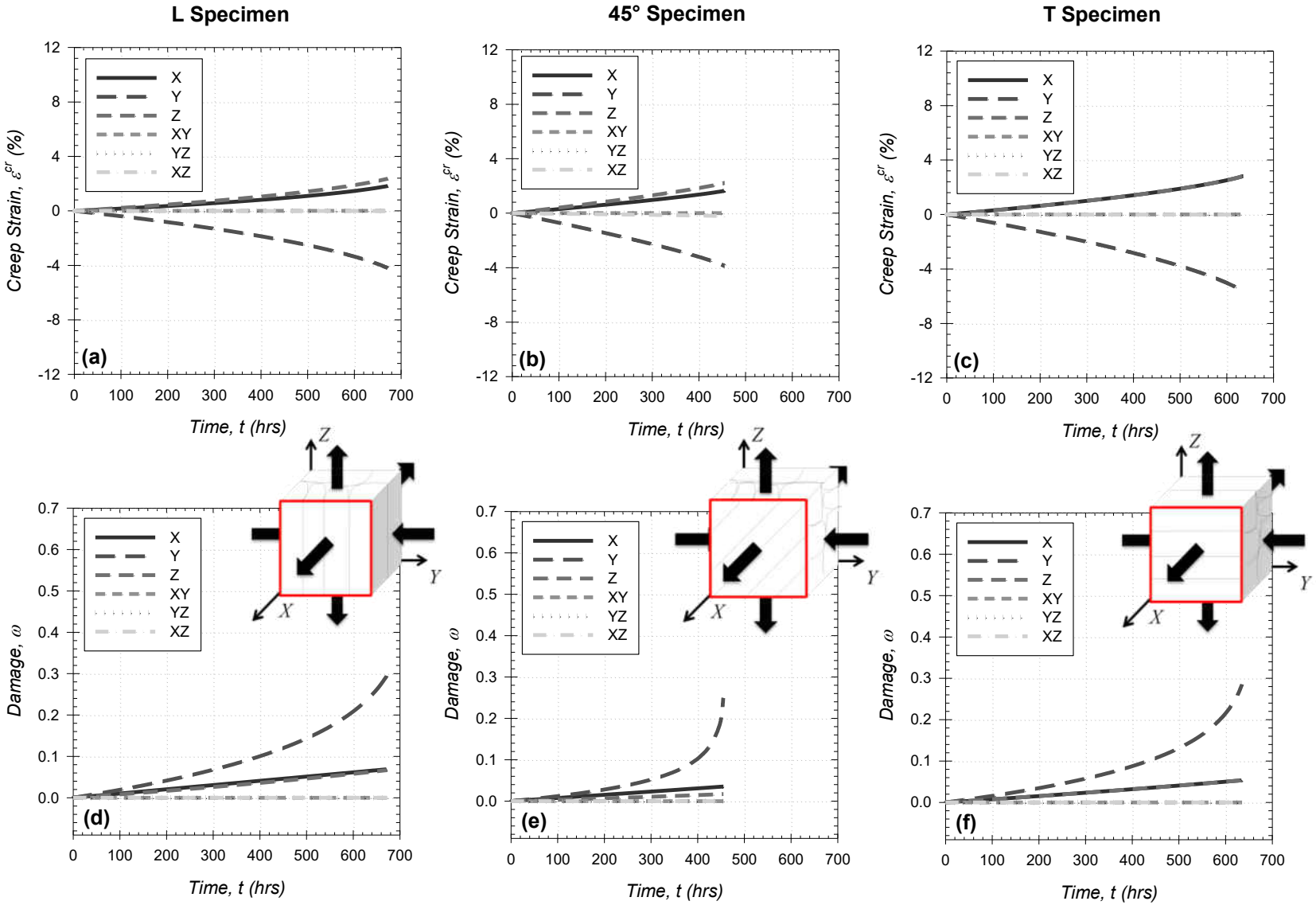

Figure 8.8 – Triaxially loaded creep deformation and damage evolution for an L, 45°,and T-oriented specimen (a), (b), and (c) respectively

8.4 Rupture Prediction

The improved anisotropic creep damage (IM-ANI) formulation contains a highly accurate damage mechanics formulation that when integrated produces rupture time predictions. The rupture time prediction, Eq. (6.12), requires a value of critical damage, ω_{cr} , to be assumed. In the current case $\omega_{cr} = 1.0$.

The strength of the IM-ANI rupture time prediction equation is that any state of stress and material orientation can be applied. Additionally, it can be used to predict the orientation upon which rupture will occur. The orientation with the minimal value of rupture time is the failure direction. To demonstrate, predictions of rupture time for uniaxial, biaxial, pure shear, and triaxial states of stress were applied for L, 45°, and T oriented specimen at 871°C and are listed in Table 8.1 through Table 8.4.

For uniaxial loading, load is applied on the Z normal. Naturally, rupture was found to occur on the Z normal in all cases. Under biaxial loading distinct rupture direction are found for the three specimen. For the L-oriented specimen, rupture is found on the Z normal. For the 45°-oriented specimen, rupture is found on both Y and Z normals. For the T-oriented specimen, rupture occurs on the Y normal. These are all due to the specific material behavior at the current material orientation and the applied states of stress. Under pure shear stress, load is applied on the YZ shear component. Naturally, rupture was found to occur on the YZ shear component in all cases. Interesting, under triaxial stress, rupture was found in all cases to occur on the Y

normal. This can be an attributed to the triaxiality of stress inducing a strong anisotropic response on the Y normal.

A plot of the stress against rupture time can be observed in Figure 8.9. Pure shear was found to produce the shortest rupture times while triaxial the longest. This is due to the loading conditions being based around von Mises equivalent stress instead of the internally used Hill's equivalent stress. This should be corrected in later studies. For all loading conditions, and at each material orientation (L, 45°, and T), the maximum load applied was equal to material ultimate tensile strength (UTS). At every instance a rupture time prediction was found at less than 200 hrs. Under UTS equivalent loading the rupture time should be minimal and related to ductile necking until rupture. Additional creep tests should be performed at the UTS in L, 45°, and T oriented specimen to determine the short time before failure. Then a comparison of the rupture predictions are this stress level can be performed.

A potentially useful property of the IM-ANI rupture time prediction equation is that it provides a method by which specimen rupture time can be predicted for conditions which may have been determined under purely elastic loading. When it is necessary to conduct multiple tests and available lab experiment time is limited. It can be used to produce states of stress and temperature that can be done within lab time limits.

Table 8.1 - Rupture predictions under uniaxial loading of DS GTD-111 specimens at 871°C

L		45°		T	
Stress (MPa)	Time (hr)	Stress (MPa)	Time (hr)	Stress (MPa)	Time (hr)
802	77	641	82	834	80
600	140	600	94	600	157
400	323	400	217	400	360
289	629	289	422	289	702
200	1340	200	900	200	1495
10	630100	10	423100	10	703000

Table 8.2 - Rupture predictions under biaxial loading of DS GTD-111 specimens at 871°C

L		45°		T	
Stress (MPa)	Time (hr)	Stress (MPa)	Time (hr)	Stress (MPa)	Time (hr)
802	91	641	120	834	91
600	166	600	138	600	166
400	381	400	317	400	381
289	743	289	618	289	743
200	1582	200	1316	200	1582
10	743900	10	618900	10	743900

Table 8.3 - Rupture predictions under pure shear loading of DS GTD-111 specimens at 871°C

L		45°		T	
Stress (MPa)	Time (hr)	Stress (MPa)	Time (hr)	Stress (MPa)	Time (hr)
802	91	641	120	834	91
600	166	600	138	600	166
400	381	400	317	400	381
289	743	289	618	289	743
200	1582	200	1316	200	1582
10	743900	10	618900	10	743900

Table 8.4 - Rupture predictions under triaxial loading of DS GTD-111 specimens at 871°C

L		45°		T	
Stress (MPa)	Time (hr)	Stress (MPa)	Time (hr)	Stress (MPa)	Time (hr)
802	87	641	82	834	71
600	157	600	94	600	140
400	360	400	217	400	323
289	702	289	422	289	629
200	1495	200	900	200	1340
10	703000	10	423100	10	630100

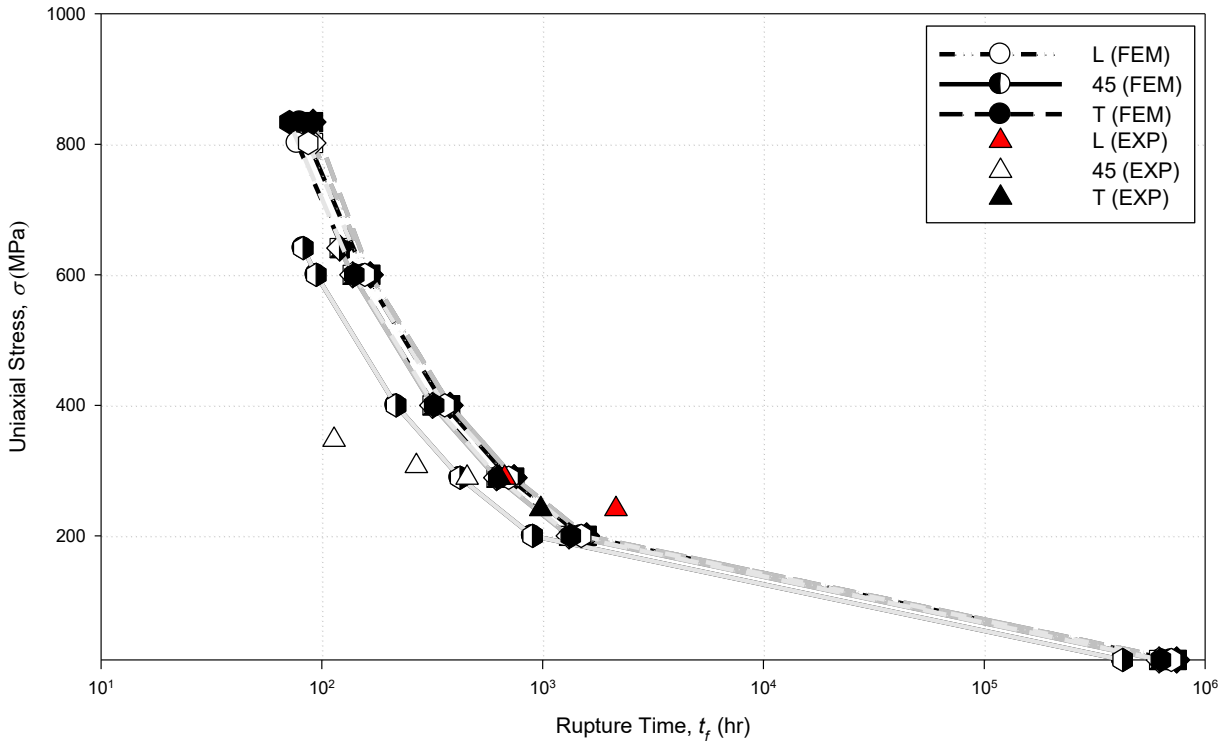

Figure 8.9 – Stress-rupture time curves for DS GTD-111 for L, 45°, and T-oriented specimen at 871°C with (a) unaixial – circle (b) biaxial – square , (c) pure shear – diamond , and (d) triaxial – hex

CHAPTER NINE: CONCLUSIONS AND FUTURE WORK

9.1 Conclusions

The damage evolution and creep deformation of DS GTD-111 has been characterized using three different creep damage constitutive models. Integration of these formulations has provided time to failure predictions at a high caliber of accuracy. The following conclusions can be drawn.

The Kachanov-Rabotnov isotropic creep damage formulation is found to successfully model the creep deformation behavior of DS GTD-111 in the uniaxial L, T, and 45° orientations. Using the available creep deformation data, secondary creep constants were analytically determined. Utilizing the uSHARP software, optimization with the simulated annealing algorithm produced tertiary creep constants that accurately predict the creep deformation at various stress and temperature conditions. The obtained secondary and tertiary creep constants were regression fit into a temperature-dependent form. These temperature-dependent functions are found to accurately and moderately match the optimized tertiary creep constants in the L and T orientations, respectively. Integration of the creep damage formulation provided critical damage and rupture time prediction models. A study of the predicted critical damage compared with MacLachlan-Knowles estimates shows that in general critical damage predicts are below the ultimate tensile strength equivalent net/effective stress. Rupture time predictions accurately matched the available creep rupture data when *a priori* critical damage was assumed unity.

Setting *a priori* critical damage to half the MacLachlan-Knowles critical damage estimate provides additional conservation in rupture time predictions. The isotropic creep damage formulation does not provide a full creep strain tensor for transversely-isotropic materials; therefore, it was necessary to develop the novel anisotropic tertiary creep damage formulation.

The novel anisotropic tertiary creep damage formulation (ANI) for transversely-isotropic materials performs equal to the Kachanov-Rabotnov isotropic tertiary creep damage formulation at modeling the creep response of L and T-oriented specimen of DS GTD-111. The novel formulation provides a full creep strain tensor for transversely isotropic materials based on a generalization of the Kachanov-Rabotnov formulation using the Hill's compliance tensor and a unique damage mechanics model. The developed damage mechanics model is analytical shown to work under various states of material orientation and stress. Using the creep deformation equation, an analytical method has been developed to determine the required Hill constants. The ANI formulation produces accurate creep strain tensor that accounts for elongation and angular distortions for L and T orientations but does not function correctly for intermediate material orientations ($0° < \alpha < 90°$). Slip plane damage is not accounted for; therefore, the damage mechanics model is inaccurate under material rotation. The inaccurate damage mechanics model leads to inaccurate and complicated critical damage and rupture time prediction models; therefore, it was necessary to develop the improved anisotropic creep damage formulation.

The improved anisotropic tertiary creep damage formulation for transversely-isotropic materials is able to accurately model the creep deformation in L, T, and 45°-oriented specimen. The improved formulation provides a full creep strain tensor for transversely-isotropic materials

based on a generalization of the Kachanov-Rabotnov formulation using the Hill compliance tensor in both the creep deformation and damage evolution equations. The model is able to accurately predict damage evolution and creep deformation under any state of stress and/or material orientation. Integration provides simple critical damage and rupture time prediction vectors where rupture time is equal to the minimal value. The orientation upon which failure is reached is assumed to be associated with the component where the minimal value is found. Rupture time predictions are accurate when compared with creep test data. The parametric study shows the model is well behaved under various materials orientations and uniaxial, biaxial, pure shear, and triaxial states of stress.

9.2 Future Work

Overall, the improved anisotropic creep damage formulation provides a solid foundation for modeling the creep damage behavior of transversely-isotropic materials. Additional work could be performed to improve the characterization of material behavior. Following are some recommendations for future work.

1) Limited uniaxial tensile creep test data is available for DS GTD-111. Scatter cannot be clearly identified and accounted for unless additional creep tests are performed. The number of creep test in the L, T, and 45° orientations are not equal. The temperature-dependence of creep constants for the T orientation suffers due to a lack of creep tests. The creep damage behavior in the 45° orientation is not well understood. To improved

damage evolution and creep deformation and rupture time predictions, additional creep tests are desired. At each temperature level for L, T, and 45°-oriented specimen, tests should be conducted at the same applied load.

2) No compressive creep tests are available for DS GTD-111. The tensile/compressive behavior of the subject material is not known. Modified net/effective stress equations, such as the Hayhurst triaxial stress, have been developed to account for tensile/compressive asymmetry. Compressive creep tests need to be conducted such that a modified net/effective stress can be implemented within the improved anisotropic creep damage formulation. Any required tensile/compressive weight factors could be obtained using uSHARP optimization.

3) Optimization was performed for each uniaxial creep test independently. This results in creep damage constants dependent on the individual behavior of a single creep test and not the generalized behavior observed from a set of tests. The optimization method should be modified such that all specimen at a particular orientation (L, T, or 45°) and temperature level are optimized within the same batch. This can be done utilizing the uSHARP software (Figure A.3).This would produce creep damage constants that are not specialize per-test but account for the generalized behavior of the material in a particular orientation and temperature at any stress level.

APPENDIX A: uSHARP SCREENSHOTS

Figure A.1 – uSHARP Logo

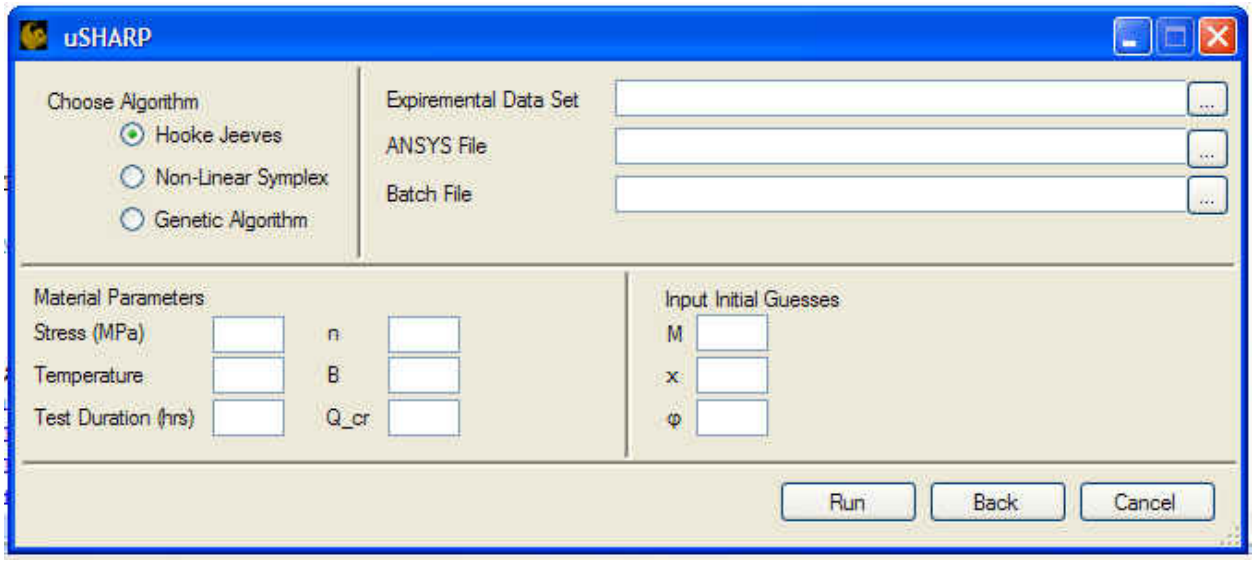

Figure A.2 - uSHARP main menu (single test optimization)

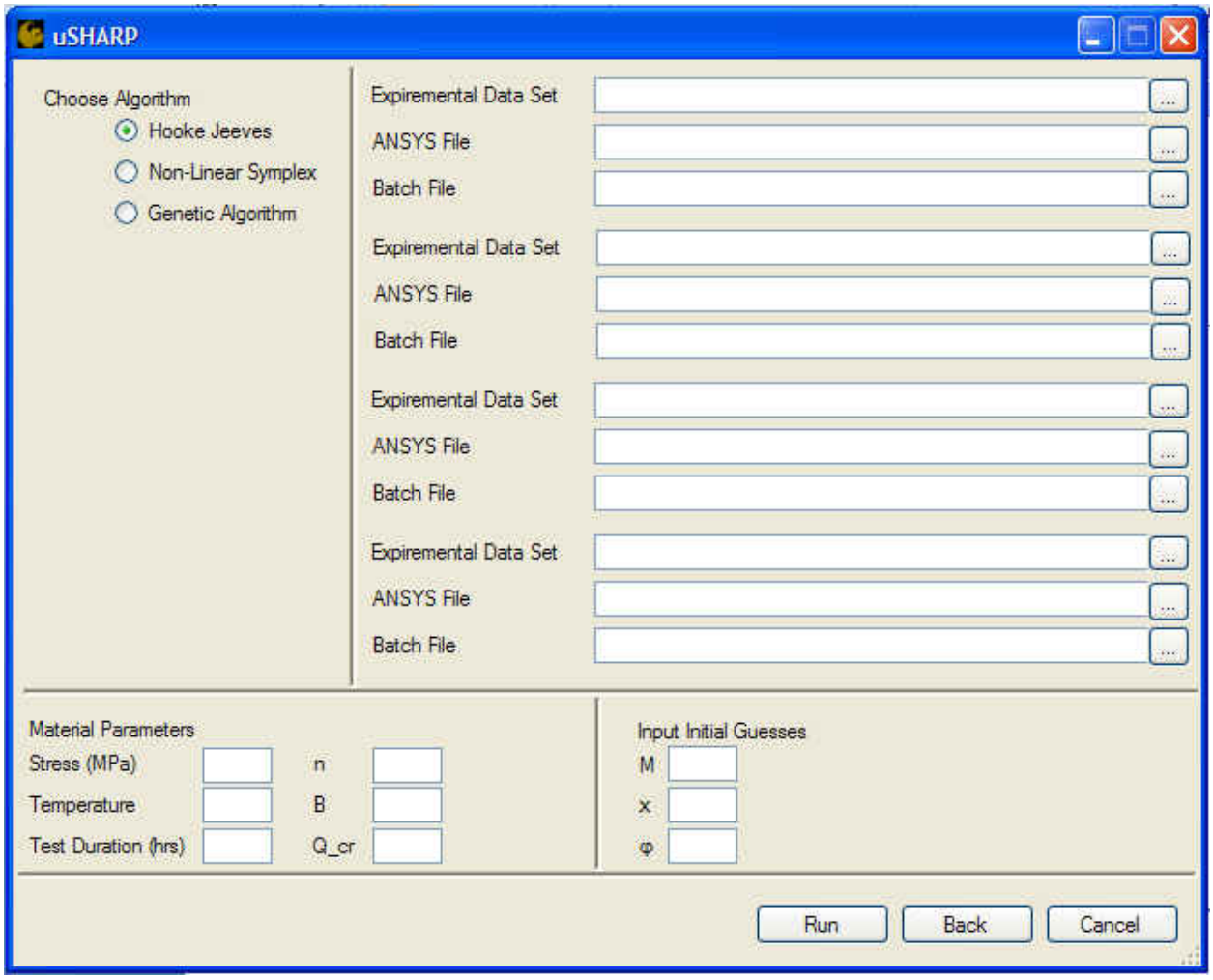

Figure A.3 - uSHARP main menu (batch test optimization)

APPENDIX B: HILL CONSTANTS DERIVATION

The material used to verify the model is the Ni-based superalloy DS GTD-111. DS GTD-11 is an "directionally-solidified" material commonly used in gas turbine applications [74]. It has been found to produce enhanced creep life, impact strength, corrosion and thermal fatigue resistance compared to its equiaxed counterpart [75-77]. The material is transversely-isotropic where isotropy is found in the x_1-x_2 plane while different materials properties are found on the x_3 normal plane (Figure B.1a).

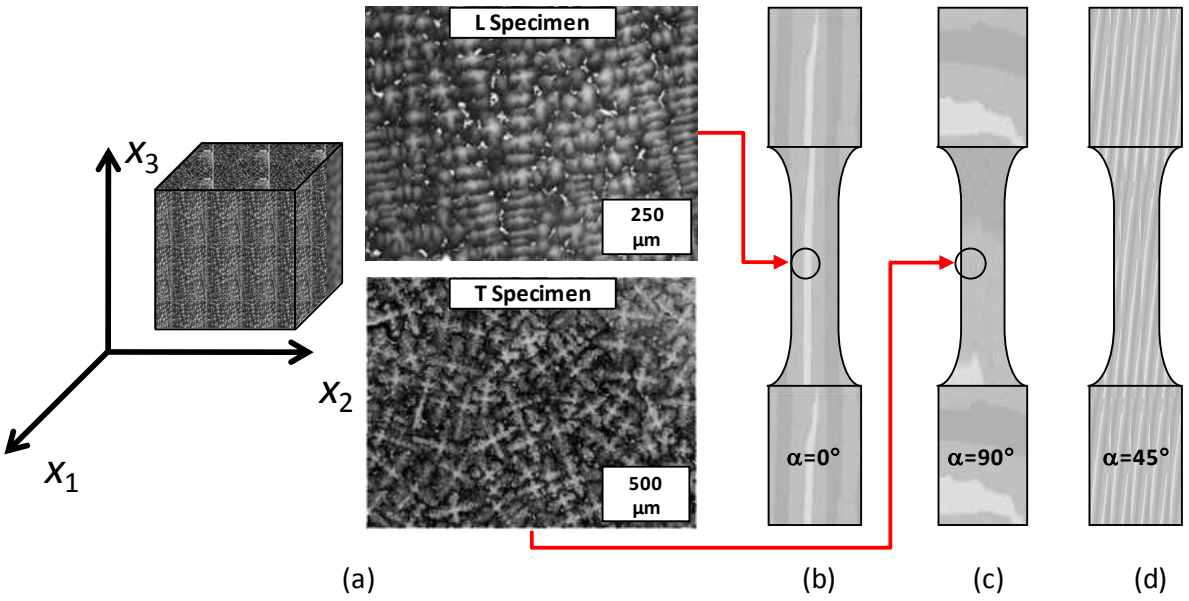

Figure B.1 - Grain schematic of DS GTD-111 (a) unit volume and grain structure (b) L-oriented (c) T-oriented (d) and 45°-oriented

To determine the secondary creep constants, A_{aniso} and n_{ansio}, and the Hill constants F, G, H, L, M, and N the authors derived constants from tensile specimen [27,104]. Previous research

by the authors has provided uniaxial A and n constants for DS GTD-111 [105]. These results where formulated as follows

$$\begin{aligned}\dot{\varepsilon}_{33}^{min} &= A_L \sigma^{n_L} \\ \dot{\varepsilon}_{33}^{min} &= A_T \sigma^{n_T} \\ \dot{\varepsilon}_{33}^{min} &= A_{45^\circ} \sigma^{n_{45^\circ}}\end{aligned} \tag{B.1}$$

where $\dot{\varepsilon}_{33}^{min}$ describes the minimum creep strain rate found in the specimen depicted in Figure B.1a, b, and c. Creep test data for DS GTD-111 oriented at 45° is not available. Following trends in 0°, 45°, and 90° data for comparable DS Ni-based superalloys a set of constants at 45° is deduced for DS GTD-111 [105-108]. Since the desire is to model secondary creep, damage evolution is neglected leading to the following form of the creep strain rate equation

$$\mathbf{e}^{cr} = A_{aniso} \sqrt{\mathbf{s}^T \mathbf{T}\mathbf{M}\mathbf{T}^T \mathbf{s}}^{n_{aniso}} \frac{\mathbf{T}\mathbf{M}\mathbf{T}^T \mathbf{s}}{\sqrt{\mathbf{s}^T \mathbf{T}\mathbf{M}\mathbf{T}^T \mathbf{s}}}$$

$$\mathbf{M} = \begin{bmatrix} G+H & -H & -G & 0 & 0 & 0 \\ -H & F+H & -F & 0 & 0 & 0 \\ -G & -F & F+G & 0 & 0 & 0 \\ 0 & 0 & 0 & 2N & 0 & 0 \\ 0 & 0 & 0 & 0 & 2L & 0 \\ 0 & 0 & 0 & 0 & 0 & 2M \end{bmatrix} \tag{B.2}$$

where **T** represents a material orientation transformation tensor about the x_1 axis of the form

$$\mathbf{T}=\begin{bmatrix} 1 & 0 & 0 & 0 & 0 & 0 \\ 0 & \cos(\alpha)^2 & \sin(\alpha)^2 & 0 & 0 & \cos(\alpha)\sin(\alpha) \\ 0 & \sin(\alpha)^2 & \cos(\alpha)^2 & 0 & 0 & -\cos(\alpha)\sin(\alpha) \\ 0 & 0 & 0 & \cos(\alpha) & -\sin(\alpha) & 0 \\ 0 & 0 & 0 & \sin(\alpha) & \cos(\alpha) & 0 \\ 0 & -2\cos(\alpha)\sin(\alpha) & 2\cos(\alpha)\sin(\alpha) & 0 & 0 & \cos(\alpha)^2-\sin(\alpha)^2 \end{bmatrix} \tag{B.3}$$

It is assumed that initially the L orientation is aligned with normal x_3 and the isotropic T orientations are found on x_1 and x_2 normals. For the L specimen, $\alpha = 0°$, leading to a creep strain rate in the x_3 normal of

$$\dot{\varepsilon}_{33} = A_L \sigma^{n_L} = A_{aniso}\left(G+F\right)^{\frac{n_{aniso}+1}{2}} \sigma_{33}^{n_{aniso}} \tag{B.4}$$

where it is assumed that F=G and G is chosen arbitrarily. For the T specimen, $\theta = 90°$, thus the creep strain rate in the x_3 normal is

$$\dot{\varepsilon}_{33} = A_T \sigma^{n_T} = A_{aniso}\left(G+H\right)^{\frac{n_{aniso}+1}{2}} \sigma_{33}^{n_{aniso}} \tag{B.5}$$

where rearranging equation (B.4) to solve for A_{aniso} and apply it in equation (B.5) leads to

$$\begin{aligned} H &= \left(2t_1 - 1\right)G \\ t_1 &= \left(\frac{A_T \sigma^{n_T}}{A_L \sigma^{n_L}}\right)^{2/(n_{aniso}+1)} \end{aligned} \tag{B.6}$$

For the 45° specimen, $\theta = 45°$, thus the creep strain rate in the x_3 normal is

$$\dot{\varepsilon}_{33} = A_{45°} \sigma^{n_{45°}} = A_{aniso}\left(0.25G + 0.25H + 0.5M\right)^{\frac{n_{aniso}+1}{2}} \sigma_{33}^{n_{aniso}} \tag{B.7}$$

using equations (B.5) leads to

$$M = G\left(4t_2 - t_1\right)$$

$$t_2 = \left(\frac{A_{45°}\sigma^{n_{45°}}}{A_L\sigma^{n_L}} \right)^{2/(n_{aniso}+1)} \tag{B.8}$$

where it is assumed that L=M. To determine the final constant, N, a symbolic plane stress rotation is applied. Initially the state of stress is set as

$$\boldsymbol{\sigma} = \begin{bmatrix} \sigma_0 & 0 & 0 \\ 0 & -\sigma_0 & 0 \\ 0 & 0 & \sigma_{33} \end{bmatrix}$$

where the Hill equivalent stress resolves to the following

$$\sigma_{Hill} = \sqrt{2G\left(\sigma_{33} + \sigma_0\right)^2 + 4H\sigma_0^{\,2}} \tag{B.9}$$

In the case where the state of stress is rotated by 45° about the x_3 axis, pure shear stress develops in the x_1-x_2 plane of the form

$$\boldsymbol{\sigma}' = \mathbf{Q}\boldsymbol{\sigma}\mathbf{Q}^T = \begin{bmatrix} 0 & -\sigma_0 & 0 \\ -\sigma_0 & 0 & 0 \\ 0 & 0 & \sigma_{33} \end{bmatrix}$$

$$\mathbf{Q} = \begin{bmatrix} \cos(\beta) & \sin(\beta) & 0 \\ -\sin(\beta) & \cos(\beta) & 0 \\ 0 & 0 & 1 \end{bmatrix}$$

where the Hill equivalent stress resolves to the following

$$\sigma_{Hill} = \sqrt{2G\sigma_{33}^{\,2} + 2N\sigma_0^{\,2}} \tag{B.10}$$

then by equating Eqns. (B.9)-(B.10) , the N constant can be determined.

$$N = \left(4t_1 - 1\right)G \tag{B.11}$$

Implementation of Eqns. (B.4), (B.6), (B.8), and (B.11) leads to the constants found in Table B.1.

Table B.1 - Secondary, Hill, and tertiary creep damage constants for DS GTD-111 at 871°C

A_{aniso} $(MPa^{-n_{aniso}}hr^{-1})$			n_{aniso}		
5.7639×10^{-21}			6.5068		
F	*G*	*H*	*L*	*M*	*N*
0.5	0.5	0.3866	1.6413	1.6413	1.2731
M_1 $(MPa^{-\chi}hr^{-1})$	M_2 $(MPa^{-\chi}hr^{-1})$	χ_1	χ_2	ϕ_1	ϕ_2
131.01×10^{-11}	345.84×10^{-11}	2.054	1.9186	9.698	6.8226

To determine the tertiary creep damage constants M_1, M_2, χ_1, χ_2 , ϕ_1, and ϕ_2 an automated optimization routine uSHARP was used [98]. Finite element simulations using the isotropic Kachanov-Rabotnov model Eqns. (4.4)-(4.6) where performed and compared with corresponding creep test data in L and T orientations. The Corona et al. simulated annealing multimodal global optimization algorithm was utilized [99]. The applied constants can be found in Table B.1. Additional results can be found in another paper by the authors [105].

To determine constants for the $\mathbf{M}_b$ and $\mathbf{M}_\lambda$ tensors, the only requirements are the following modifications

$$
\begin{array}{ll}
\mathbf{M}_b & \mathbf{M}_\lambda \\
t_1 = \left(\frac{M_2 \sigma \chi_2}{M_1 \sigma \chi_1} \right)^{2/(\chi_{aniso}+1)} & t_1 = \left(\frac{\phi_2}{\phi_1} \right)^2 \\
t_2 = \left(\frac{M_{45^\circ} \sigma \chi_{45^\circ}}{M_1 \sigma \chi_1} \right)^{2/(n_{aniso}+1)} & t_2 = \left(\frac{\phi_{45^\circ}}{\phi_1} \right)^2
\end{array}
\tag{B.12}
$$

APPENDIX C: ANALYTICAL EXERCISE OF THE NOVEL DAMAGE MODEL

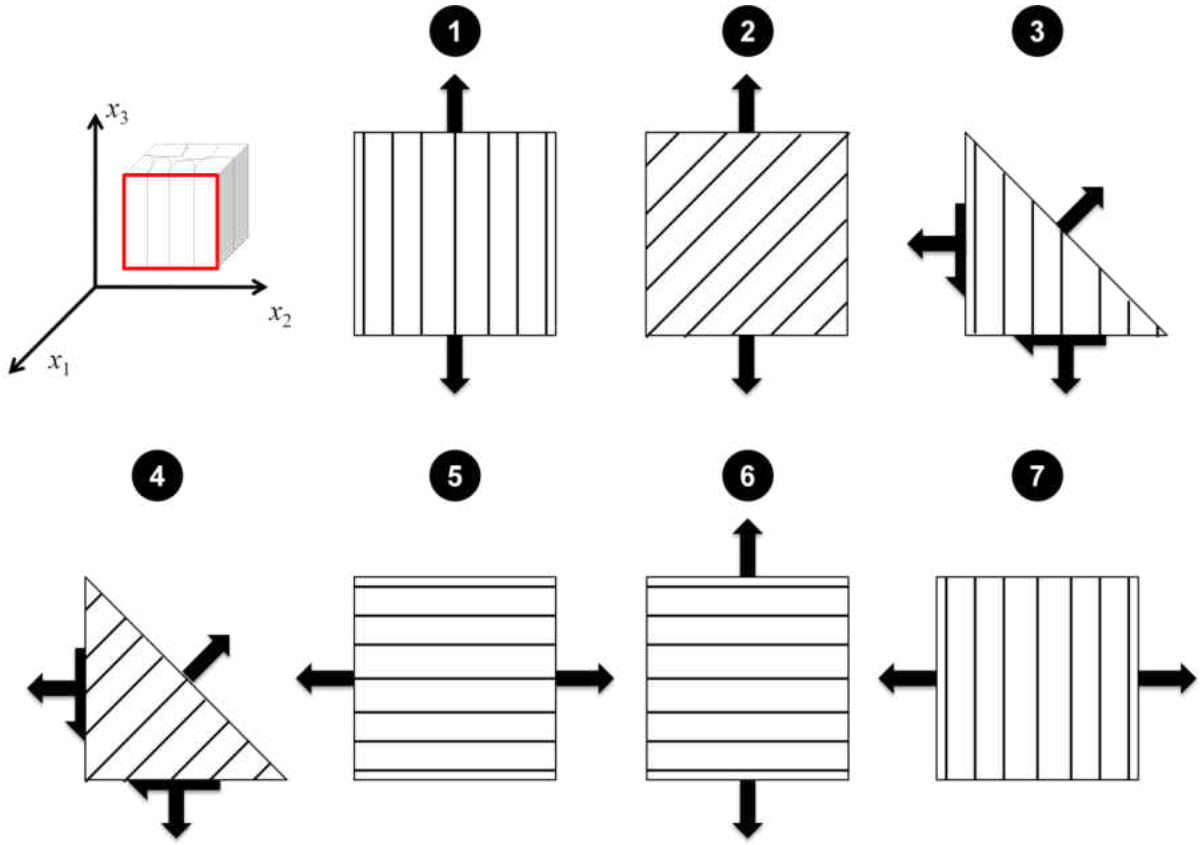

Figure C.1 - Symbolic rotation study configuration schematics

In order to verify the functionality of the developed damage rate equation, an analytic study was performed. Since the first principal stress direction and/or the material orientation may not be aligned with a normal of the representative volume element (RVE) local coordinate system, the damage rate must be determined via rotation. In addition, use of the damage control variable, γ significantly alters the damage rate tensor. Seven configurations of rotation are presented in Figure C.1. The material under consideration is transversely-isotropic thus only 2D schematics are necessary. The conditions of these configurations are listed in Table C.1. Both

material and stress are reoriented about the x_1 axis, where material coincides with angle α and stress transformation with angle β.

Table C.1 – Material and stress orientation cases

Case No.	Configuration	First Principal Stress Direction, $\mathbf{n_1}^T$	Material Orientation Vector, $\mathbf{v}^T$
1	No Rotation (α=0°, β=0°)	$\begin{pmatrix}0 & 0 & 1\end{pmatrix}$	$\begin{pmatrix}0 & 0 & 1\end{pmatrix}$
2	Material 45° Rotation Only (α=45.0°, β=0°)	$\begin{pmatrix}0 & 0 & 1\end{pmatrix}$	$\begin{pmatrix}0 & 1/\sqrt{2} & 1/\sqrt{2}\end{pmatrix}$
3	Stress 45° Rotation Only (α=45.0°, β=45.0°)	$\begin{pmatrix}0 & 1/\sqrt{2} & 1/\sqrt{2}\end{pmatrix}$	$\begin{pmatrix}0 & 0 & 1\end{pmatrix}$
4	Stress and Material 45° Rotation (α=45.0°, β=45.0°)	$\begin{pmatrix}0 & 1/\sqrt{2} & 1/\sqrt{2}\end{pmatrix}$	$\begin{pmatrix}0 & 1/\sqrt{2} & 1/\sqrt{2}\end{pmatrix}$
5	Reference Frame Shift (α=90.0°, β=90.0°)	$\begin{pmatrix}0 & 1 & 0\end{pmatrix}$	$\begin{pmatrix}0 & 1 & 0\end{pmatrix}$
6	Material 90° Rotation Only (α=90.0°, β=0°)	$\begin{pmatrix}0 & 0 & 1\end{pmatrix}$	$\begin{pmatrix}0 & 1 & 0\end{pmatrix}$
7	Stress 90° Rotation Only (α=0°, β=90.0°)	$\begin{pmatrix}0 & 1 & 0\end{pmatrix}$	$\begin{pmatrix}0 & 0 & 1\end{pmatrix}$

In Case 1, neither stress nor material rotations are performed. The rotated damage constant tensors and first principal stress influence tensor are along the diagonal; therefore it is assumed that the shear damage rate elements $\dot{\boldsymbol{\omega}}_{12}, \dot{\boldsymbol{\omega}}_{13}, \dot{\boldsymbol{\omega}}_{23} = 0.0$ and $\omega_{12}, \omega_{13}, \omega_{23} = 0.0$. The following damage rate tensors are produced

$$\dot{\boldsymbol{\omega}}\left(\gamma=0.0\right)=\begin{bmatrix}\dfrac{B_2\sigma_{Hill}^{\chi_2}}{\left(1-\omega_{11}\right)^{|\phi_2|}} & 0 & 0\\ 0 & \dfrac{B_2\sigma_{Hill}^{\chi_2}}{\left(1-\omega_{22}\right)^{|\phi_2|}} & 0\\ 0 & 0 & \dfrac{B_1\sigma_{Hill}^{\chi_1}}{\left(1-\omega_{33}\right)^{|\phi_1|}}\end{bmatrix}$$

$$\dot{\boldsymbol{\omega}}\left(\gamma=1.0\right)=\begin{bmatrix}0 & 0 & 0\\ 0 & 0 & 0\\ 0 & 0 & \dfrac{B_1\sigma_{Hill}^{\chi_1}}{\left(1-\omega_{33}\right)^{|\phi_1|}}\end{bmatrix}$$

where isotropically ($\gamma = 0.0$) damaging materials develop x_1, x_2, and x_3 normal damage rate terms and anisotropically ($\gamma = 1.0$) damaging materials only develop damage in the normal aligned with the first principal stress direction. This result matches the Kachanov-Rabotnov isotropic formulation [5,6].

In Case 2, the material orientation alone is rotated at 45°. When the material is reoriented but the first principal stress direction is still aligned with x_3 of the RVE local coordinate system, effective damage rate terms developed due to the rotated damage constant tensors, **B** and **D**. It is symbolically found a posteriori that shear damage rate elements $\dot{\boldsymbol{\omega}}_{12},\dot{\boldsymbol{\omega}}_{13},\dot{\boldsymbol{\omega}}_{23}=0.0$. Thus it can be assumed a priori that $\omega_{12},\omega_{13},\omega_{23}=0.0$ to produce the following

$$\dot{\boldsymbol{\omega}}\left(\gamma=0.0\right)=\begin{bmatrix}\dfrac{B_2\sigma_{Hill}^{\chi_2}}{\left(1-\omega_{11}\right)^{|\phi_2|}} & 0 & 0\\ 0 & \dfrac{0.5B_1\sigma_{Hill}^{\chi_1}+0.5B_2\sigma_{Hill}^{\chi_2}}{\left(1-\omega_{22}\right)^{|0.5\phi_2+0.5\phi_1|}} & 0\\ 0 & 0 & \dfrac{0.5B_1\sigma_{Hill}^{\chi_1}+0.5B_2\sigma_{Hill}^{\chi_2}}{\left(1-\omega_{33}\right)^{|0.5\phi_2+0.5\phi_1|}}\end{bmatrix}$$

$$\dot{\boldsymbol{\omega}}\left(\gamma=1.0\right)=\begin{bmatrix}0 & 0 & 0\\ 0 & 0 & 0\\ 0 & 0 & \dfrac{0.5B_1\sigma_{Hill}^{\chi_1}+0.5B_2\sigma_{Hill}^{\chi_2}}{\left(1-\omega_{33}\right)^{\left|0.5\phi_2+0.5\phi_1\right|}}\end{bmatrix}$$

where again it is found that isotropically (γ = 0.0) damaging materials develop x_1, x_2, and x_3 normal damage rate terms and anisotropically (γ = 1.0) damaging materials only develop damage in the first principal stress direction.

In Case 3, the state of stress is modified such that the first principal stress direction is rotated at 45°. When the first principal stress direction is not aligned with a normal of the RVE local coordinate system, shear damage terms will appear. Due to the development of shear terms the damage applied tensor, $\boldsymbol{\Omega}$ becomes more complex. It is symbolically found a posteriori that shear damage rate elements $\dot{\boldsymbol{\omega}}_{12},\dot{\boldsymbol{\omega}}_{13}=0.0$. Thus it can be assumed a priori that $\omega_{12},\omega_{13}=0.0$ (It should be noted that for γ = 0.0 it was found also that $\dot{\boldsymbol{\omega}}_{23},\omega_{23}=0.0$) to produce the following

$$\dot{\boldsymbol{\omega}}\left(\gamma=0.0\right)=\begin{bmatrix}\dfrac{B_2\sigma_{Hill}^{\chi_2}}{\left(1-\omega_{11}\right)^{\left|\phi_2\right|}} & 0 & 0\\ 0 & \dfrac{B_2\sigma_{Hill}^{\chi_2}}{\left(1-\omega_{22}\right)^{\left|\phi_2\right|}} & 0\\ 0 & 0 & \dfrac{B_1\sigma_{Hill}^{\chi_1}}{\left(1-\omega_{33}\right)^{\left|\phi_1\right|}}\end{bmatrix}$$

$$\dot{\boldsymbol{\omega}}\left(\gamma=1.0\right)=\begin{bmatrix}0 & 0 & 0\\ & \dfrac{0.5B_2\sigma_{Hill}^{\chi_2}}{\left(1-\omega_{22}{}'\right)^{\left|\phi_2\right|}} & \dfrac{0.25B_1\sigma_{Hill}^{\chi_1}}{\left(1-\omega_{33}{}'\right)^{\left|\phi_1\right|}}+\dfrac{0.25B_2\sigma_{Hill}^{\chi_2}}{\left(1-\omega_{22}{}'\right)^{\left|\phi_2\right|}}\\ SYM & & \dfrac{0.5B_1\sigma_{Hill}^{\chi_1}}{\left(1-\omega_{33}{}'\right)^{\left|\phi_1\right|}}\end{bmatrix}$$

where

$$\left(1-\omega_{22}{}'\right)=\left(\frac{\omega_{33}-1}{\omega_{23}^2+\omega_{22}+\omega_{33}-\omega_{22}\omega_{33}-1}\right)\qquad\left(1-\omega_{33}{}'\right)=\left(\frac{\omega_{22}-1}{\omega_{23}^2+\omega_{22}+\omega_{33}-\omega_{22}\omega_{33}-1}\right)$$

where the stress rotation results in a rotation of the isotropically expected damage rate (seen in Case 1) based on first principal stress direction. Physically this is an accurate representation, similar to the results of a stress transformation of the form $\boldsymbol{\sigma}'=\mathbf{Q}\boldsymbol{\sigma}\mathbf{Q}^T$ but applied on the damage rate tensor.

In Case 4, both the state of stress and material orientation are rotated. Reorientation in both the rotated damage constant tensors and first principal stress influence tensor cause shear terms to develop in addition to transformed damage rate terms. It is symbolically found a posteriori that shear damage rate elements $\dot{\boldsymbol{\omega}}_{12},\dot{\boldsymbol{\omega}}_{13}=0.0$. Thus it can be assumed a priori that $\omega_{12},\omega_{13}=0.0$ (It should be noted that for $\gamma = 0.0$ it was found also that $\dot{\boldsymbol{\omega}}_{23},\omega_{23}=0.0$) to produce the following

$$\dot{\boldsymbol{\omega}}\left(\gamma=0.0\right)=\begin{bmatrix}\dfrac{B_2\sigma_{Hill}^{\chi_2}}{\left(1-\omega_{11}\right)^{|\phi_2|}} & 0 & 0\\ 0 & \dfrac{0.5B_1\sigma_{Hill}^{\chi_1}+0.5B_2\sigma_{Hill}^{\chi_2}}{\left(1-\omega_{22}\right)^{|0.5\phi_2+0.5\phi_1|}} & 0\\ 0 & 0 & \dfrac{0.5B_1\sigma_{Hill}^{\chi_1}+0.5B_2\sigma_{Hill}^{\chi_2}}{\left(1-\omega_{33}\right)^{|0.5\phi_2+0.5\phi_1|}}\end{bmatrix}$$

$$\dot{\boldsymbol{\omega}}\left(\gamma=1.0\right)=\begin{bmatrix}0 & 0 & 0\\ & 0.5M_{22}+0.5M_{23} & 0.25M_{22}+0.25M_{33}+0.5M_{23}\\ SYM & & 0.5M_{33}+0.5M_{23}\end{bmatrix}$$

where

$$M_{22}=\left(\frac{0.5B_1\sigma_{Hill}^{\chi_1}+0.5B_2\sigma_{Hill}^{\chi_2}}{\left(1-\omega_{22}{}'\right)^{|0.5\phi_2+0.5\phi_1|}}\right)\quad M_{33}=\left(\frac{0.5B_1\sigma_{Hill}^{\chi_1}+0.5B_2\sigma_{Hill}^{\chi_2}}{\left(1-\omega_{33}{}'\right)^{|0.5\phi_2+0.5\phi_1|}}\right)\quad M_{23}=\left(\frac{0.5B_1\sigma_{Hill}^{\chi_1}-0.5B_2\sigma_{Hill}^{\chi_2}}{\left(1-\omega_{23}{}'\right)^{|0.5\phi_2-0.5\phi_1|}}\right)$$

$$\left(1-\omega_{22}{}'\right)=\left(\frac{\omega_{33}-1}{\omega_{23}^2+\omega_{22}+\omega_{33}-\omega_{22}\omega_{33}-1}\right)\qquad\left(1-\omega_{33}{}'\right)=\left(\frac{\omega_{22}-1}{\omega_{23}^2+\omega_{22}+\omega_{33}-\omega_{22}\omega_{33}-1}\right)$$

$$\left(1-\omega_{23}{}'\right)=\left(\frac{-\omega_{23}}{\omega_{23}^2+\omega_{22}+\omega_{33}-\omega_{22}\omega_{33}-1}\right)$$

where the rotation of the material orientation leads to effective damage rate terms. For isotropically damaging materials the model reacts similar to Case 2, while for anisotropically damaging materials the coupled stress rotation leads to a highly complex calculation. Conveniently, Tensor mathematics simplifies implementation. Due to the complexity of this solution, it is difficult to derive any relevant physical interpretation. However careful examination shows a rotation of the effective damage terms found in Case 2.

In Case 5, a 90° rotation of both the state of stress and material orientation occurs. It is resolved as follows

$$\dot{\boldsymbol{\omega}}\left(\gamma=0.0\right)=\begin{bmatrix}\dfrac{B_2\sigma_{Hill}^{\chi_2}}{\left(1-\omega_{11}\right)^{|\phi_2|}} & 0 & 0\\ 0 & \dfrac{B_1\sigma_{Hill}^{\chi_1}}{\left(1-\omega_{22}\right)^{|\phi_1|}} & 0\\ 0 & 0 & \dfrac{B_2\sigma_{Hill}^{\chi_2}}{\left(1-\omega_{33}\right)^{|\phi_2|}}\end{bmatrix}$$

$$\dot{\boldsymbol{\omega}}\left(\gamma=1.0\right)=\begin{bmatrix}0 & 0 & 0\\ 0 & \dfrac{B_1\sigma_{Hill}^{\chi_1}}{\left(1-\omega_{22}\right)^{|\phi_1|}} & 0\\ 0 & 0 & 0\end{bmatrix}$$

showing a pure plane shift of the system can accurately be performed.

In Case 6, the material orientation alone is rotated at 90°. When the material is reoriented (90°) while the first principal stress direction is still aligned (0°), it is found that the T orientation is parallel to the first principal stress. It is symbolically found a posteriori that shear damage rate elements $\dot{\boldsymbol{\omega}}_{12}, \dot{\boldsymbol{\omega}}_{13}, \dot{\boldsymbol{\omega}}_{23} = 0.0$. Thus it can be assumed a priori that $\omega_{12}, \omega_{13}, \omega_{23} = 0.0$ to produce the following

$$\dot{\boldsymbol{\omega}}\left(\gamma = 0.0\right) = \begin{bmatrix} \dfrac{B_2 \sigma_{Hill}^{\chi_2}}{\left(1-\omega_{11}\right)^{|\phi_2|}} & 0 & 0 \\ 0 & \dfrac{B_1 \sigma_{Hill}^{\chi_1}}{\left(1-\omega_{22}\right)^{|\phi_1|}} & 0 \\ 0 & 0 & \dfrac{B_2 \sigma_{Hill}^{\chi_2}}{\left(1-\omega_{33}\right)^{|\phi_2|}} \end{bmatrix}$$

$$\dot{\boldsymbol{\omega}}\left(\gamma = 1.0\right) = \begin{bmatrix} 0 & 0 & 0 \\ 0 & 0 & 0 \\ 0 & 0 & \dfrac{B_2 \sigma_{Hill}^{\chi_2}}{\left(1-\omega_{33}\right)^{|\phi_2|}} \end{bmatrix}$$

where for isotropically damaging materials the Case 5 tensor is found again. However, for anisotropic damaging materials only the element coinciding with the first principal stress direction arises.

In Case 7, the state of stress is modified such that the first principal stress direction is rotated at 90° while material orientation is still aligned (0°). Using the same assumptions as Case 6 the following is produced

$$\dot{\boldsymbol{\omega}}\left(\gamma = 0.0\right) = \begin{bmatrix} \dfrac{B_2 \sigma_{Hill}^{\chi_2}}{\left(1-\omega_{11}\right)^{|\phi_2|}} & 0 & 0 \\ 0 & \dfrac{B_2 \sigma_{Hill}^{\chi_2}}{\left(1-\omega_{22}\right)^{|\phi_2|}} & 0 \\ 0 & 0 & \dfrac{B_1 \sigma_{Hill}^{\chi_1}}{\left(1-\omega_{33}\right)^{|\phi_1|}} \end{bmatrix}$$

$$\dot{\boldsymbol{\omega}}\left(\gamma = 1.0\right) = \begin{bmatrix} 0 & 0 & 0 \\ 0 & \dfrac{B_2 \sigma_{Hill}^{\chi_2}}{\left(1-\omega_{22}\right)^{|\phi_2|}} & 0 \\ 0 & 0 & 0 \end{bmatrix}$$

where for isotropically damaging materials the Case 1 tensor is found again. However, for anisotropic damaging materials only the element coinciding with the first principal stress direction arises.

Examining the results of Cases 1-7, it is shown that the model performs robustly under various rotation configurations. Damage rates are not only determined by the induce anisotropy controlled by the first principal stress direction via,γ , but also the material orientation both relative to a normal of the RVE local coordinate system.

LIST OF REFERENCES

[1] Schilke, P. W., Foster, A.D., Pepe, J. J., and Beltran, A. M., 1992, "Advanced Materials Propel Progress in LAND-BASED GAS TURBINES," *Advanced Materials and Processes*, **141**(4), pp. 22-30.

[2] Viswanathan, R., and Scheirer, S. T., 2001, "Materials Technology for Advanced Land Based Gas Turbines," *Creep: proceedings of the international conference on creep and fatigue at elevated temperatures*, Tsukuba, Japan, No.01-201 (20010603), pp. 7-21.

[3] Siemens Energy, 2006, "Gas Turbine," Siemens press picture. <http://www.powergeneration.siemens.com/press/press-pictures/gas-turbines/gas-turbine-4.htm>

[4] Hayhurst, D. R., 1972, "Creep Rupture Under Multi-Axial States Of Stress," *Journal of the Mechanics and Physics of Solids*, **20**(6), pp. 381-382.

[5] Kachanov, L. M., 1967, *The Theory of Creep*, National Lending Library for Science and Technology, Boston Spa, England, Chaps. IX, X.

[6] Rabotnov, Y. N., 1969, *Creep Problems in Structural Members*, North Holland, Amsterdam.

[7] Misseijer, R. C., Thabit, T. I., and Mattheij, J. H. G., 1996, "Operational evaluation of patch repaired combustion gas turbine transition pieces," *Journal of Quality in Maintenance Engineering*, **2**(4), pp. 59-70.

[8] Daleo, J.A. and Wilson, J.R., 1998, "GTD111 alloy material study," *Journal of Engineering for Gas Turbines and Power, Transactions of the ASME*, **120**(2), pp. 375-382.

[9] Elliott, A. J. and Pollock, T. M., "Thermal Analysis of the Bridgman and Liquid-Metal Cooled Directional Solidification Investment Casting Processes," *Metallurgical and Materials Transactions A*, **38**(4), pp 871-882.

[10] Siemens Energy, 2009, " New blade hall for Berlin – Turbine layers," Siemens press picture. <http://w1.siemens.com/press/en/presspicture/pictures-photonews/2009/pn200909/pn200909-02.htm>

[11] Kermanpur, A., Mehrara, M., Varahram, N., and Davami, P., 2008, "Improvement of grain structure and mechanical properties of a land based gas turbine blade directionally solidified with liquid metal cooling process.," *Materials Science & Technology*, **24**(1), pp. 100-106.

[12] Xie, Y., Wang, M., Zhang, G., and Chang, M., 2006, "Analysis of Superalloy Turbine Blade Tip Cracking During Service," *Engineering Failure Analysis*, **13**(8), pp. 1429-1436.

[13] Pridemore, W. D., 2008, "Stress-Rupture Characterization in Nickel-Based Superalloy Gas Turbine Engine Components," *Journal of Failure Analysis and Prevention*, **8**(3), pp. 281-288.

[14] National Research Council (U.S.) Committee on Materials for Large Land-Based Gas Turbines, 1986, "Materials for large land-based gas turbines," National Academy Press.

[15] Betten, J., 2002, *Creep Mechanics*, Springer.

[16] Kassner, M. E. , and Pérez-Prado M., 2004, *Fundamentals of creep in metals and alloys*, Elsevier, pp.47-49.

[17] Heilmaier, M., and Reppich, B., 1997, "On the Microstructural Origin of Primary Creep in Nickel-Base Superalloys," *Materials Science and Engineering*, A234-236, pp 501-504.

[18] Penny, R. K., and Marriott, D. L., 1995, *Design for Creep*, Springer, pp.11.

[19] Andrade, E. N., 1910, "The Viscous Flow in Metals and Allied Phenomena," *Proceedings of the Royal Society*, **A 84**, pp 1-12.

[20] Andrade, E. N., 1914, "Flow of Metals under Large Constant Stress," *Proceedings of the Royal Society*, **A 90**, pp 329-342.

[21] Nabarro, F. R. N., 1997, "Thermal Activation and Andrade Creep," *Philosophical Magazine Letters*, **74**(4), pp 227-233.

[22] Pantelakis, S., 1983, *Kriechverhalten metallischer Werkstoffe bei zeitveranderlicher Spannug*, PhD Thesis, RWTH-Aachen.

[23] Odquist, F., and Hult, J., 1962, *Kriechfestigkeit metallischer Werkstoffe*, Springer Berlin.

[24] Stewart C. M., and Gordon A. P., (2009), "Modeling the Temperature Dependence of Tertiary Creep Damage of a Ni-base Alloy," *Journal of Pressure Vessel Technology*, **131**(5), pp.1-11.

[25] Norton, F. H., 1929, *The creep of steel at high temperatures*, McGraw-Hill, London.

[26] Hill, R., 1950, *The Mathematical Theory of Plasticity*, Oxford University Press, New York.

[27] Hyde, T. D., Jones, I.A., Peravali, S., Sun, W., Wang, J.G., and Leen S. B., 2005, "Anisotropic Creep Behavior of Bridgman Notch Specimens," *Proceedings of the Institution of Mechanical Engineers, Part L: Journal of Materials: Design and Applications*, **219**(3), pp. 163-175.

[28] Webster, G. A., and Ainsworth, R. A., 1994, *High temperature component life assessment*, Chapman & Hall, London.

[29] Monkman, F. and Grant, N., (1956), Proc. ASTM, **56**, p. 595.

[30] Ibanez, A. R., Srinivasan, V. S., and Saxena, A., 2006, "Creep Deformation and Rupture Behaviour of Directionally-solidified GTD 111 Superalloy," *Fatigue & Fracture of Engineering Materials & Structures*, **29**(12), pp. 1010 – 1020.

[31] Guo, J., Yuan, C., Yang, H., Lupinc, V and Maldini, M., (2001), "Creep-Rupture Behavior of a Directionally Solidified Nickel-Base Superalloy", Metallurgical and Materials Transactions A, **32**, pp. 1103-1110.

[32] Dorn, J.E., 1955, "Some Fundamental experiements on high temperature creep", *Journal of the Mechanics and Physics of Solids*, **3**, pp. 85-116.

[33] Garofalo, F., 1965, *Fundamentals of Creep and Creep-Rupture in Metals*, Macmillan, New York.

[34] Skrzypek, J. and Ganczarski, A., 1999, *Modeling of material damage and failure of structures*, Springer, pp. 69-78.

[35] Lemaitre, J. (1986). Local Approach of Fracture. *Engineering Fracture Mechanics Vol. 25 No. 5/6* , 523-537.

[36] Govindaraju, M. R. , Kaminski, D. A., Devine, M. K. , Biner, S. B. and Jiles, D. C., 1997, "Nondestructive Evaluation of Creep Damage in Power-Plant Steam Generators and Piping by Magnetic Measurements," *NDT & E International*, **30**(1), pp 11-17.

[37] Hatanaka, K.,Yahya, A. N., Nonaka, I., and Umaki, H., 1999, "Initiation of High Tempearture Creep Voids in Notched Components," *JSME Internaional Journal*, 42(2), pp. 280 -287.

[38] Le May, I., and Furtado, H. C., 1999, "Creep Damage Assessment and Remaining Life Evaluation," *International Journal of Fracture*, **97**(1), pp 125-135.

[39] Leckie, F. A., and Hayhurst, D. R., 1977, "Constitutive equations for creep rupture," *Acta Metall.*, **25**, pp. 1059 – 1070.

[40] Leckie, F. A., and Ponter, A., 1974, "On the State Variable Description of Creeping Materials," *Ing.-Archiv.*, **43**, pp. 158-167.

[41] Hayhurst, D., Trampczynksi, W., and Leckie, F. A., 1980, "Creep Rupture and Nonproportional Loading," *Acta Metall.*, **28**, pp 1171-1183.

[42] Hyde, T.D., Sun, W., and Williams, J.A, 1999, "Creep Behaviour of Parent, Weld and HAZ Materials of New, Service-Aged and Repaired 1/2Cr1/2Mo1/4V: 2 1/4Cr1Mo Pipe Welds at 640°C," *Material at High Temperatures*, 16(3), pp 117-129.

[43] Maclachlan, D. W. and Knowles, D. M., 2000, "Creep-Behavior Modeling of the Single-Crystal Superalloy CMSX-4," *Metallurgical and Materials Transactions A*, **31**(5), pp. 1401-1411.

[44] Batsoulas, N. D., 2009, "Creep Damage Assessment and Lifetime Predictions for Metallic Materials under Variable Loading Conditions in Elevated Temperature Applications," *Steel Research International*, **80**(2), pp 152-159.

[45] Altenbach H., Huang C., and Naumenko K., 2002, "Creep damage Predictions in Thin-Walled Structures by use of Isotropic and Anisotropic Damage Models*," Journal of strain analysis for engineering design*, **37**(3), pp. 265-275.

[46] Murakami, S. and Sanomura, Y., 1985, "Creep and Creep Damage of Copper Under Multiaxial States of Stress," *In Plasticity Today*, edited by A. Sawczuk and G. Bianci, pp. 535–551.

[47] Murakami, S. and Ohno, N., 1981, "A Continuum Theory of Creep and Creep Damage.," *In Creep in Structures*, A. R. S. Ponter and D. R. Hayhurst, eds., pp. 422–443.

[48] Trampczynski, W. A., Hayhurst, D. R., and Leckie, F. A., 1981, **"**Creep Rupture of Copper and Aluminum Under Non-Proportional Loading**,"** *Journal of the Mechanics and Physics of Solids*, **29**(5-6), pp. 353-374.

[49] Betten, J., El-Magd, E., Meydanli, S. and Palmen, P., 1995, "Bestimmung der Materialkennwerte einer dreidimensionalen Theorie zur Beschreibung des tertia¨ren Kriechverhaltens austenitischer Sta¨hle auf der Basis der Experimente," *Arch. Appl. Mechanics*, **65**(2), pp. 110–120.

[50] Murakami, S., 1990, "A Continuum Mechanics Theory of Anisotropic Damage," *Yielding, Damage and Failure of Anisotropic Solids,* J. P. Boehler, eds., Mechanical Engineering Publications, London, pp. 465–482.

[51] Stewart,C. M, Gordon, A. P., and Nicholson, D. W., 2009, "Numerical Simulation of Temperature-Dependent, Anisotropic Tertiary Creep Damage," *47th AIAA Aerospace Sciences Meeting Including The New Horizons Forum and Aerospace Exposition*, Orlando, Fl, January 5-8 2009.

[52] Radayev, Y.N., 1996, "Thermodynamical Model of Anisotropic Damage Growth. Part I. Canonical Dynamic State Variables of Continuum Damage Mechanics and Thermodynamical Functions of Three-Dimensional Anisotropic Damage State," *Journal of Non-Equilibrium Thermodynamics*, **21**(2), pp. 129-152.

[53] Radayev, Y.N., 1996, "Thermodynamical Model of Anisotropic Damage Growth. Part II. Canonical Damage Growth Rate Equations and Theory Of Damage Invariants," *Journal of Non-Equilibrium Thermodynamics*, **21**(3), pp. 197-222.

[54] Rabotnov, Y., 1968, “Creep Rupture,” *Applied Mechanics Conference*, Stanford University, Palo Alto, pp. 342-349.

[55] Murakami, S., 1987, “Progress of Continuum Damage Mechanics,” *JSME International Journal*, **30**(263), pp. 701-710.

[56] Murakami, S., 1988, “Mechanical Modeling of Material Damage,” *Trans. ASME Journal of Applied Mechanics*, **55**, pp. 280-286.

[57] Peravali, S., Hyde, T. H., Cliffe, K. A., and Leen, S. B., 2009, “An Anisotropic Creep Damage Model for Anisotropic Weld Metal,” *Journal of Pressure Vessel Technology*, **131**(2), pp. 1-8

[58] Cordebois, J. P., and F. Sidoroff, F., 1982, “Damage Induced Elastic Anisotropy,” In: J.P. Boehler, Editor, *Mechanical Behavior of Anisotropic Solids*, Matinus Nijhoff, The Hague, pp. 761–774.

[59] Cordebois, J. P., and F. Sidoroff, F., 1982, “Endommagement Anistrope en Elasticite et Plasticite,” *J. Mec. Theor. Appl.*, Numero Special, pp. 45-60.

[60] Murakami, S., and Imaizumi, T. J., 1982, “Mechanical Description of Creep Damage State and its Experimental Verification,” *Mec. Theor. Appl.*, **1**(5), pp. 743-761.

[61] Murakami, S., Sanomura, Y., and Saitoh, K., 1986, “Formulation of Cross-Hardening in Creep and its Effect on the Creep Damage Process of Copper,” *Journal of Engineering Materials and Technology*, **108**(2), pp. 167-173.

[62] Murakami, S., Sanomura, Y., 1986, “Analysis of the Coupled Effect of Plastic Damage and Creep Damage in Nimonic 80A at Finite Deformation,” *Engineering Fracture Mechanics*, **25**(5/6), pp. 693-704.

[63] Lemaitre, J., and Chaboche, J. L., 1978, “Aspect Phénoménologique de la Rupture par Endommagement,” *J. de Mecanique Appliquée*, **2**(3), pp. 317-365.

[64] Chaboche, J. L., 1982, "Le Concept de Contrainte Effective Appliquée À L'élasticité Et À La Viscoplasticité en Présence d'un Endommagement Anisotrope," Mechanical behavior of anisotropic solids, *Proc, Euromech 115*, Villars de Lans, Editions du CNRS, No. 295, pp. 737–760.

[65] Chow, C., and Wang, J., 1987, “An Anisotropic Theory of Elasticity for Continuum Damage Mechanics,” *International Journal of Fracture*, **33**, pp. 3-16.

[66] Ohno, N., Mizuno, T., Kawaji, H., And Okada, I, 1992, “Multiaxial Creep of a Nickel-Base Directionally Solidified Alloy: Anisotropy and Simulation,” *Acta Metall, Mater.* **40**(3), pp. 559-567.

[67] Shesterikov, S. A., Lokochtchenko, A. M., and Mjakotin, E. A., 1998, "Creep Rupture of Anisotropic Pipes," *Journal of Pressure Vessel Technology*, **120**(3), pp. 223-225.

[68] Kawai, M., 1997, "Coupled Inelasticity and Damage Model for Metal Matrix Composites," *International Journal of Damage Mechanics*, **6**(4), pp. 453-478.

[69] Hyde, T. H., Jones, I. A., Peravali, S., Sun, W., Wang, J. G., and Leen, S. B., 2005, "Anisotropic Creep Behaviour of Bridgman Notch Specimens," *Proceedings of the Institution of Mechanical Engineers. Part L*, *Journal of Materials, Design and Applications*, **219**(3), 163-175.

[70] Yaguchi, M., Yamamoto, M., Ogata, T., 2007, "A Unifed Anisotropic Constitutive Model for Ni Base Directionally Solidified Superalloy," *Eighth Intentional Conference on Creep and Fatigue at Elevated Temperatures (CREEP8),* San Antonio, Texas.

[71] Betten, J., 2001, Kontinuumsmechanik, 2. Aufl., Springer Verlag, Berlin, Heidelberg, New York.

[72] Harris, K., Erikson, G. L., and Schwer, R. E., "Directionally Solidified and Single-Crystal Superalloys," ASM Handbook Tenth Edition: Properties and Selection: Irons, Steels, and High-Performance Alloys, **1**, pp. 995-1006.

[73] Li, L., 2006, "Repair of directionally solidified superalloy GTD-111 by laser-engineered net shaping," *Journal of Materials Science*, **41**(23), pp. 7886-7893.

[74] Schilke, P.W., 2004, "Advanced Gas Turbine Materials and Coatings," GE ENERGY, Schenectady, NY.

[75] Viswanathan, R., and Scheirer, S. T., 1998, "Materials Advances in Land-Based Gas Turbines," *POWER-GEN 1998 Conference*, Orlando, FL.

[76] Sajjadi, S. A., and Nategh, S., 2001, "A High Temperature Deformation Mechanism Map for the High Performance Ni-Base Superalloy GTD-111," *Materials Science and Engineering A*, **307**(1-2), pp. 158-164.

[77] Hale, J. M., 1994, "Procedure Development for the Repair of GTD-111 Gas Turbine Bucket Material," *Eighth Congress &Exposition on Gas Turbines in Cogeneration and Utility*, Portland, OR.

[78] Smallman, R. E. and Bishop, R. J., 1999, *Modern physical metallurgy and materials engineering: science, process, applications*, Butterworth-Heinemann, pg 46-47.

[79] Doi, M., Miki, D., Moritani, T., and Kozakai, T., 2004, "Gamma/Gamma-Prime Microstructure Formed by Phase Separation of Gamma-Prime Precipitates in a Ni-Al-Ti Alloy," *Superalloys 2004*, TMS, pp. 109-114.

[80] Gordon, A. P., 2006, "Crack Initiation Modeling of a Directionally-Solidified Nickel-Base Superalloy," Dissertation, *Georgia Institute of Technology*, pp. 6-59.

[81] Gale, W. F., Smithells, C. J., and Totemeier, T. C., 2004, *Smithells Metals Reference Book 8th Edition*, Butterworth-Heinemann, pp. 7-12, Chap. 38.

[82] Yamabe-Mitari, Y., Ro, Y., Maruko, T. and Harada, H., 1999, "Microstructure Dependence of Strength of Ir-Base Refractory Superalloys," *Intermetallics*, **7**(1), pp. 49-58.

[83] ASTM E-139, "Standard Test Methods for Conducting Creep, Creep-Rupture, and Stress-Rupture Tests of Metallic Materials," No. 03.01, West Conshohocken, PA.

[84] Stewart, C. M., Gordon, A. P., Ma, Y. M., and Neu, R. W., 2009, "Anisotropic Creep Damage Modeling of a Directionally-Solidified Ni-base Superalloy," *International Journal of Pressure Vessels and Piping (under development).*

[85] Zuo, M., Chiovelli, S., and Nonaka, Y., 2000, "Fitting Creep-Rupture Life Distribution Using Accelerated Life Testing Data," *Journal of Pressure Vessel Technology*, **122**(4), pp. 482-487.

[86] Hyde, T. H., Sun, W., Tang A., 1998, "Determination of the material constants in creep continuum damage constitutive equations" *Strain*, **34**(3), pp. 83-90.

[87] Hoff, N.J., 1953, "Necking and rupture of rods subjected to constant tensile loads," *Journal of Applied Mechanics*, **20**(1), pp. 105-108.

[88] Hyde, T. H., Xia, L., and Becker, A. A., 1996, "Prediction of Creep Failure in Aeroengine Materials under Multiaxial Stress States," *International Journal of Mechanical Sciences*, **38**(4), pp. 385-403.

[89] Jeong, C. Y., Nam, S. W., and Ginsztler, J. 1999, "Stress dependence on stress relaxation creep rate during tensile holding under creep-fatigue interaction in 1Cr-Mo-V steel," *Journal of Materials Science*, v **34**(11), pp. 2513-2517.

[90] Ibanez, A. R., 2003, "Modeling Creep Behavior in a Directionally Solidified Nickel Base Superalloy," Dissertation, *Georgia Institute of Technology*.

[91] ANSYS® Academic Teaching Introductory, Release 11.0, ANSYS, Inc.

[92] McGaw, M. A., 1993, "Cumulative Damage Concepts in Thermomechanical Fatigue," *Thermomechanical Fatigue Behavior of Materials*, ASTM STP 1186, H. Sehitoglu, Ed., American Society of Testing and Materials, Philadelphia, PA , pp. 144-156.

[93] Hyde, T. H., Becker, A. A., and Sun, W., 2001, "Creep Damage Analysis of Short Cracks Using Narrow Notch Specimen made from a Ni-base Superalloy at 700°C," *10th International Conference on Fracture*, Honolulu, HI.

[94] Altenbach, J., Altenbach, H., and Naumenko, K., 2004, "Edge Effects in Moderately Think Plates under Creep-Damage Conditions," *Technische Mechanik*, **24**(3-4), pp. 254-263.

[95] Hayhurst, D. R., 1983, "On the Role of Continuum Damage on Structural Mechanics," *Engineering Approaches to High Temperature Design*, B. Wilshire and D. R. Owen, eds., Pineridge Press, Swansea, pp. 85-176.

[96] Johnson, A. E., Henderson, J., and Khan, B., 1962, *Complex-Stress Creep, Relaxation and Fracture of Metallic Alloys*, HMSO, England. Chap. 6.

[97] Kouhia, R., Marjamaki, P.,and Kivilahti, J., 2005, "On the implicit integration of rate-dependent inelastic constitutive models," *International Journal for Numerical Methods in Engineering*, **62**(13), pp. 1832-1856.

[98] Hogan, E. A., 2009, "An efficient method for the optimization of Viscoplastic constitutive model constants," Honors in the Major Undergraduate Thesis, University of Central Florida, Orlando, FL.

[99] Corana, A., Marchesi, M., Martini, C., and Ridella, S., 1987, "Minimizing Multimodal Functions of Continuous Variables with the 'Simulated Annealing" Algorithm," *ACM Transactions on Mathematical Software*, **13**(3), pp. 262-280.

[100] Goffe, W. L., Gary, D. F., and Rogers, J., 1993, "Global Optimization of Statistical Functions with Simulated Annealing," *Journal of Econometrics*, **60**(1/2), pp. 65-100.

[101] Schur, I., Joseph, A., Melnikov, A., and Rentschler, R., 2003, *Studies in memory of Issai Schur*, Springer, Chap. xci.

[102] Bernstein, D. S., 2005, *Matrix mathematics*, Princeton University Press, pp 252-253, Chap. 7.3.

[103] Lin, G, 1999, "ANSYS USER Material Subroutine USERMAT," ANSYS, Inc., Canonsburg, PA.

[104] Gardner, B., Saxena, A., and Qu, J., 2001, "Creep Crack Growth Parameters for Directionally-solidified Superalloys", *International Conference on Fracture (ICF10)*, Elsevier Science, Honolulu, HI.

[105] Stewart, C. M., and Gordon, A. P., 2009, "Modeling the Temperature-Dependence of Tertiary Creep Damage of a Directionally-solidified Ni-Base Superalloy," *Proceedings of the 2009 ASME International Mechanical Engineering Congress & Exposition*, Lake Buena Vista, Fl.

[106] Gordon, A. P., Shenoy, M. M., and McDowell, D. L., 2005, "Simulation of Creep Crack Growth of a Directionally-Solidified Ni-Base Superalloy," *Proceedings of the 11th International Conference on Fracture*, Turlin, Italy.

[107] Peterson, L. G., Hrencecin, D., Ritter, A., and Lewis, N., "Hip Diffusion Bonding of P/M Alloys for Composite Land-Based Gas Turbine Buckets," *Progress in Powder Metallurgy*, **41**, pp. 561-578.

[108] Woodford, D. A. and Frawley, J. J., 1974, "Effect of Grain Boundary Orientation on Creep and Rupture of In-738 and Nichrome," *Metallurgical Transactions*, **5**(9), pp. 2005-2013.

[109] Sessions, M. L. and McMahon, C. J. Jr, 1975, "Influence of Stress Components on Intergranular Oxidation and Cracking in a Nickel-Base Superalloy," *Nuclear Technology*, pp. 477-489.

[110] ANSYS Inc., 2007, "Theory Reference for ANSYS and ANSYS Workbench," Canonsburg, PA, pp. 103-105, Chap. 4.3.

[111] G.E., 1992, "Power Generation Engineering: DS GTD-111 Preliminary UTS Data"

[112] Smith, I., Landis, E., and Gong, M., 2003, *Fracture and fatigue in wood*, John Wiley & Sons,West Sussex, UK.

[113] Tang Chak-yin, Fan Jianping, Tsui Chi-pong, Lee Tai-chiu, Chan Luen-chow, and Rao Bin, 2007, "Quantification of Shear Damage Evolution in Aluminium Alloy 2024T3" Acta Mechanica Solida Sinica, **20**(1), pp. 57-64.

[114] Mayr, C., Eggeler, G., Webster, G. A., and Peter, G., 1995, "Double Shear Creep Testing of Superalloy Single Crystals at Temperatures above 1000°C" Materials Science and Enginering A, **199**(2), pp. 121-130.